A scalable multimodal approach for quantifying the nerve fiber architecture of the human brain

---

Kai Benning

Dissertation vorgelegt:

21. Mai 2024

Tag der mündlichen Prüfung:

13. November 2024

Gutachter:

1. Prof. Dr. Markus Axer
2. Prof. Dr. Dirk Lützenkirchen-Hecht
3. Prof. Dr. Gunnar Schröder

Fakultät für Mathematik und Naturwissenschaften
Bergische Universität Wuppertal

Strukturelle und funktionelle Organisation des Gehirns (INM-1)
Forschungszentrum Jülich GmbH

Cécile und Oskar Vogt Institut für Hirnforschung
Universitätsklinikum Düsseldorf

A scalable multimodal approach for quantifying the nerve fiber architecture of the human brain

Dissertation zur Erlangung des Doktorgrades

Dr. rer. nat.

an der Fakultät
für Mathematik und Naturwissenschaften
der Bergischen Universität Wuppertal

vorgelegt von

Kai Benning

in

Wuppertal

im Mai 2024.

Abstract

In 3D Polarized Light Imaging (3D-PLI) the birefringence of nerve fibers is used to measure and reconstruct how nerve fibers are oriented in histological sections. With the introduction of oblique views in the polarimeter, every detected fiber or fiber bundle in a voxel of the mounted histological section can be unambiguously attributed to an in-plane angle φ and an out-of-plane angle α. Furthermore, each voxel has a specific Transmittance quantifying the transmitted light and a Retardation $\sin\delta$ which quantifies the birefringence strength in this voxel.

The development of new microscopes which pushed the resolution for 3D-PLI with oblique views from 60 µm down to 1.85 µm greatly increased the amount of data that has to be processed. In this work, the size of the data, unused HPC resources and the needed reproducibility of the data processing led to the development of an automatic workflow of 3D-PLI processing on HPC. Additionally, an integrated testing scheme is presented for the orientational analysis, as well as porting the GPU implementation of the least-squares-based orientational analysis to Multi-GPU and further, the integration of optional denoising into the workflow.

Because point estimates of orientation vectors $\vec{f}(\varphi, \alpha)$ lack quantification of their credibility, the present Bayesian implementation (still using CPU) of the objective function is accelerated in two different ways. First, by implementing the objective function in OpenCL and using the Multi-threaded Optimization Toolbox (MOT) to perform the Monte-Carlo Markow-Chain (MCMC) Sampling data-parallel on the GPU to obtain a speed-up factor ≈ 7 (from 310 min to 44 min for a section, exemplarily) in exchange for underestimation of the variances and noisier distributions. Secondly, by formulating the credibility interval (CI) estimation as a regression problem using Generalized Additive Models (GAMs). The MCMC sampling is only performed on a representative subset ($10^2 - 10^3$ datapoints vs. $> 10^6$ datapoints) of the dataset and the remaining CIs are predicted, lowering the sampling time to a few hundred seconds sequential and to a few seconds parallelized using up to 128 cores on a single HPC node.

Finally, a 2D-section to 3D-volume registration workflow of 3D-PLI parameter maps using 3D-PLI Blockface images is introduced to correlate 3D-PLI volumes with Diffusion Weighted Imaging (DWI) volumes. It consists of quickly selecting 3D-PLI Region of Interest (ROIs), which can be interactively registered and correlated with DWI volumes using the well-established software suite `3D-Slicer`, leveraging its rich extension ecosystem. Thereby, first results of the correlation of Retardation, and rel. Thickness vs. Myelin Water Fraction (MWF) of DWI are shown. The results show strong linear agreement and furthermore, correlations with Transmittance show that low-myelination areas (as indicated by MWF) can be identified with a combined measure of Retardation and (local maxima of) Transmittance.

Zusammenfassung

Beim 3D Polarized Light Imaging (3D-PLI) wird die Doppelbrechung von Nervenfasern genutzt, um zu messen und zu rekonstruieren, wie Nervenfasern in histologischen Schnitten ausgerichtet sind. Durch die Einführung von Schrägansichten im Polarimeter kann jeder detektierte Faser oder jedem Faserbündel in einem Voxel eines histologischen Schnitts eindeutig ein Winkel in der Ebene (φ) und ein Winkel aus der Ebene heraus (α) zugeordnet werden. Darüber hinaus bekommt jedes Voxel eine spezifische Transmittanz, die angibt wie viel Licht durchgelassen wurde, und eine Retardierung ($\sin\delta$), die die Stärke der Doppelbrechung angibt.

Die Entwicklung neuer Mikroskope, mit denen die Auflösung für 3D-PLI mit schrägem Lichteinfall von 60 µm auf 1,85 µm gesenkt werden konnte, hat die Menge der zu verarbeitenden Daten stark erhöht. In dieser Arbeit führten die Größe der Daten, ungenutzte HPC-Ressourcen und die erforderliche Reproduzierbarkeit der Datenverarbeitung zur Entwicklung eines automatisierten Workflows für die Verarbeitung der Daten auf HPC. Zusätzlich wird ein Testschema für die auf der Methode der kleinsten Quadrate basierenden Orientierungsanalyse vorgestellt sowie die Portierung der GPU-Implementierung der Orientierungsanalyse auf Multi-GPU und die Integration von optionaler Artefaktbereinigung in den Workflow.

Da Punktschätzungen der Orientierungen $\vec{f}(\varphi, \alpha)$ in Bezug auf ihre Genauigkeit nicht quantifiziert werden können, wird die derzeitige Bayes'sche Implementierung der Zielfunktion (die immer noch die CPU verwendet) auf zwei verschiedene Arten beschleunigt. Erstens wird die Zielfunktion in OpenCL implementiert und die Multi-Threaded Optimization Toolbox (MOT) verwendet, um das Monte-Carlo Markow-Chain (MCMC) Sampling datenparallel auf dem Grafikprozessor durchzuführen, um einen Beschleunigungsfaktor von ≈ 7 zu erhalten (von 310 Minuten auf 44 Minuten für einen ausgewählten Hirnschnitt), im Austausch für eine Unterschätzung der Varianzen und verrauschten Verteilungen. Zweitens wird die Schätzung des Glaubwürdigkeitsintervalls (CI) als Regressionsproblem unter Verwendung verallgemeinerter additiver Modelle (GAMs) formuliert. Das MCMC-Sampling wird nur auf einer repräsentativen Teilmenge ($10^2 - 10^3$ Datenpunkte im Vergleich zu $> 10^6$ Datenpunkten) des Datensatzes durchgeführt und die verbleibenden CIs werden vorhergesagt, wodurch die Sampling-Zeit auf einige hundert Sekunden sequentiell und auf einige Sekunden parallelisiert unter Verwendung von bis zu 128 Kernen auf einem einzelnen HPC-Knoten gesenkt wird.

Schließlich wird ein Workflow zur Registrierung von 3D-PLI-Parameterkarten mit Blockface-Bildern vorgestellt, um 3D-PLI-Volumina mit diffusionsgewichteter Bildgebung (DWI) zu korrelieren. Dieser Ablauf besteht aus der zuerst zügigen Auswahl von 3D-PLI Regionen (ROIs), die interaktiv registriert und mit DWI-Volumina korreliert werden. Hierzu wird die bereits etablierte Software `3D-Slicer` genutzt. Im Zuge dessen werden erste Ergebnisse der Korrelation von Retardierung und relativer Dicke vs. Myelinwasserfraktion (MWF) von DWI gezeigt. Die Ergebnisse zeigen eine starke lineare Übereinstimmung, und darüber hinaus zeigen die Korrelationen mit der Transmittanz, dass Bereiche mit geringer Myelinisierung (indiziert anhand MWF) mit einem kombinierten Maß von Retardierung und (lokaler Maxima der) Transmittanz identifiziert werden können.

Acknowledgements

I want to thank Prof. Dr. Markus Axer for the supervision, the long discussions, the guidance during this project, and for making this work between Wuppertal and Jülich possible.

I want to thank Prof. Dr. Katrin Amunts, the Director of the Institute for Neurosciences and Medicine – Structural and Functional Organization of the Brain (INM-1), for all the support, for the scientific discussions, and for providing me with the opportunity to participate in all those conferences and seminars.

I want to thank Dr. Roxana N. Kooijmans for the scientific exchange, for the wonderful lectures, and for the explanation of why HSV is superior to RGB.

A heartfelt thank you to Dr. Felix Matuschke for the insightful discussions on 3D-PLI details and ongoing conversations about programming and software.

Thanks to my colleagues in Wuppertal, Jülich, and Düsseldorf for fostering a warm and friendly environment.

Special thanks to my friends and fellow students who know that Tippen-Tappen-Tönchen is more than just steps. Thanks for the wonderful companionship from day 1. Thanks to Kai, Daniel, and Marvin for proofreading the manuscript. Thanks to my family for sparking my interest in science.

Thank you, Hannah!

Funding

This research has received funding from the European Union's Horizon 2020 Framework Programme for Research and Innovation under the Specific Grant Agreement No. 945539 (Human Brain Project SGA3). In addition, this research was supported by the Helmholtz Joint Lab "Supercomputing and Modeling for the Human Brain". Furthermore, the author gratefully acknowledges the computing time granted through JARA on the supercomputer JURECA at Forschungszentrum Jülich.

Contents

Chapter 1

Introduction

With its 86 billion[1] nerve cells [1], the human brain forms a vast network where each cell is connected to approximately 10,000 others [2]. This dense system underscores the complexity of the brain's connectome [3]. Like any organ, disorders can occur such as Major Depressive Disorder [4], Dementia [5], Alzheimer's [6], Parkinson's [7, 8], Multiple Sclerosis [9], or even seemingly benign ailments like migraines [10], which fundamentally impact the Quality of Life. A better understanding of the human brain can only positively influence our understanding of these diseases and might offer cures in the future. Transfer of this knowledge to fields such as Artificial Intelligence and advances in neuromorphic computing can be made *en passant*. Initiatives like the Human Brain Project (2013-2023) [11] and the Brain Activity Map Project [12] (since 2013) represent significant human endeavors aimed at deepening our understanding of this complex organ. From the HBP, the platform EBRAINS emerged, bundling and summarizing these efforts by providing datasets, atlas services, and simulations, to become a permanent European Infrastructure project, which is desperately needed to ensure these efforts are sustainable. This paves the way for fast iterating between foundational research and clinical applications [11].

In recent years, 3D polarized light imaging (3D-PLI) [13, 14] has emerged as a state-of-the-art imaging technique. Unlike traditional methods dependent on staining, 3D-PLI relies solely on the birefringence of the myelin sheath surrounding the axon, the long projection of nerve cells, which we call fibers in the following. This approach provides an unadulterated view of cortical myeloarchitecture and effectively resolves fiber orientations, the in-plane direction angle (φ) and the out-of-plane direction angle (α) of the axons, in densely white matter, giving each fiber or fiber bundle inside the mounted section a vector representation $\vec{f}(\varphi, \alpha)$. It serves as a perfect bridge between detailed tracing studies and the coarse fiber pathways observed in Diffusion MRI [15, 16, 17]. However, the process of working with thousands of thin histological sections scanned on a micrometer scale introduces significant reconstruction work. Before 3D-PLI can provide us with a microscale connectome, several steps must be taken. This includes data processing, understanding the certainty of fiber orientations, and ensuring correspondence with MRI data, which acts as an important mirror in this exploration.

This thesis starts with a brief overview of the human brain, followed by an exploration of brain preparation principles, 3D-PLI, and its associated mathematical derivations. Subsequently, an automatic workflow of 3D-PLI data is presented, alongside an examination of Uncertainty Analysis. Finally, the thesis concludes with the methodology and correlational analysis of 3D-PLI data with MRI.

[1] (86.1 ± 8.1) billion

Part I

Basics

Chapter 2

The human brain in a Nutshell

Figure 2.1: Korbinian Brodmann (17 November 1868 – 22 August 1918) was a pioneering german neurologist and anatomist who made significant contributions to the field of neuroscience and is especially known for his discovery of Brodmann areas [18].

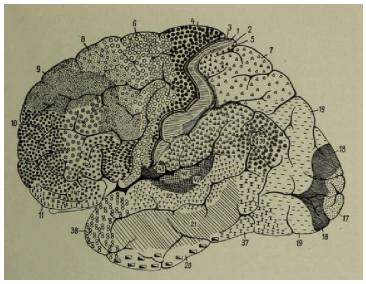

Figure 2.2: One of Brodmann's diagrams of the cerebral cortex using different markings for the discovered Brodmann areas. Each area is attributed a number from 1 to 52. The Broca speech area e. g. is localized at the Brodmann areas 44 and 45 [19].

The brain hides behind a 5 to 8 mm thick skull [20] and is well protected from its surroundings. This makes it not easy to investigate, but at least (to begin with) suggests that it is very fragile. When the brain is extracted from the skull, it can be observed to consist of three distinct regions: the brainstem, the cerebellum, and the cerebrum. The latter can be further easily divided into a left and a right hemisphere, because of the prominent *longitudinal fissure*, leaving mainly one broad bridge between this hemisphere, the *corpus callosum*. Further investigation of the fissures in the cerebrum leads to the four different lobes: the *frontal*, *parietal*, *temporal*, and the *occipital* lobe [21]. If many brains are measured to account for variability, the average weight for female and male brains is 1,198 g (1,336 g) [22], and the average volumes are 1,130 cm^3 (1,260 cm^3) [23].

Taking a look inside the brain, e.g., performing a coronal cut through the middle of the brain, the inner part of the brain appears paler than the outer part, which further serves as a distinction between gray and white matter. At this point, it becomes apparent that the neuroanatomic structures in the brain must be small. In the 19th century, Santiago Ramón y Cajal began studying brain tissue under a microscope after staining them with silver nitrate, a procedure which was developed by Camillo Golgi, to enhance the visibility of the neurons. He was the first then who gave a detailed insight into the field of neuroanatomy and advanced the neuron doctrine [24].

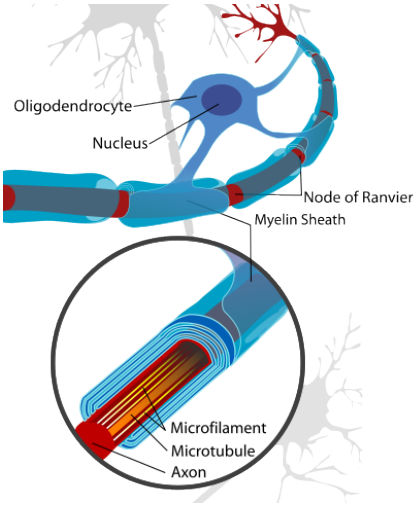

Figure 2.3: The myelin sheath for nerve cells in the central nervous system (CNS) is provided by the oligodendrocytes. By a concentric wrapping of myelin along the axon in segments (separated by the nodes of Ranvier), a jumping propagation of action potentials through the process of saltatory conduction is enabled, allowing for much higher processing speeds. While unmyelinated fibers only allow for a propagation of 0.5 to 10 m/s, the myelinated axons allow a propagation of up to 150 m/s [25].[c]

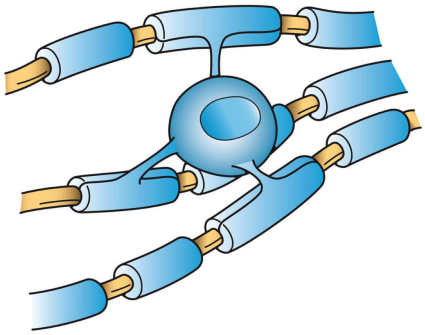

Figure 2.4: An Oligodendrocyte cell can provide a 1 µm thick myelin sheath for about 50 axons [26].[d]

From 1901 to 1910 Korbinian Brodmann (fig. 2.1) started developing his concept of cytoarchitecture. Contrary to Cajal he showed a persistent six-layer structure in Nissl-stained histological sections of the cortex, even across all mammals by considering the architectonic formations of the neurons rather than their specific cell type [18].

Proceeding from this laminar pattern, Brodmann was able to perform a parcellation of the cortex into 52 different *brodmann areas* (fig. 2.2). These distinctive areas are additionally, though not intended in the beginning, inclosing distinctive brain functions e.g., the *Broca* area for speech [27] which corresponds to the areas 44 and 45 [28]. However, Brodmann did not consider that these areas vary in size and shape between different individuals and that these have to be mapped and visualized probabilistically [29, 30, 31, 19]. Additionally, the biased human interpretations must be excluded from the analysis [32].

In 1903 Brodmann described in an article published in the *Journal for Psychology and Neurology*[a], that the birefringence of the myelin sheaths which surrounds the axons (fig. 2.3) of the very prominent nerve cells is not destroyed by the fixation of the tissue with formalin. The myelin is concentrically wrapped around the long axonal projections and is provided by Oligodendrocytes[b] (fig. 2.4) and creates birefringence, because of its anisotropic structure [33].

Myelinated axons can transfer information more quickly (150 m/s) than their unmyelinated counterparts (0.5 to 10 m/s) due to an emergent process called *saltatory conduction* [34].

[a] ger: Journal für Psychologie und Neurologie

[b] In the peripheral nervous system (PNS) the myelin is provided by *Schwann* cells [21].

[c] Public Domain: `https://commons.wikimedia.org/wiki/File:Neuron_with_oligodendrocyte_and_myelin_sheath.svg`.

[d] Artwork by Holly Fischer `https://commons.wikimedia.org/wiki/File:Oligodendrocyte_illustration.png`, „Oligodendrocyte illustration“, `https://creativecommons.org/licenses/by/3.0/legalcode`

Brodmann further described that tissue sections can be studied with a polarization microscope to discover pathological alterations:

> *Erst viel später bin ich auf Formalinpräparate verfallen und habe mit Befriedigung feststellen können, daß Formalinfixierung die Doppelbrechung der markhaltigen Nervenfasern nicht verändert, daß wir also auch in Formalin gehärtete und konservierte Nervenfasern, vorausgesetzt, daß sie in absolut frischem Zustande, so lange noch keine Leichenveränderungen eingetreten sind, in die Fixierungsflüssigkeit gelangen, durch das Polarisationsmikroskop untersuchen und eventuelle krankhafte Veränderungen derselben wahrnehmen können.*

> It was not until much later that I fell for formalin preparations and was pleased to see that formalin fixation does not alter the birefringence of myelinated nerve fibers. Therefore, we can examine nerve fibers hardened and preserved in formalin through the polarizing microscope and observe pathological changes, provided that they enter the fixation fluid in a fresh state, as long as no cadaveric changes have occurred.

– K.Brodmann, 1903

The most common disease which targets the myelin sheath is multiple sclerosis (MS), because of an autoimmune response [35].

This discovery about the possibility of creating fixated specimens where birefringence properties can be investigated, even on completely unstained histological sections, laid the foundation of imaging techniques like 3D Polarized Light Imaging [13, 14].

Today, the human brain is investigated on a cytoarchitectural and fiberarchitectural level. Multiple images methods including Diffusion Weighted Imaging (DWI) [36, 37, 38], Micostructural CT (μCT) [39], PS-OCT [40], Fluorescence Microscopy [41, 42, 43], Electron Microscopy (EM) [44, 45], and Two-Photon Flurescence-Microscopy [46] are therefore used. The holy grail of neuroanatomy of the human brain would be to break down its whole connectome [3, 47]. This is a huge undertaking as the 86 billion cells (see chapter 1) with a variety of shapes and forms [48, 49] are on average connected to about 10,000 other cells: Some of these connections form short-range local networks (e.g., U-fiber networks) and others form longer networks inside a single hemisphere (association fibers) or between the two hemispheres (commissural fibers). And furthermore, the fibers that connect the cortex to the inner nuclei and the spinal cord. To address this variety of scales the prevalent tractography algorithms based on DWI have to be completely revisited to include and to be informed by these details [16].

Chapter 3

From brain preparation to 3D Polarized Light Imaging

Brain research depends on donated human brain tissue. Scientists can only access this tissue through the voluntary donations of individuals who consent to have their brains used for research after death. As confirmed by the ethics committee at the Heinrich Heine University Düsseldorf, postmortem human brain studies do not need any additional approval, if written informed consent of the subject is available.

Examining real brain samples provides invaluable insights that are impossible to gain through other means [50]. To prevent the autolysis of brain tissue the tissue undergoes fixation. A widely established method is the fixation with formalin [51]. The process involves immersing the brain tissue in buffered formalin[1], which cross-links proteins and nucleic acids to preserve the structural integrity of the sample [52]. After 15 days of formalin fixation, the brain is further treated with a glycerin solution for cryoprotection and then frozen at -80°C. Subsequently, the brain is cut into 50 µm thin sections using a cryostat-microtome. Before every cutting, an overview image is taken. This imaging modality is called Blockface imaging. It is the last instance that is not deformed by cutting and embedding and serves as a reference space [53].

As part of this research three unique brain specimens were examined, each obtained through these donation programs, which are, in this thesis named after their location of descent

- Amsterdam Brain
- Düsseldorf Brain
- Chenonceau Brain.

Additional information and the ethical approval or study numbers are given in appendix A. For illustration purposes, a glance at a few selected Blockface images of the Amsterdam Brain, which is sagittally-sectioned, is displayed in fig. 3.1.

[1] Formalin is a solution of formaldehyde. The IUPAC name is methanal.

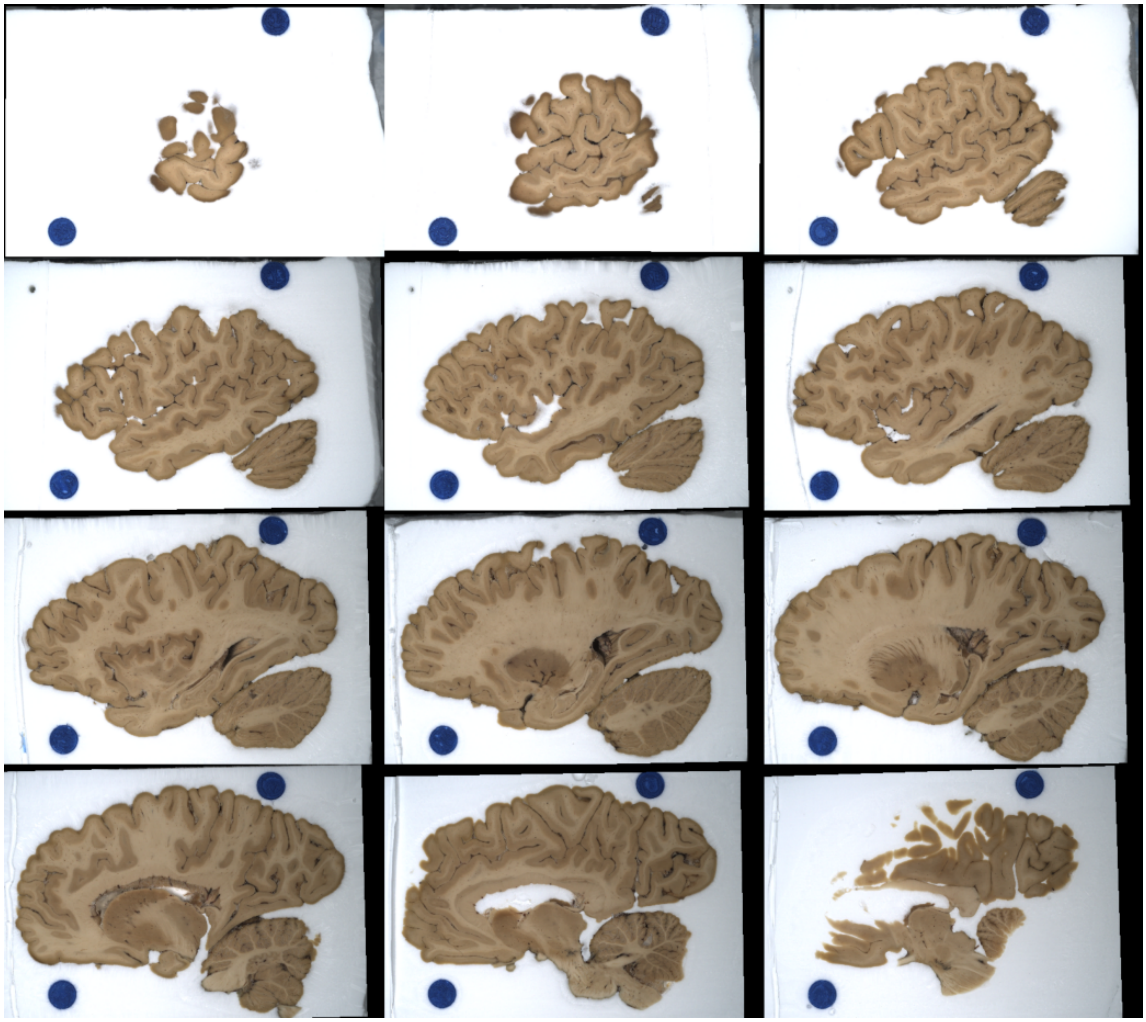

Figure 3.1: Before every cut of a new section an overview image from the embedded brain section is taken. Here, every 100th Blockface image of a left hemisphere of a human brain cut in the sagittal plane is shown. From **Left** to **Right** and **Top** to **Bottom** it starts from the outer cortex and ends before the *longitudinal fissure*. The displayed section numbers are from **Left** to **Right** and **Top** to **Bottom**: 100, 200, 300, ..., 1,200. A detailed description of the preparation of the portrayed brain is given in appendix A.1.

The sections are then, after cutting, carefully placed on glass slides to be mounted into the polarization setup to study the myelinated nerve fibers. For completeness, the lateral (schematic) view of such a nerve cell with the myelinated axon is shown in fig. 3.2. The myelin is wrapped around the axon in concentric circles and creates a duct-tape-like appearance shown in fig. 3.3. Following Brodmann's observation we will now lay out the interaction of (linear) polarized light (see eq. (3.1)) through a fixated brain section.

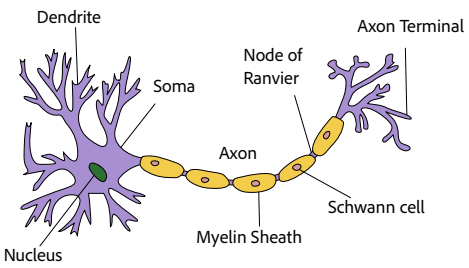

Figure 3.2: Illustration of a nerve cell: The myelin segments with the nodes of Ranvier are located between the dendrite and the terminal. In the (central nervous system) CNS the myelin sheath is provided by oligodendrocytes.[e]

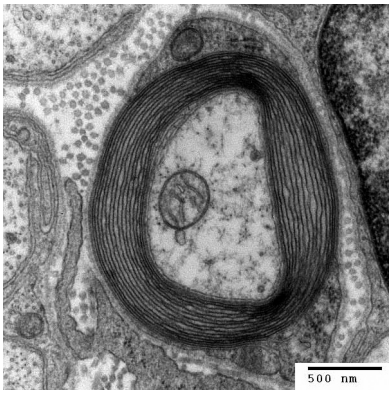

Figure 3.3: Electron microscopy image of the concentric layers of myelin surrounding an axon of a nerve fiber.[f]

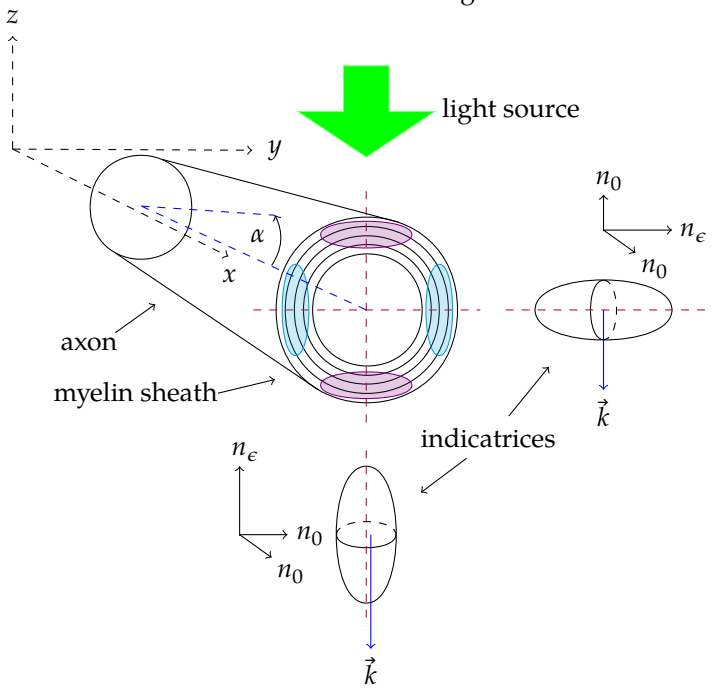

Figure 3.4: The anisotropic structure of the myelin sheath around the axon, here simply schematically sketched as layered concentric circles, leads to uniaxial positive birefringence ($n_o < n_\epsilon$) for every radial myelin segment [54], represented by the vertical and horizontal indicatrices with their respective optical axes (red dashed lines). The fiber is flat (inclined by the inclination angle $\alpha = 0°$), and its direction goes along the x-axis. Light traveling down the z-axis that is polarized along the x-axis travels through the purple and blue area with the same velocity $v_{px} = c/n_o$. However, if the light is polarized along the y-axis, it is slowed down in the blue area (but not in the red area) to $v_{py} = c/n_\epsilon$. Therefore, thin nerve fibers can be modeled as negative uniaxial birefringent ($n_o > n_\epsilon$) objects with their optic axis oriented along their direction because, from this perspective, the extraordinary wave (light polarized along the x-axis) is faster than the ordinary wave (light polarized along the y-axis).

[e]User:Dhp1080 (`https://commons.wikimedia.org/wiki/File:Neuron.svg`), „Neuron“, annotations modified by the author, `https://creativecommons.org/licenses/by-sa/3.0/legalcode`)

[f]Roadnottaken (`https://commons.wikimedia.org/wiki/File:Myelinated_neuron.jpg`), „Myelinated neuron“, `https://creativecommons.org/licenses/by-sa/3.0/legalcode`

The light with the direction along $\vec{k} = k_z$

$$E(z,t) = \mathbf{E}_0 \, \mathrm{e}^{-i(kz-\omega t)} = \begin{pmatrix} E_{x,0} \cdot \mathrm{e}^{-i\Phi_x} \\ E_{y,0} \cdot \mathrm{e}^{-i\Phi_y} \\ 0 \end{pmatrix} \mathrm{e}^{-i(kz-\omega t)}, \tag{3.1}$$

with $\Phi_x = \Phi_y$ and $E_{x,0} = E_{y,0}$ for linear polarization [55], hits the concentric myelin layers around the axon and is mostly influenced by the myelin sheath as visualized in fig. 3.4. For large enough structures nerve fibers can appear as parallel-running lines instead of one (blue areas) or as rings (blue and purple areas) if viewed along the cross-section ($\alpha = 90°$) [33]. Note that for the latter, if the structures are sufficiently small the effect of the blue areas and the purple areas have an equal contribution, but in orthogonal directions. The measured cumulative birefringence is then zero.

The measured birefringence decreases with an increasing Inclination angle α (for which the birefringence of the purple area increases). The cumulated birefringence of a myelinated nerve fiber is negative (phase difference $\delta = \Psi_e - \Psi_o > 0$) with an optical axis in the direction of the nerve fiber [56, 57, 58] and can be approximated as

$$\delta = \Psi_e(\alpha) - \Psi_o = \frac{2\pi t |n_e(\alpha) - n_o|}{\lambda} \tag{3.2}$$

$$\approx \frac{2\pi t \Delta n}{\lambda} \cos^2 \alpha \tag{3.3}$$

$$= \frac{\pi}{2} t_{\mathrm{rel}} \cos^2 \alpha, \tag{3.4}$$

for small difference $\Delta n = |n_e - n_o| \approx 10^{-3} \ldots 10^{-2}$ [59] by Taylor expansion [60]. This has been verified by simulation studies [61]. The relative thickness t_{rel} was introduced in [13, 14].

3.1 Polarized light microscopy

While the first polarization studies, at this time on minerals (apophyllite, amethyst, analcime), were performed by David Brewster [62], it was William H. F. Talbot who first placed samples into an apparatus consisting of two crossed polarizing filters and detailedly described his observations in [63]. The technique is still used in the field of mineralogy and geology and is continuously being improved [64]. Since the discovery of the preserved birefringence of myelinated nerve fibers after the fixation with formalin by Brodmann in 1903, polarization optics have been widely used to study the human brain [65, 66, 67].

The polarization microscopes presented in this chapter are either developed by the Institute of Neuroscience and Medicine 1 (INM-1) at the Forschungszentrum Jülich GmbH or by Taorad GmbH (Herzogenrath, Germany).

3.2 Large Area Polarimeter (LAP)

The first is the Large Area Polarimeter (LAP) in which the brain sections can be scanned as a whole with a wide field of view of $300 \times 300\,\mathrm{mm}^2$. This is realized via a large illumination array consisting of 32×32 LEDs and large polarizing filters as it can be seen in fig. 3.5. Furthermore, it comes with the possibility of tilting the specimen stage in four different directions (north, east, south, and west). A sketch of the layout of the optical components can be viewed in fig. 3.6.

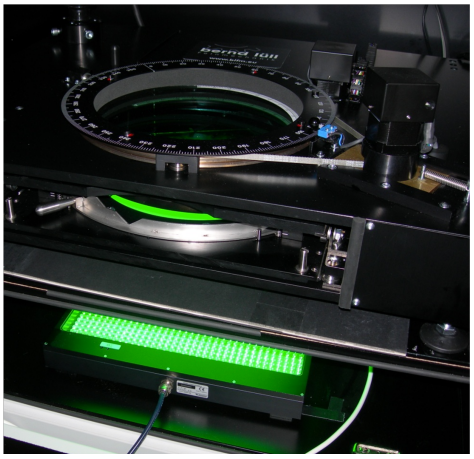

Figure 3.5: Front view of the optical components in the LAP: The LAP is constructed in a very modular fashion. Every component is installed on a shelf. At the bottom is the LED Panel for illumination, above that are the rotating filters. Then comes the sample stage which can be tilted in four different directions. Above the sample stage, on the top (which cannot be seen in the image), is the camera.

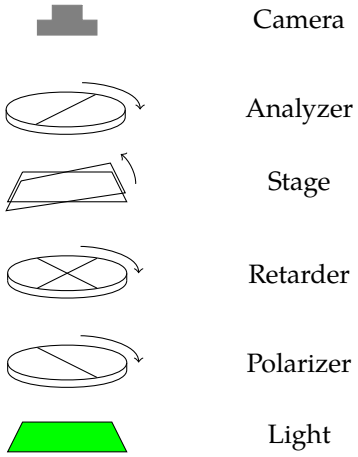

Figure 3.6: Sketch of the used components in the LAP: The moving components are the polarizer, the retarder, and the analyzer. They rotate counterclockwise with respect to the perspective of the light. The sample stage is covered by the field of view of the camera and can be tilted in four different directions.

When the brain section is placed onto the specimen stage, the polarizer, analyzer, and retarder are rotating counterclockwise with respect to the light. The rotation goes from 0° to 170° in steps of 10°, resulting in 18 measurements. After the flat measurement is taken, the specimen stage is tilted under an angle of $\tau = 8°$ in four different directions (north, east, south, west) and for each of these four oblique views the scanning is repeated. In this way, for every camera pixel, five signal curves are aquired.

The produced data of the LAP for the flat measurement and the four oblique measurements with the tilted specimen stage of $\tau = 8°$ is about $(1 + 4) \times 892\,\text{MB} = 4.5\,\text{GB}$ for a size of $W \times H = 4164 \times 3120$ and $N = 18$ rotation angles. And $5 \times 396\,\text{MB} = 2.0\,\text{GB}$ for a size of $W \times H = 2776 \times 2080$, respectively.

3.3 Large Metripol Polarimeter 3D (LMP-3D)

The Large Metripol Polarimeter 3D (LMP-3D) realizes the oblique views on a microscopic scale of 1.85 µm via a moving aperture in a Köhler Illumination Setting because the mechanical tilting approach of the LAP is not applicable at this resolution [60]. In contrast to the very modular structure of the LAP where each component is very large and visible (fig. 3.5), the design of the LMP-3D is much more compact, and the moving components are hidden (see fig. 3.7). The polarized light and the selection of the oblique illumination angle are produced in the upper part of the microscope (see fig. 3.8). The Retarder and the Analyzer are fixed and are located below the surface and the XY-Stage.

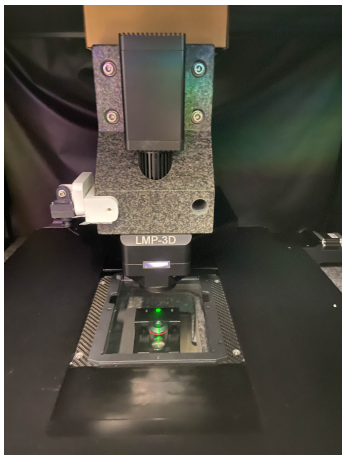

Figure 3.7: Front view of the optical components in the LMP-3D: The upper part with the engraving includes the light source with the Köhler illumination and below the sample stage is the camera.

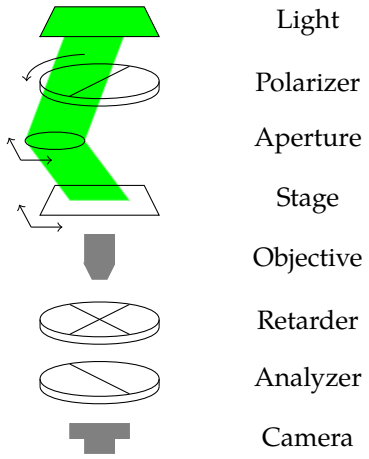

Figure 3.8: Sketch of the used components in LMP-3D: The moving components are the polarizer after the light source which turns counterclockwise, the aperture which can be moved in the xy-plane to create the oblique illumination, and the sample stage which can be moved to scan the specimen tile-wise.

Because of the small field of view of 3.8 mm^2 with a pixel size of 1.85 µm the inserted specimen is mounted onto an XY-Stage and scanned tilewise with an overlap of $\approx$ 30%, each scanned tile has a size of 2048 × 2048 pixel. During the scan, the polarizer is rotating from 0° to 160° with a stepsize of 20° resulting in 9 rotations angles. This is half the number of rotation angles than the LAP of 18 in order to save storage space. Analog to the LAP, the measurement is then repeated for four different shifted apertures (2.5 mm from the center position each, which translates to an oblique view angle of $\tau = 3.9°$), resulting in four different oblique views. The detailed specifications are given in appendix B.

For a large *sagittale* section, this results into Column (C) × Row (R) = 38 × 52 tiles á 2048 × 2048 pixel for one flat and four oblique measurements consisting of 9 rotation angles each. Considering that the `dtype` of these arrays are `float32`, this leads to a storage consumption of $\approx$ 5 × 33 GB × 9 $\approx$ 1.5 TB raw data per dataset. The mean image of such a scan is shown in fig. 3.9.

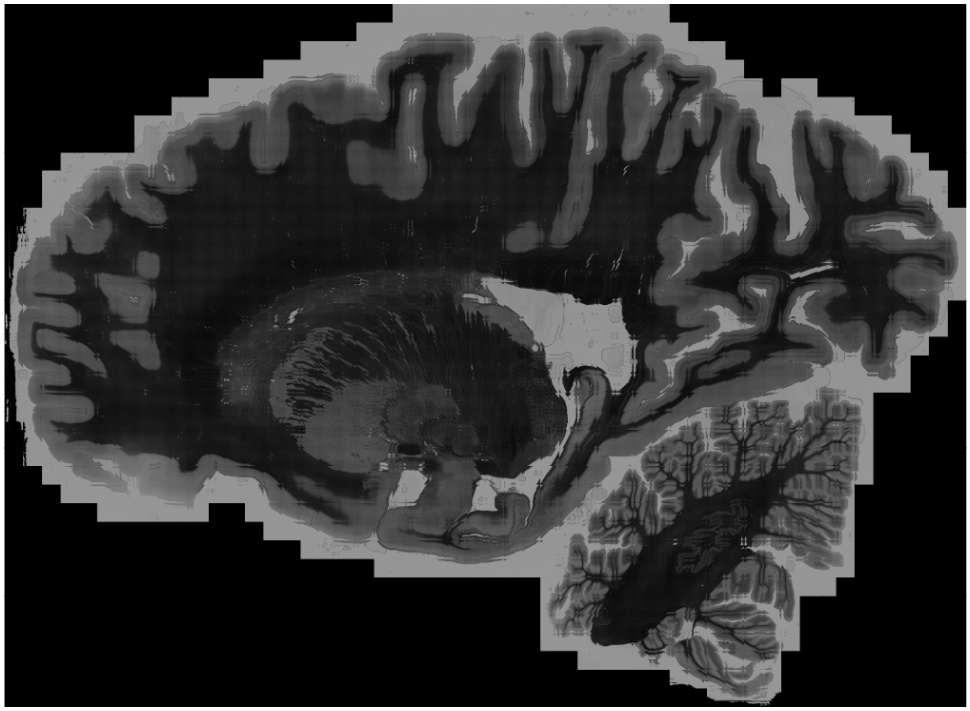

Figure 3.9: Tilewise scanned *sagittale* human brain section with 38 × 52 tiles á 2048 × 2048 pixel with a pixelsize of 1.85 µm: The original file of this preview has a filesize of ≈ 33 GB.

The raw data is stored and archived on the **Ju**elich **S**torage **C**luster (JuST) accessible via the **Ju**elich **D**ata **A**ccess (JuDAC) server located in the Jülich Supercomputing Centre (JSC) in Jülich. This infrastructure is connected to the **Ju**elich **R**esearch on **E**xascale **C**luster **A**rchitectures - **D**ata **C**entric (JuRECA-DC) supercomputer [68] where the data processing is performed.

Chapter 4

Directional Analysis of 3D Polarized Light Imaging

In the polarizing microscope (fig. 3.8) the only rotating part (around the angle ρ) is the first linear polarizer which generates polarized light $E[\rho] = R[\rho]E_y$. This polarized light hits the fiber which can be modeled as a wave retarder $M_{\text{ret}}[\zeta =: \delta/2]$ rotated in-plane by the Direction angle φ. After that, the light goes through a quarterwave-retarder $M_{\text{ret}}[\pi/4]$ which is rotated by $-45°$. (For completeness both cases $\pm 45°$ are considered.) Finally, the light goes through a linear polarizer P_y before it is captured by the camera sensor. For ideal optical components, fully polarized light, and non-attenuating tissue[1], the components can be represented as two-dimensional Jones matrices by the Jones calculus [70]. The expected light intensity is then calculated by multiplication of these matrices and taking the sum of squares

$$
\begin{aligned}
I_{\text{PLI}}(\rho) &= \left| P_x \cdot R\left[\pm\frac{\pi}{4}\right] \cdot M_{\text{ret}}\left[\frac{\pi}{4}\right] \cdot R\left[\mp\frac{\pi}{4}\right] \cdot R[\varphi] \cdot M_{\text{ret}}[\zeta] \cdot R[-\varphi] \cdot E[\rho] \right|^2 \\
&= \left| \begin{pmatrix} 1 & 0 \\ 0 & 0 \end{pmatrix} \begin{pmatrix} \cos\left(\frac{\pi}{4}\right) & \mp\sin\left(\frac{\pi}{4}\right) \\ \pm\sin\left(\frac{\pi}{4}\right) & \cos\left(\frac{\pi}{4}\right) \end{pmatrix} \begin{pmatrix} e^{\frac{i\pi}{4}} & 0 \\ 0 & e^{\frac{-i\pi}{4}} \end{pmatrix} \begin{pmatrix} \cos\left(\frac{\pi}{4}\right) & \pm\sin\left(\frac{\pi}{4}\right) \\ \mp\sin\left(\frac{\pi}{4}\right) & \cos\left(\frac{\pi}{4}\right) \end{pmatrix} \right. \\
&\qquad \left. \begin{pmatrix} \cos(\varphi) & -\sin(\varphi) \\ \sin(\varphi) & \cos(\varphi) \end{pmatrix} \begin{pmatrix} e^{i\zeta} & 0 \\ 0 & e^{-i\zeta} \end{pmatrix} \begin{pmatrix} \cos(\varphi) & \sin(\varphi) \\ -\sin(\varphi) & \cos(\varphi) \end{pmatrix} \begin{pmatrix} -\sin\rho \\ \cos\rho \end{pmatrix} \right|^2 I_0 \\
&= \left| \begin{pmatrix} 1 & 0 \\ 0 & 0 \end{pmatrix} \begin{pmatrix} \frac{1}{\sqrt{2}} & \pm\frac{i}{\sqrt{2}} \\ \pm\frac{i}{\sqrt{2}} & \frac{1}{\sqrt{2}} \end{pmatrix} \right. \\
&\qquad \left. \begin{pmatrix} \cos(\zeta) + i\sin(\zeta)\cos(2\varphi) & i\sin(\zeta)\sin(2\varphi) \\ i\sin(\zeta)\sin(2\varphi) & \cos(\zeta) - i\sin(\zeta)\cos(2\varphi) \end{pmatrix} \begin{pmatrix} -\sin\rho \\ \cos\rho \end{pmatrix} \right|^2 I_0 \\
&= \frac{I_0}{2}[1 \mp \sin(2\zeta)\sin(2\rho - 2\varphi)].
\end{aligned}
$$

The calculation can be analogously performed for the Large Area Polarimeter (fig. 3.6) and yields the same result.

[1] In a non-ideal world, with partially polarized light and attenuation the light and the optical components can be modeled via Müller Calculus, see 69.

During the tilting process, whether it is the mechanical tilting with a specimen stage or the creation of an oblique illumination angle through shifting the aperture in the Koehler Illumination of the LMP-3D, the Direction φ and the Retardation $\delta := 2\zeta$ vary. The resulting PLI formula can be expressed as

$$I(I_T, \varphi', \sin\delta'; \rho) = \frac{T}{2}\,(1 + \sin(2\rho - 2\varphi')\,\sin\delta'),$$

with

$$\begin{aligned}\varphi'(\alpha,\varphi,\tau,\psi) = \operatorname{arctan2}\Big(&\sin(\alpha)\sin(\tau)\cos(\psi) + \cos(\alpha)\cos(\varphi)\left(\cos(\tau)\cos^2(\psi) + \sin^2(\psi)\right)\Big)\\ &- 2\cos(\alpha)\sin^2\left(\frac{\tau}{2}\right)\sin(\psi)\cos(\psi)\sin(\varphi),\\ &(\sin(\alpha)\sin(\tau)\sin(\psi) + \cos(\alpha)(\cos(\tau)\sin(\psi)\cos(\phi-\psi) + \cos(\psi)\sin(\phi-\psi)))\,,\end{aligned}$$

and

$$\begin{aligned}\sin\delta'(t'_{rel}(t_{rel},\tau),\alpha'(\alpha,\varphi,\tau,\psi)) &= \sin\left(\frac{\pi}{2}\frac{t_{rel}}{\cos\tau}\cos^2(\alpha'(\alpha,\varphi,\tau,\psi))\right)\\ &= \sin\left(\frac{\pi}{2}\frac{t_{rel}}{\cos\tau}\left(1 - (\sin(\alpha)\cos(\tau) - \cos(\alpha)\sin(\tau)\cos(\varphi-\psi))^2\right)\right),\end{aligned}$$

where τ is the angle of the oblique illumination inside the tissue and ψ is the Direction from which the oblique illumination is coming. The derivation of the (τ dependent) oblique rel. Thickness t'_{rel} from the Retardation expression

$$\frac{\pi}{2} t_{\mathrm{rel}} \cos^2\alpha \tag{4.1}$$

is the easy part because the experienced thickness of the tissue by the light can be expressed by simple trigonometry as

$$t'_{\mathrm{rel}}(t_{\mathrm{rel}},\tau) = \frac{t_{\mathrm{rel}}}{\cos\tau}, \tag{4.2}$$

see [60]. But for the Retardation which depends on the Inclination α, and also for the Direction φ the acting of the rotation matrices $R_{\mathrm{obl.}}(\tau,\psi) = R_z(\psi)\cdot R_y(\tau)\cdot R_z(\psi)$ on the fiber vector $\vec{f}(\alpha,\varphi)$

$$R_{\mathrm{obl.}}(\tau,\psi)\cdot\vec{f}(\alpha,\varphi) = \begin{pmatrix}\cos(\psi) & -\sin(\psi) & 0\\ \sin(\psi) & \cos(\psi) & 0\\ 0 & 0 & 1\end{pmatrix}\begin{pmatrix}\cos(\tau) & 0 & \sin(\tau)\\ 0 & 1 & 0\\ -\sin(\tau) & 0 & \cos(\tau)\end{pmatrix} \tag{4.3}$$

$$\begin{pmatrix}\cos(\psi) & \sin(\psi) & 0\\ -\sin(\psi) & \cos(\psi) & 0\\ 0 & 0 & 1\end{pmatrix}\cdot\begin{pmatrix}\cos\alpha\cos\phi\\ \cos\alpha\sin\phi\\ \sin\alpha\end{pmatrix} \tag{4.4}$$

has to be considered.

This expression can be simplified to

$$\vec{f}'(\alpha,\varphi) = R_{\text{obl.}}(\tau,\psi)\cdot\vec{f}(\alpha,\varphi) \tag{4.5}$$

$$= \begin{pmatrix} \cos(\tau)\cos^2(\psi)+\sin^2(\psi) & ((\cos(\tau)-1)\cos(\psi))\sin(\psi) & \cos(\psi)\sin(\tau) \\ ((\cos(\tau)-1)\cos(\psi))\sin(\psi) & \cos^2(\psi)+\cos(\tau)\sin^2(\psi) & \sin(\tau)\sin(\psi) \\ -\cos(\psi)\sin(\tau) & -\sin(\tau)\sin(\psi) & \cos(\tau) \end{pmatrix} \begin{pmatrix} \cos(\alpha)\cos(\varphi) \\ \cos(\alpha)\sin(\varphi) \\ \sin(\alpha) \end{pmatrix} \tag{4.6}$$

$$= \begin{pmatrix} \sin\alpha\sin\tau\cos\psi+\cos\alpha\cos\varphi(\cos\tau\cos^2\psi+\sin^2\psi)-2\cos\alpha\sin^2\frac{\tau}{2}\sin\psi\cos\psi\sin\varphi \\ \sin\alpha\sin\tau\sin\psi+\cos\alpha(\cos\tau\sin\psi\cos(\varphi-\psi)+\cos\psi\sin(\varphi-\psi)) \\ \sin\alpha\cos\tau-\cos\alpha\sin\tau\cos(\varphi-\psi) \end{pmatrix}, \tag{4.7}$$

the new angles can then be obtained via

$$\varphi'(\alpha,\varphi,\tau,\psi) = \operatorname{arctan2}\left(\vec{f}'_1,\vec{f}'_2\right), \tag{4.8}$$

$$\alpha'(\alpha,\varphi,\tau,\psi) = \arcsin\vec{f}'_3, \tag{4.9}$$

yielding the desired expression. Note that the order of arguments in arctan2 functions in programming languages can differ. In `Python` it is `atan2(y,x)`[2] and in `Mathematica` it is `ArcTan(x,y)`[3]. Here, we are using the latter. The derived form is significantly more explicit than [71] and can be easily implemented in any programming language with scalar functions alone and no extra looping along matrix indices is needed. The `Mathematica` encoded derivation can be found in appendix C.

[2] `https://docs.python.org/3/library/math.html#math.atan2`
[3] `https://reference.wolfram.com/language/ref/ArcTan.html`

4.1 Established 3D-PLI analysis

Here, a short overview of the established 3D-PLI analysis consisting of calibration, Fourier analysis [14, 13], and Least Squares Analysis [71] is given.

4.1.1 Calibration

Before every analysis, the data has to be calibrated. This is necessary because the field of view of the microscope is not homogeneous. For this reason, empty measurements are taken from the LAP and the LMP-3D. After averaging the measurements to obtain the normalization coefficients, the data (or raw data) is divided by these normalization coefficients.

4.1.2 Fourier Analysis

The measurement data of the LAP has `2776 x 2080` or `4164 x 3120` pixels per section. For the microscopic LMP-3D, it goes up to `118697 x 85055` for a large sagittal brain section. For an analysis to work on about 10^{10} pixel (or voxel if the thickness of the brain section is considered), it must work in parallel. Because of the sinusoidal form of the PLI signal *behind* every pixel it seems natural to apply (vectorized) Fourier analysis to extract the mean and the phase

$$a_0 = \frac{1}{N}\sum_{i=0}^{N-1} I_i = \frac{I_T}{2}, \tag{4.10}$$

$$a_2 = \frac{2}{N}\sum_{i=0}^{N-1} I_i \cos 2\rho_i = -\frac{I_T}{2}\sin\delta\sin 2\varphi, \tag{4.11}$$

$$b_2 = \frac{2}{N}\sum_{i=0}^{N-1} I_i \sin 2\rho_i = \frac{I_T}{2}\sin\delta\cos 2\varphi. \tag{4.12}$$

Solving for I_T, φ and $\sin\delta$ and using basic trigonometry yields

$$I_T = 2a_0, \tag{4.13}$$

$$\varphi = \frac{1}{2}\arctan 2\left(-a_2, b_2\right), \tag{4.14}$$

$$\sin\delta = \frac{\sqrt{a_1^2 + b_1^1}}{a_0}. \tag{4.15}$$

Here, I_T is the image transmittance, corresponding to the light that passes the tissue on average [13, 14]. The angle φ is the in-plane orientation, the Direction of the fiber. The value $\sin\delta$ is a measure for the birefringence strength, where

$$\delta = \frac{2\pi t\Delta n}{\lambda}\cdot\cos^2\alpha = \frac{\pi}{2}t_{\text{rel}}\cos^2\alpha \tag{4.16}$$

as previously derived. Visually, the Direction φ corresponds to the phase of the signal, the Retardation $\sin\delta$ corresponds to the peak-to-peak distance of the signal and a_0 corresponds to the mean of the signal as seen in fig. 4.1.

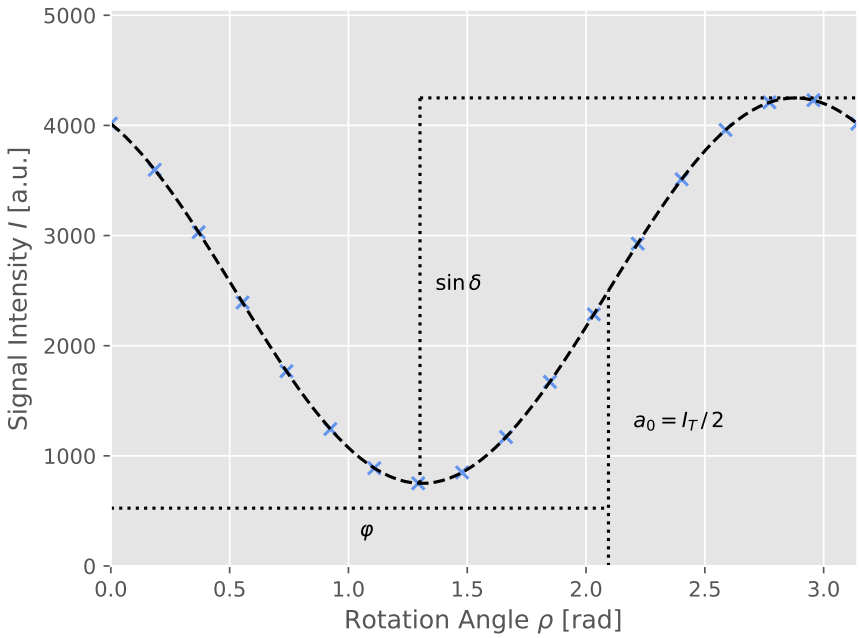

Figure 4.1: The PLI signal (black dashed line) gets sampled across the rotation angles (blue crosses). From the Fourier analysis, we obtain the annotated values: The Retardation $\sin\delta$, the Transmittance $I_T = 2a_0$, and the Direction φ.

The image modalities Transmittance, Direction, and Retardation can then be visualized with a suitable colormap as seen in fig. 4.2.

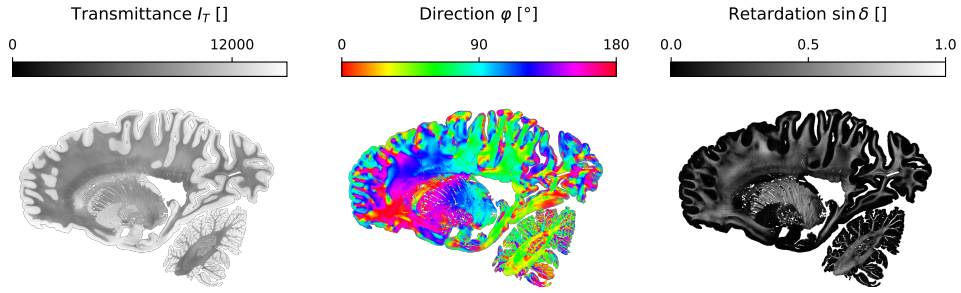

Figure 4.2: After the Fourier analysis is applied to the data (x,y,z) for every signal in z in every tuple (x,y), the resulting modalities Transmittance I_T, Direction φ, and Retardation $\sin\delta$ can be visualized with a suitable colormap. The Transmittance and Retardation are visualized with a linear colormap, and the Direction is visualized with the cyclic colormap `hsv` to satisfy the periodic boundaries.

4.1.3 Least Squares Fitting

The signal analysis via Fourier analysis gives only one orientation, the in-plane-direction or Direction φ, but the fiber orientations reside in three dimensions. In order to extract the out-of-plane orientation, the Inclination α, the information of the oblique views is used.

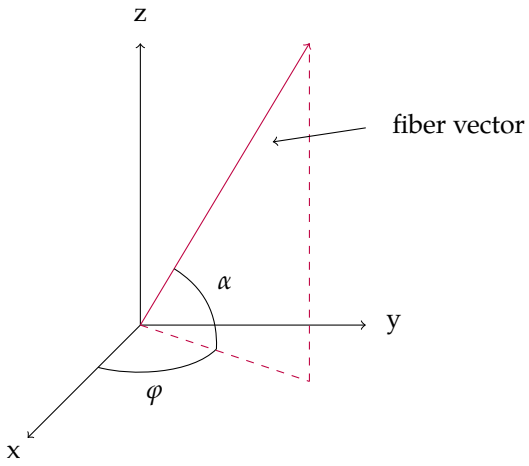

Figure 4.3: The fiber orientation is defined by the two angles Direction φ and Inclination α, creating the red fiber vector r. The value range for this angles is $\alpha \in [-\pi/2, \pi/2)$ and $\varphi \in [0, \pi)$.

Following the previously derived expression for the 3D-PLI model

$$\hat{I}(I_T, \varphi, \alpha, t_{\text{rel}}; \tau, \psi, \rho) = \frac{I_T}{2}\left(1 + \sin(2\rho - 2\varphi'(\alpha, \varphi, \tau, \psi))\ \sin\delta'(t'_{rel}(t_{rel}, \tau), \alpha'(\alpha, \varphi, \tau, \psi))\right)$$

we create the objective function J for the least squares fitting by simply summing the square differences of the model function and the measured signal $I_{\tau,\psi,\rho}$ for the tilt amplitudes $\tau = 0$, $\tau \neq 0$, and all respective tilt directions ψ

$$J(I_T, \varphi, \alpha, t_{\text{rel}}, I) = \sum_{\tau,\psi,\rho}\left(\frac{\hat{I}(I_T, \varphi, \alpha, t_{\text{rel}}; \tau, \psi, \rho) - I_{\tau,\psi,\rho}}{\sigma_{\tau,\psi,\rho}}\right)^2. \tag{4.17}$$

Note that τ must be corrected for the refractive index of brain tissue $n \approx 1.45$ [71, 72] according to snells law [73]. The objective function can be simplified by normalizing with I_T because this value does not need to be fitted, yielding the optimization problem of $\tilde{J}$ instead of J

$$\arg\min_{\varphi,\alpha,t_{\text{rel}}} \tilde{J}(\varphi, \alpha, t_{\text{rel}}, I), \tag{4.18}$$

which can be solved via the Levenberg-Marquardt algorithm, after a brute-force initialization via grid-search for the parameters α and t_{rel} [71]. The variance $\sigma^2_{\tau,\psi,\rho}$ is obtained via multiplying the microscopes g with the Intensities $I_{\tau,\psi,\rho}$. For the LAP with $g = 3$, this means $\sigma_{\tau,\psi,\rho} = \sqrt{3 \cdot I_{\tau,\psi,\rho}}$.

Because of the large number of pixels the first version of the algorithm, named **R**obust **O**rientation **F**itting via **L**east **S**quares algorithm (**ROFL** algorithm), was implemented in `numba` [74] and `mpi4py` [75] for compiled parallel execution. For further speedup, the algorithm was implemented on the GPU (`goROFL`) [76] with the `Gpufit` library [77]. The resulting image modalities Direction, Inclination, and rel. Thickness can then be visualized with a suitable colormap as seen in fig. 4.4.

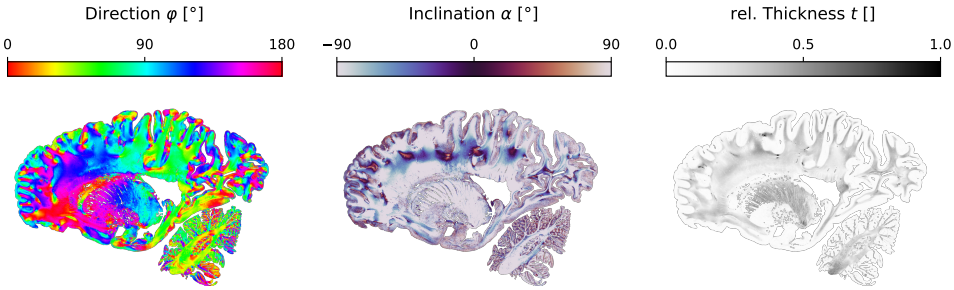

Figure 4.4: After the least squares fitting is applied to the data (x,y,z) for every signal in z in every tuple (x,y), the resulting modalities Direction φ, Inclination α, and rel. Thickness t_{rel} can be visualized with a suitable colormap. The relative Thickness is visualized with a linear colormap, and the Direction and Inclination are visualized with cyclic colormaps to satisfy the periodic boundaries.

The chosen colormap `hsv` for the Direction angle φ is a result of the periodic (from 0° to 360° periodic) `hue` value. Furthermore, the Inclination angle α can be incorporated via the `saturation` and the `value` of the HSV color space. The mapping to the HSV color space is then expressed as

$$H = 2\varphi \tag{4.19}$$

$$S = 1 \tag{4.20}$$

$$V = 1 - 2|\alpha|/\pi. \tag{4.21}$$

The result of this mapping applied to the Direction and Inclination maps of fig. 4.4 is shown in fig. 4.5.

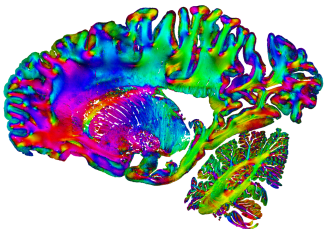

Figure 4.5: Application of the Direction and Inclination mapping to the HSV colorspace. Areas with more inclined fibers appear darker.

Part II

3D Polarized Light Imaging meets High-Performance Computing

Chapter 5

Towards an automatic workflow on HPC

Since the introduction of 3D Polarized Light Imaging (3D-PLI) at 100 µm in 2011 with the Large Area Polarimeter (LAP) [13], the technique of 3D-PLI was quickly improved pixel-wise (down to 1.3 µm) by the introduction of the Polarizing Microscope (PM), and reconstruction-wise by the extension of the LAP by a tiltable specimen-stage to tackle the sign-ambiguity of the Inclination angle [14]. In 2016 Wiese developed in his dissertation the prototype of a Polarizing Microscope with oblique views by using a Koehler illumination system which made the Inclination sign also finally accessible at 1.85 µm [60]. Given the dimensions of the human brain resulting in about 3,000 histological sections of 50 µm thickness that need to be scanned, calibrated, processed, and archived, a manual workflow becomes quickly unbearable. If we then consider the resolution of 1.85 µm, resulting in up to 10^9 voxel per histological section which is obtained for $N = 9$ rotation angles and $M = 4$ additional oblique views, the petabyte regime is reached.

The issue then becomes twofold: The workflow to analyze the data has to be clearly outlined from the preprocessing to the final result to ensure reproducibility, repeatability and a high level of automation. Furthermore, the workflow needs to be able to handle large amounts of data concerning data handling and computing.

First, in section 5.1, the storage of the measurement data and the metadata is addressed. Then, in section 5.2, a new software testing approach based on this saving scheme is presented. After outlining and ensuring that the workflow is running on HPC (see section 5.3), two updates are introduced. In the first update, the (see section 5.4) Least Squares Analysis is parallelized in order to use multiple GPUs and in the second update (see section 5.5) denoising of the measurement data based on Independent Component Analysis (ICA) is added.

Parts of this chapter have been previously published in

- Benning, K., Menzel, M., Reuter, J.A., Axer, M. (2021). Independent Component Analysis for Noise and Artifact Removal in Three-Dimensional Polarized Light Imaging. In: Amunts, K., Grandinetti, L., Lippert, T., Petkov, N. (eds) Brain-Inspired Computing. BrainComp 2019. Lecture Notes in Computer Science(), vol 12339. Springer, Cham. https://doi.org/10.1007/978-3-030-82427-3_7.

5.1 Data and Metadata

The raw data is saved in the Hierarchical Data Format 5 (HDF5), which allows storing large arrays together with the corresponding metadata so that the file becomes self-describing [78]. The array itself and its attributes are saved under the Group `"/"` in the Dataset `"Image"`. In the case of the raw data, the shape `(X, Y, N)` can be identified with the image width, the image height, and the number of analyzer angles. A few of these attributes which are fundamental for further processing are listed in table 5.1.

```
GROUP "/" {
   DATASET "Image" {
      DATATYPE  H5T\_STD\_U16LE
      DATASPACE  SIMPLE { ( X, Y, N ) / ( X, Y, N ) }
   }
   ATTRIBUTE "FOO" {
      DATATYPE  H5T\_STD\_I32LE
      DATASPACE  SCALAR
      DATA {
      (0): 42
      }
   ...
   }
}
```

Table 5.1: Selected Measurement Attributes for the Raw Data

Attributes	**Values LAP**	**Values PM**
analyzer_start_angle	0	0
analyzer_step_size	10	20
data_source	LAP	PM
direction_offset	0	54
measurement_time	JJJJ-MM-DD hh:mm:ss	JJJJ-MM-DD hh:mm:ss
samples_per_pixel	18	9
tilt_amplitude	$\in \{0°, 8°\}$	$\in \{0\,\text{mm}, 2.5\,\text{mm}\}$
tilt_direction	$\in \{0°, 90°, 180°, 270°\}$	$\in \{0°, 90°, 180°, 270°\}$

For both instruments, the LAP and the PM, which are internally described as `data_source`, the `analyzer_start_angle` of the analyzer is defined as 0. The LAP has a smaller `analyzer_step_size` of 10 than the PM which has a `analyzer_step_size` 20, because of the higher data consumption of the latter. Therefore the attributes `samples_per_pixel` equals 18 (or 9) for a full analyzer run of 180°. Because the appearing Direction $\tilde{\varphi}$ of a fiber can differ from the real Direction φ due to a rotational offset of the built-in filter, the attribute `direction_offset` defines the offset angle φ_{offset}. The Direction φ is then obtained by $\varphi = \tilde{\varphi} + \varphi_{\text{offset}}$.

The mapping of the flat measurement with the associated oblique views is performed via the attribute `measurement_time`. The angle for the amplitude τ of the oblique view and the tilt direction Ψ is given by the attributes `tilt_amptlitude` and `tilt_direction`. The flat measurement has hereby an amplitude of $\tau = 0°$ and a tilt direction of $\psi = 0°$ by convention. Whereas the LAP achieves a clearly defined angle equal to the tilt amplitude τ by tilting the stage, the PM generates oblique views through a 2.5 mm

aperture shift from the center position, using the Köhler Illumination setting.[1]

The self-describing HDF5 files can be given to a CLI call of the specific program without further measurement-specific options. Therefore errors when working with a specific program interactively are minimized, because the most important parameters are encapsulated and are read by the program directly as shown in listing 5.1.

Listing 5.1: Scheme of an analysis-tool application

```
analysis-tool foo_path/foo.h5 bar_path/bar.h5 -o output_path/
```

Furthermore, when setting up a pipeline no additional CLI arguments have to be provided.

5.2 Software Testing

To ensure the proper working of the directional analysis software for generating synthetic 3D-PLI data with oblique views and quick visualization was developed.

5.2.1 Introduction

Synthetic data should prove the consistency and reproducibility of the directional analysis tooling. But because of the self-describing HDF5 files, for testing the program, the test data must also have the right format with the corresponding attributes. For this reason, the software `synPLI` was developed. It builds upon the in-house tools for file-reading, metadata processing, and metadata validation to be close to the workflow implementation on the HPC system. This makes end-to-end testing possible, to ensure the desired analysis behavior and spot integration issues early.

5.2.2 Development

The derived and simplified PLI formula (see eq. (4.8) and eq. (4.9)) is implemented in Python with `numpy` [79] and `numba` [74] as external libraries. The CLI tool parses values for Transmittance, Direction, Inclination, and t_{rel} and outputs the signal datasets (of the flat and the oblique views) and the corresponding *ground truth* modalities. The software is written in a way that if multiple values are given e.g., for the Inclination α, the cartesian product of the values is evaluated. If for example the user types into the terminal the expression of listing 5.2.

Listing 5.2: Example `synPLI` CLI call

```
synpli-tilt --transmittance 5000.0 \
            --direction 45 \
            --inclination $(seq -80 2 80 ) \
            --trel 0.8 \
            --output .
```

,

the user should obtain 9×9 signals from an Inclination starting at $\alpha = -80°$ to an Inclination of $\alpha = 80°$ in a stepsize of two, with constant values for $t_{\text{rel}} = 0.8$ and $\varphi = 45°$ If the length of the cartesian product is not a square number the generated signal sequences are filled up with zeros up to the next square number. In either case, a boolean mask is generated specifying which pixel values are valid.

[1] The oblique view angle of the LMP-3D has been measured as $\tau = 3.9°$.

5.2.3 Results

After execution of the software the specified folder contains e.g., files for the flat measurements and the oblique views, and files for the Transmittance, Inclination, t_{rel}, Retardation (calculated from Inclination and t_{rel}) as seen in listing 5.3. The flat measurement and the oblique views are per definition calibrated.

Listing 5.3: Content of the `synPLI` output folder

```
$ tree
.
|-- Synpli_Calibrated_Flat.h5
|-- Synpli_Calibrated_Tilted_1.h5
|-- Synpli_Calibrated_Tilted_2.h5
|-- Synpli_Calibrated_Tilted_3.h5
|-- Synpli_Calibrated_Tilted_4.h5
|-- Synpli_Direction_Flat.h5
|-- Synpli_Inclination_Flat.h5
|-- Synpli_Mask_Flat.h5
|-- Synpli_Retardation_Flat.h5
|-- Synpli_Transmittance_Flat.h5
`-- Synpli_Trel_Flat.h5
```

Inspection of the Inclination file yields the content of listing 5.4. Here, it can be seen how the Inclination values α are increasing over the dataspace from `(0,0)` to `(8,8)`.

Listing 5.4: Dataset `Image` of the Inclination file

```
GROUP "/" {
   DATASET "Image" {
      DATATYPE  H5T_IEEE_F32LE
      DATASPACE  SIMPLE { ( 9, 9 ) / ( 9, 9 ) }
      DATA {
      (0,0): -80, -78, -76, -74, -72, -70, -68, -66, -64,
      (1,0): -62, -60, -58, -56, -54, -52, -50, -48, -46,
      (2,0): -44, -42, -40, -38, -36, -34, -32, -30, -28,
      (3,0): -26, -24, -22, -20, -18, -16, -14, -12, -10,
      (4,0): -8, -6, -4, -2, 0, 2, 4, 6, 8,
      (5,0): 10, 12, 14, 16, 18, 20, 22, 24, 26,
      (6,0): 28, 30, 32, 34, 36, 38, 40, 42, 44,
      (7,0): 46, 48, 50, 52, 54, 56, 58, 60, 62,
      (8,0): 64, 66, 68, 70, 72, 74, 76, 78, 80
      }
...
}
```

The content of the signal files of the flat- and oblique signal files are shown in fig. 5.1. It can be seen that for an inclined fiber, here in a synthetic setting of an oblique illumination angle of $\tau = 8°$ and a tilt direction of $\Psi \in \{0°, 90°, 180°, 270°\}$ (the default values of the software to imitate the LAP setup), there is a slight variation of the sinusoidal 3D-PLI signal.

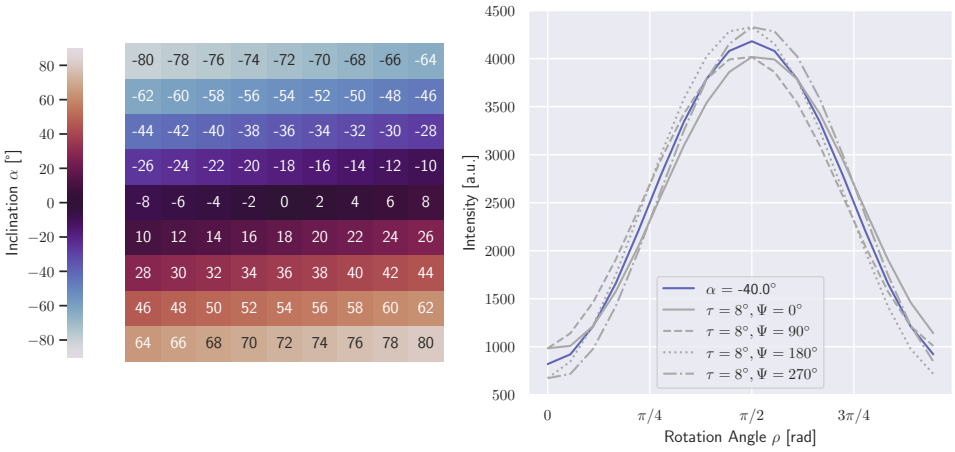

Figure 5.1: **Left**: Example data of a synthetic flat measurement with an increasing Inclination α from $\alpha = -80°$ to $\alpha = 80°$. **Right**: Selected 3D-PLI signal of the flat measurement with the corresponding oblique views.

For completeness, a `synPLI` call with $\alpha = 0°$, $t_{\text{rel}} = 1.0$ and $\varphi \in \{0°, 2°, \ldots 160°\}$ yields the content of fig. 5.2. Here, it can clearly be observed how a change in the Direction φ changes the phase of the signal of the flat measurement.

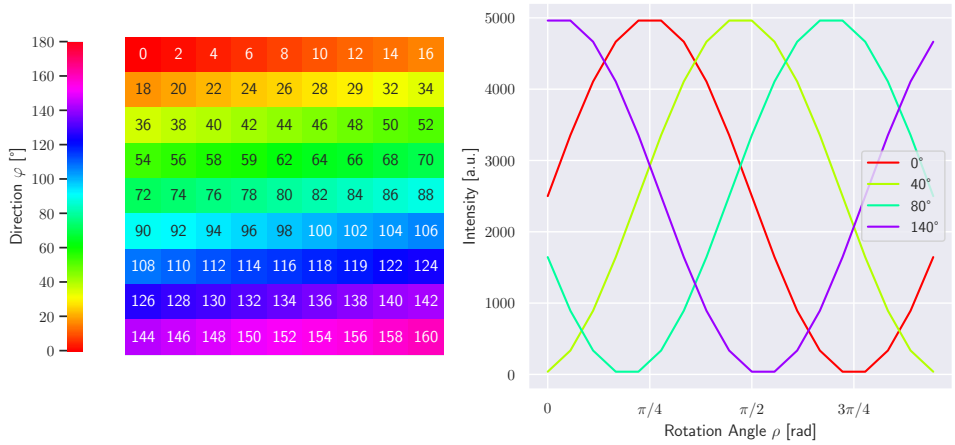

Figure 5.2: **Left**: Example data of a synthetic flat measurement with an increasing Direction φ from $\varphi = 0°$ to $\varphi = 160°$, with $N = 18$ rotation angles. **Right**: Selected 3D-PLI Signals for four different Directions φ.

In order to test algorithms now e.g., the least-squares fitting approach (ROFL) [71, 76] we can just hand these files to the algorithm via a few lines of bash as seen in listing 5.5.

Listing 5.5: Testing of the least squares fitting (ROFL) via synthetic measurements of flat and oblique views.

```
stack_0=Synpli_Calibrated_Flat.h5
dir_0=Synpli_Direction_Flat.h5
stacks_tilt=""

output="foo/"

for i in {1..4}
do
stacks_tilt+="Synpli_Calibrated_Tilted_${i}.h5␣"
done

rofl -id $dir_0 -if $stack_0 -it $stacks_tilt --output $foo
```

and compare the two output files. In the presented case the comparison is trivial because the ground truth from `synpliv2` and the output from `rofl` are identical.

Listing 5.6: Simple comparison between the ground truth Inclinations of `synpli` and the output Inclinations of `rofl`.

```
truth=$(h5dump synpli_output/Synpli_Inclination_Flat.h5 | head -n 16 | \
                tail -n 10 | awk -F':␣' '{printf␣"%s",␣$2}')

analysis=$(h5dump foo/*_Inclination.h5 | head -n 16 | \
                        tail -n 10 | awk -F':␣' '{printf␣"%s",␣$2}')

if
diff -q <(echo $truth) <(echo $analysis) >/dev/null;
then echo "true"; else echo "false";
fi

> true
```

Additionally, different tilt-amplitudes τ, tilt-directions Ψ, direction-offsets φ_{off} can construct a test matrix. The synthetic data is created with a chunk size of `(1,1,N)`, during development this simple case was enough to ensure that chunk-wise iterating (with and without `MPI`, `mpi4py`) works for other cases e.g., `(2048,2048,9)`.

5.2.4 Discussion

A framework for the generation of synthetic data with oblique views was developed. The synthetic data is in the same format (HDF5) as the workflow data of the real microscopic workflow, it also has the same attributes. The output consists of multiple files: The measurement arrays of the flat and the oblique views, and the *ground truth* arrays of the modalities.

After the synthetic data is generated it can be passed to the desired analysis program. The output of the analysis can then be compared with *ground truth* e.g., per command line. This approach fits especially into the interactive workflow on a headless system e.g., a supercomputing system like `JURECA DC` to get quick feedback if the software works with the temporarily loaded modules and Hardware (GPUs).

5.3 The Minimal Working Workflow

3D-PLI has been applied successfully to single sections and limited, contiguous, volumetric reconstructed brain sections [71]. The in-plane angle, the Direction φ, the out-of-plane angle, the Inclination angle α were validated using Two-photon fluorescence microscopy (TPFM) [80, 81, 56]. Furthermore, it helped to uncover unknown, iteratively repeated, column-like neuronal circuits in the avian forebrain [17]. However, if 3D-PLI should help to break down the entire human connectome at the microscale, ergo thousands of consecutive brain sections along the two hemispheres, these efforts need to be streamlined.

5.3.1 Introduction

A human brain sectioned into 50 µm thin section results in about 3 000 sections. If these sections are measured with oblique views using the LAP and the LMP-3D there are 2 × 3 000 datasets: the first 3 000 with macroscopic resolution (60 µm) and the seconds 3 000 with microscopic resolution (1.85 µm).

The 3D-PLI workflow starts with the calibration of the LAP or the LMP-3D raw data. The basis for an automatic workflow is the storing of the raw data in the self-describing HDF5 format with suitable attributes as introduced in section 5.1. The related calibration factors of the raw data can be found by a search for the calibration factors with the most recent `measurement_time` before the `measurement_time` of the raw data. Afterward, the Fourier analysis (section 4.1) can be applied without modifications.

As described in [71] a projective linear transform is then used to register the oblique measurements of the LAP onto the flat measurements, before performing the Least Squares Fitting (outlined in section 4.1.3). Finally, the resulting Direction and Inclination can be merged into the Fiber Orientation Map. These last three programs are not yet workflow-ready, they neither utilize the self-describing HDF5 files nor do they have been ported to the `Jureca DC`. The workflow is sketched out in fig. 5.3.

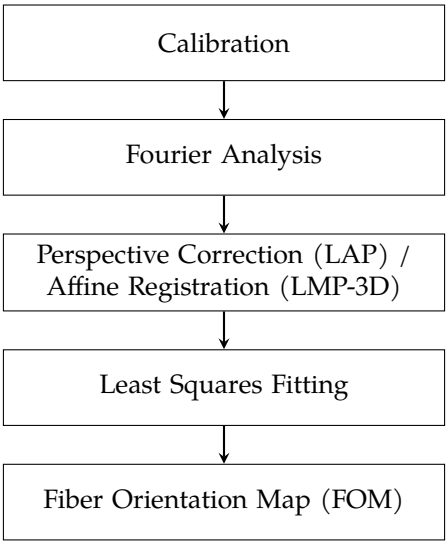

Figure 5.3: Basic workflow of the analysis of LAP and LMP-3D data after acquisition.

5.3.2 Development

The oblique views produce a slight perspective distortion in the case of the LAP, so the tilt measurements have to be registered to the flat measurement via a projective linear transformation [71]. The algorithm for the correction was implemented in Python via the free `ORB` algorithm of the `OpenCV` library [82], followed by a RANSAC [83] based homographic feature-mapping (from the same library) to find the homographic projection between the Transmittance image of the flat measurement and the Transmittance image of the tilted measurement. The Transmittance images undergo prior histogram equilization [84] to enhance the contrast.

The resulting matchpoints can be seen in fig. 5.4. The estimated homography is then applied to every rotation angle measurement of the oblique calibrated measurement with nearest-neighbor interpolation.[2] In the case of the LMP-3D, the perspective shifts are more subtle and are combined with sub-micrometer shifts, because of mechanical uncertainties of the microscope. This was solved via an affine registration.

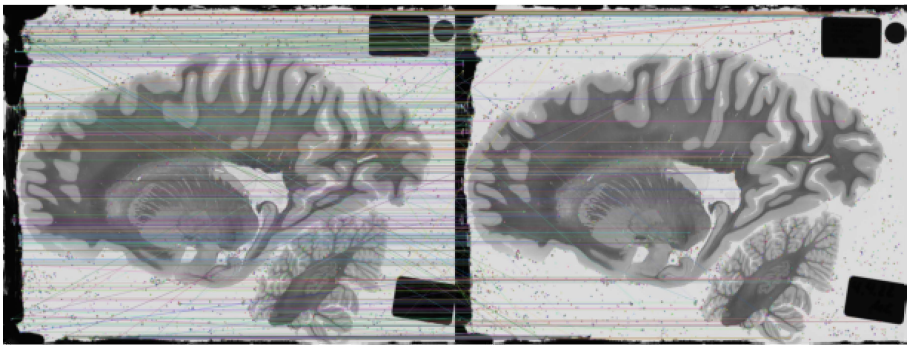

Figure 5.4: Matching key points of the ORB algorithm between one of the four tilted measurements (**left**) and the flat measurement (**right**) of section 920 of the Amsterdam Brain (see appendix A.1).

After the perspective correction, the pixel-wise Least Squares Analysis by [71] can be applied. The program was improved by automatically sorting the input with respect to the `tilt_angle_azimuth` attribute to ensure the correct order of the calibrated stacks of the tilt measurements in every run. Finally, the calculation of the FOM was implemented.

5.3.3 Results

In the final three stages of fig. 5.3, namely the perspective correction (LAP), Least Squares Fitting, and Fiber Orientation Map, have been addressed. A novel implementation of the perspective correction, involving histogram equalization, ORB keypoint detection, and RANSAC-based homographic-projection estimation, is employed to register tilt measurements to the flat measurement. For the LMP-3D, a homographic projection is not necessary, and an affine registration of tilt measurements to the flat measurement is applied. Afterward, the Least Squares Analysis is executed to derive Direction, Inclination, and relative Thickness. The final step involves the creation of the Fiber Orientation Map from the Direction and the Inclination modality. All five steps work automatically on the HPC system and make use of the self-describing HDF5 format.

[2] This is analog to the previous version which used the `SURF` algorithm (see [85]), but this algorithm is still patented. In production, a free version should be used.

5.3.4 Discussion

The necessary adjustments for the automatic processing of LAP and LMP-3D from the calibrated data to the Fiber Orientation Map were made. While the different processing steps for PLI have been described by [71, 14, 13], this is the first time the workflow has been implemented on HPC resources and works for both imaging systems, LAP and LMP-3D.

5.4 Workflow Update 1: Parallelizing the Directional Analysis

The Robust Orientation Fitting via Least Squares (ROFL) has been implemented in `numba` and has been parallelized via `mpi4py`. However, the GPU implementation of ROFL, goROFL[3] was just developed for a single GPU and was, for the previous studies, only executed on a consumer hardware GPU (NVIDIA GTX 1080) missing utilizing the (then) two server GPUs (2 Tesla K80 GPU) in each of the 75 GPU nodes of JURECA in production. Since the JURECA DC[4] has 48 accelerated compute notes with four AI accelerators (4× NVIDIA A100 GPU, 4× 40 GB HBM2e) each (see appendix D), there is room for optimization.

5.4.1 Introduction

The use of the multiple NVIDIA A100 GPU on JURECA DC can decrease the runtime, because of the faster bandwidth of the supercomputing system and because of the *pleasingly parallel* fitting problem which can be simply partitioned to the available accelerators. The new data-parallel multi-gpu program yields the updated workflow shown in fig. 5.5.

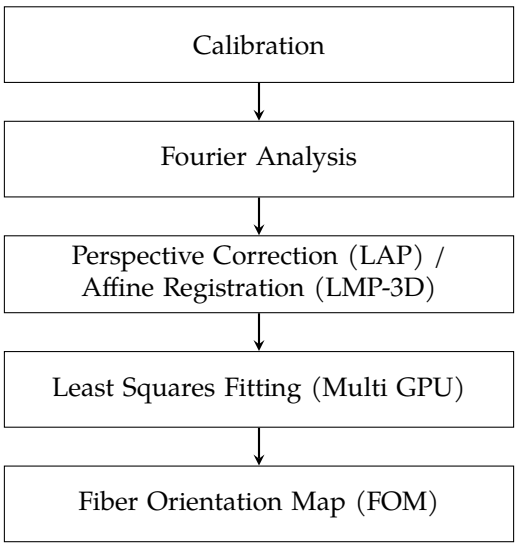

Figure 5.5: Updated version of the basic workflow: The Least Squares Fitting is now performed on multiple GPUs if available.

[3]The abbreviation goROFL stands for GPU-optimized ROFL.
[4]The Data-Centric (DC) update was performed in fall 2020.

5.4.2 Methods

The LMP-3D measurements can contain a large number of tiles as described in section 3.3. The saved measurements have an additional attribute `measured_tiles` which is a 2D array attributing to every of the 2048 × 2048 tiles a boolean **1** or **0** whether this tile was measured or not. This enables easy filtering and lowers the computational effort significantly because non-measured, black tiles constitute about one-third of the total number of tiles. Assuming a brain section with a tiling scheme illustrated in fig. 5.6, every fourth tile, starting from the index positions 0, 1, 2, and 3, can be sent to one of the four GPUs of a computing node via CUDA-Aware MPI. At the beginning of each computation the process can check whether the assigned tile has a `True` or **1** entry in the `measured_tile` attribute array, and if not, continue with the next tile. Alternatively, instead of filtering during the runtime of the algorithm, the iterator can be filtered beforehand, resulting in a more equal load between the processes.

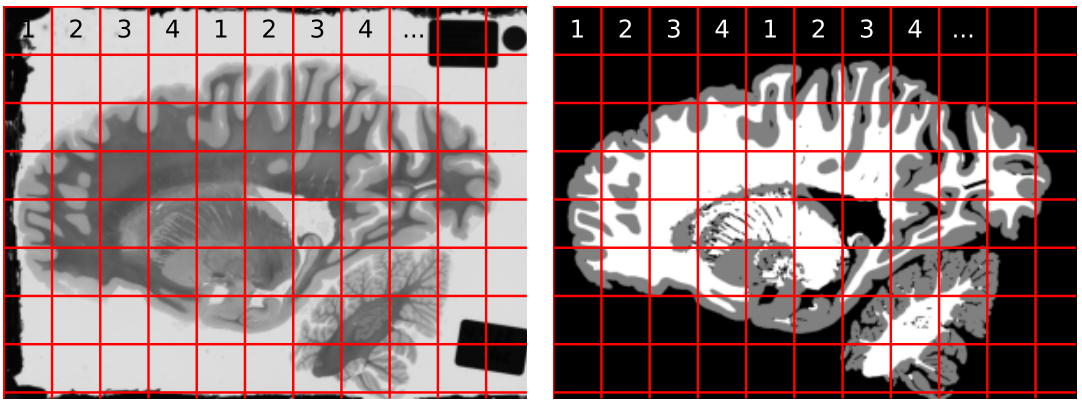

Figure 5.6: Schematic partitioning of the input data (**Left**: Transmittance, **Right**: Mask). The red lines denote the chunked layout of the data. Every 4th chunk is sent to the computing process p_1 to p_4. If a chunk of the mask is empty it can be skipped.

The same process can be applied to LAP measurements. LAP measurements have no `measured_tile` attribute, but by using a custom iterator (consisting of arbitrarily sized tiles e.g., iterating row-wise), every GPU can get its own chunk. For LAP and LMP-3D the computational load can be further reduced by providing a mask (manually or automatically created). Then, after loading the assigned measurement chunk, the data can be masked with the corresponding mask chunk. To utilize these circumstances accordingly the algorithm was refactored to use the in-house HDF5 attribute tooling which provides a (filtered) `Iterator` which can be sliced accordingly by the present MPI process as illustrated in listing 5.7.

Listing 5.7: Distributing the algorithmic workload by slicing the data iterator beginning with the present MPI-rank and with a stepsize of the present MPI universe size.

```
from mpi4py import MPI

comm = MPI.COMM_WORLD
rank = comm.Get_rank()
size = comm.Get_size()

for i in list(Iterator)[rank::size]:
        ...
```

5.4.3 Results

The Least Squares Fitting was performed on a LAP measurement with a size of 4164 × 3120 pixel, containing one and four oblique views. Additionally, a mask was provided. The program was run on an internal system with a NVIDIA RTX 3090, on the NVIDIA RTX Quadro 8000 on the Login/Development nodes of JURECA DC, and on 1, 2, and 4 NVIDIA A100 accelerators of the JURECA DC computing nodes. The results are visualized in fig. 5.7. The runtime on the RTX 3090 is with 148 s about three times larger than the runtime on the Quadro 8000 with 54 s. The runtime reduces to less than a half on one A100 accelerator. To run the program on two and four accelerators, the data was partitioned into two and four rows respectively. It was observed that the runtime of the two and four MPI processes was equally long despite different numbers of fore- and background pixels. More accelerators lead to a nearly linear speedup: two A100 reduce the runtime to 13 s, and four 100 s reduce the runtime further to 7 s.

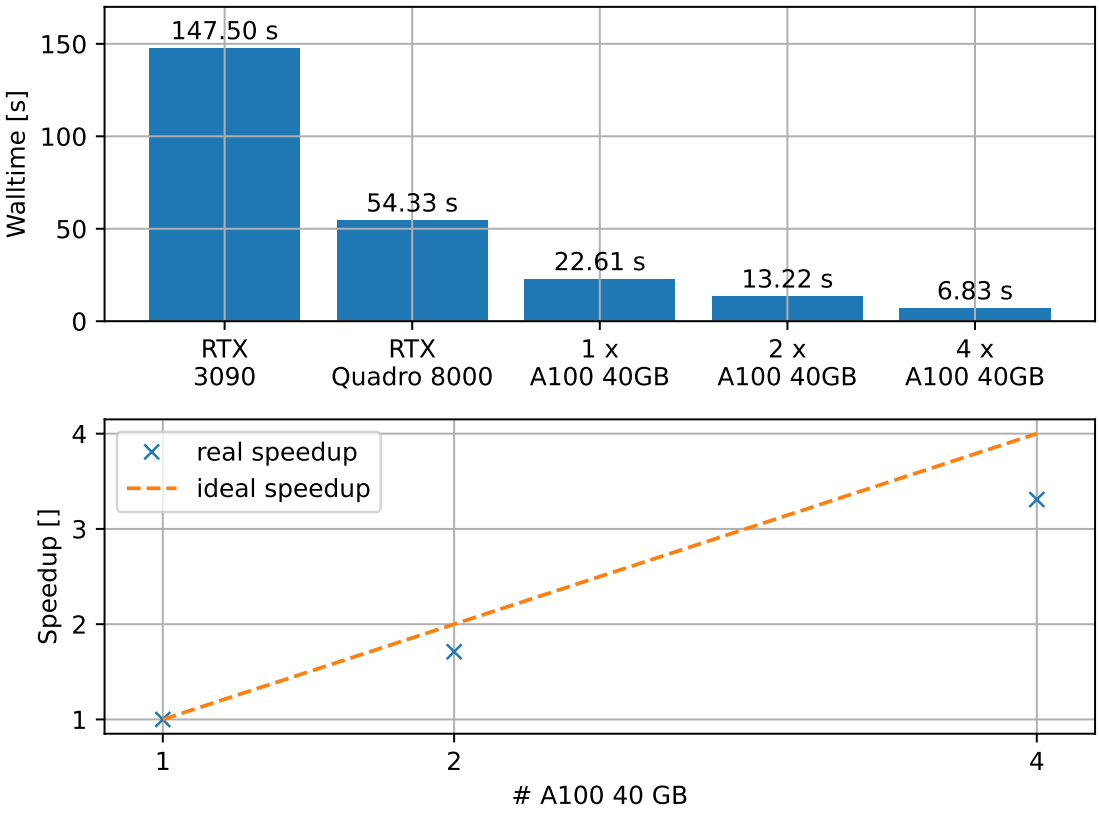

Figure 5.7: Runtime of the Least Squares Analysis via the `rofl` algorithm on different GPU configurations: The RTX 3090 is a consumer GPU, the RTX Quadro 8000 and the A100 40GB are datacenter GPUs. In the GPU nodes on `JURECA DC` four A100 40 GB are available.

This speedup transfers directly to the Least Squares Fitting on large LMP-3D sections (e.g., 38 × 52 tiles), so it is no longer the most time-consuming step in the workflow, as can be seen in fig. 5.8.

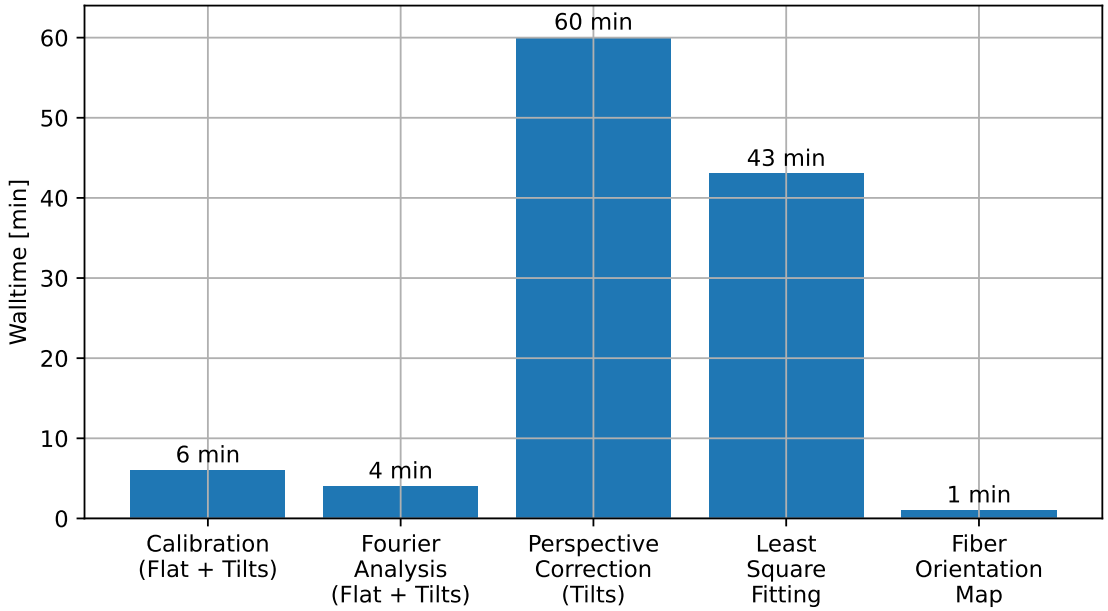

Figure 5.8: Walltimes of the PLI Workflow on a large LMP-3D brain section with 38 × 52 tiles.

5.4.4 Discussion

The Least Squares Fitting was successfully ported to multi-GPU via CUDA-Aware MPI which allows full utilization of the accelerator nodes of JURECA DC. This results in a significant speedup of the processing of LAP datasets, down to 7 s for 4164 × 3120 sized datasets. And brings the runtime of the analysis on large LMP-3D sections in a reasonable regime.

5.5 Workflow Update 2: Automatic noise and artifact removal with Independent Component Analysis

The up-to-here presented solution is enough for a quick basic analysis but fails if statistical methods should be applied to the data. In this case, the background would interfere with the analysis. Here, the application of Independent Component Analysis (ICA) on 3D-PLI data in combination with an automatic mask generation is presented. The successful application has been demonstrated on small rat and vervet brain sections for microscopic PLI measurements in [86].

This part focuses on the implementation of noise and artifact removal into the LAP workflow, because the artifacts are more prominent in the LAP than in the microscopic setup of the LMP-3D. The mask generation is performed after the Fourier analysis because it operates on the Transmittance and Retardation modality. Following this, the ICA is applied to the Calibrated data inside the generated mask. The updated flowchart can be seen in fig. 5.9.

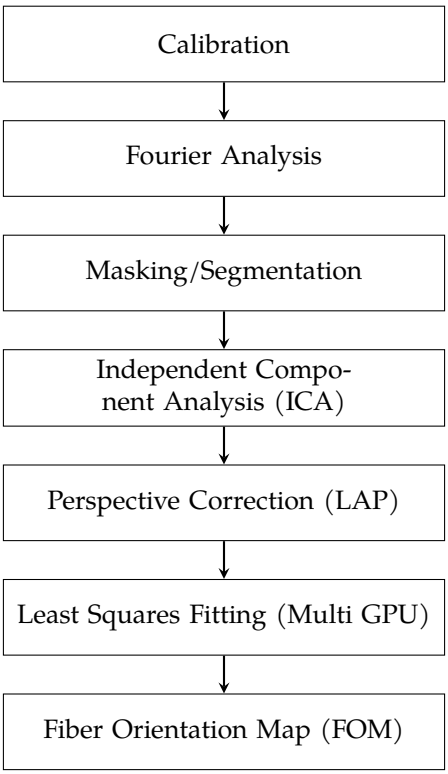

Figure 5.9: LAP workflow with automatic noise and artifact removal via mask generations followed by Independent Component Analysis.

5.5.1 Introduction

Independent component analysis (ICA) has been demonstrated to remove noise and artifacts of 3D-PLI data [87, 88, 89]. Furthermore, applications of ICA for Blind-Source-Seperation (BSS) and denoising are applied in electroencephalography (EEG), and Magnetoencephalography (MEG) [90]. The idea behind ICA is to find a mixing matrix A so that the measured signal X is obtained by multiplication of the mixing matrix A with the source signals S

$$X = A \cdot S, \tag{5.1}$$

with the assumption that the signal X is a linear combination of the source signals S and that the source signals are statistically independent. The unmixing $W \approx A^{-1}$ is found by the ICA algorithm by iteratively maximizing non-gaussianity in case of the FastICA algorithm [91] or maximizing negentropy in case of the extended infomax algorithm [92]. After convergence, the source signal S can be estimated as

$$W \cdot X = C \approx S, \tag{5.2}$$

with C being the components of the image. The distinction between A and W^{-1} and between S and C are made, because there is no way to estimate the *true* sources S due to the ambiguity

$$\begin{aligned} X &= W^{-1} \cdot \alpha \cdot \frac{1}{\alpha} \cdot C, \quad \alpha \neq 0 && (5.3)\\ &= \left(W^{-1} \cdot \alpha\right) \cdot \left(\frac{1}{\alpha} \cdot C\right) && (5.4)\\ &= \widetilde{W}^{-1} \cdot \widetilde{C}, && (5.5) \end{aligned}$$

where the components of $\widetilde{C}$ are as statistically independent as the components of C.

The noise components can then be identified through examination of the column vectors of W^{-1}. They are detected as non-sinusoidal components and can be zeroed out, yielding

$$W_d^{-1} = \begin{pmatrix} — & \text{Signal Activation 1} & — \\ — & \text{Signal Activation 2} & — \\ & \dots & \\ — & \text{Signal Activation } J & — \\ — & \cancel{\text{Noise Activation 1}} & — \\ — & \cancel{\text{Noise Activation 2}} & — \\ & \dots & \\ — & \cancel{\text{Noise Activation } K} & — \end{pmatrix}^T = \begin{pmatrix} — & \text{Signal Activation 1} & — \\ — & \text{Signal Activation 2} & — \\ & \dots & \\ — & \text{Signal Activation } J & — \\ — & 0 & — \\ — & 0 & — \\ & \dots & \\ — & 0 & — \end{pmatrix}^T, \tag{5.6}$$

where the subscript d marks it as the denoised mixing matrix [86]. The denoised signal X_d is then obtained by composition of W_d^{-1}, W, and X as

$$W_d^{-1} C = W_d^{-1} W X = X_d. \tag{5.7}$$

X_d is then a superposition of all the signal components combined with the respective signal activations.

5.5.2 Methods

The noise and artifact removal consists of three steps. First, the data is flattened and is split into Independent Components C via the `FastICA` [91] implementation of the `scikit-learn` library [93]. Second, by calculating the Fourier coefficients a_0, a_2, and b_2 of the activation function (the column vectors of the mixing matrix) the closest sinusoidal function is calculated. After calculating the mean squared error of the activation function and the fitting estimate, the noise activations were identified via thresholding. And as the last step the *denoising* matrix is calculated through $W_d^{-1} W$, before applying it to the signal X. The fourier-based fitting, the matrix operations, and the thresholding are implemented with `numpy` [79].

Before the denoising, in order to remove the background from the measurement scans, the `PLImig` [81] algorithm was first applied to the scans. But, because `PLImig` was developed for LMP-3D, where the measurement of the tiles is previously adapted to the area of the tissue, the software cannot handle surroundings like labels and the nail polish border for sealing the tissue between the microscope slide and coverslip. In section 5.5.2 this issue is shown for four selected LAP measurements.

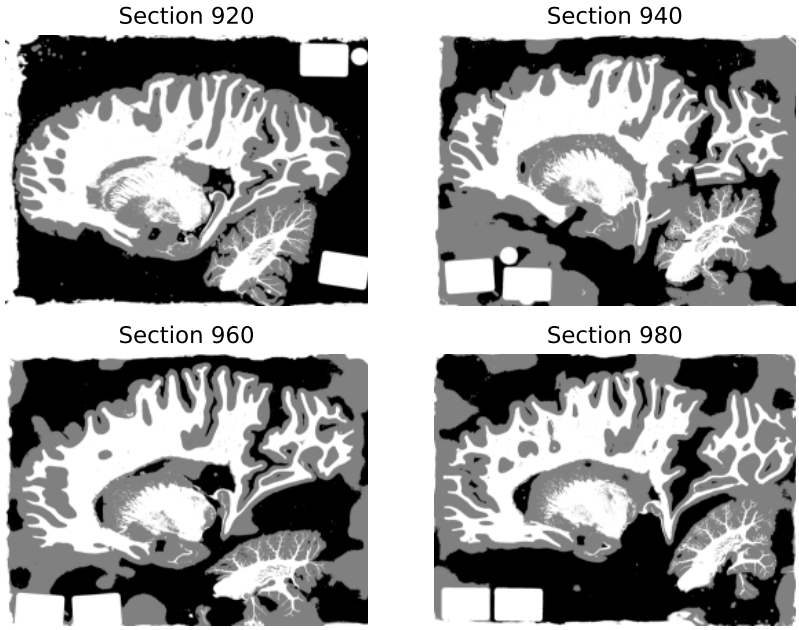

Figure 5.10: `PLImig` generated masks for LAP measurements of the Amsterdam Brain sections 920, 940, 960, and 980. The masking result from section 920 shows good separation of foreground and background, but a few misattributions like labels and the outer nail polish border are present. In the other masking the misattributions are more frequent and prominent.

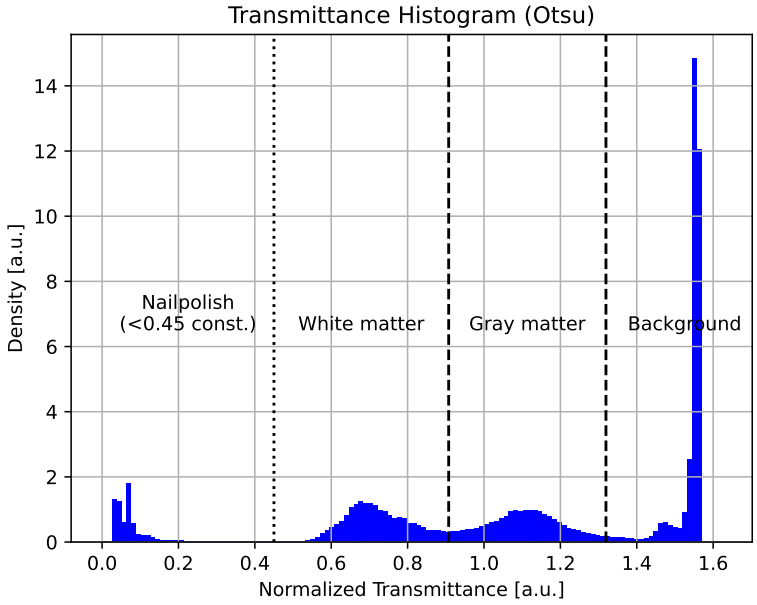

Figure 5.11: Histogram of the Transmittance modality of the Amsterdam Brain section 920 with nail polish threshold (dotted line) and annotated Otsu thresholds (dashed lines).

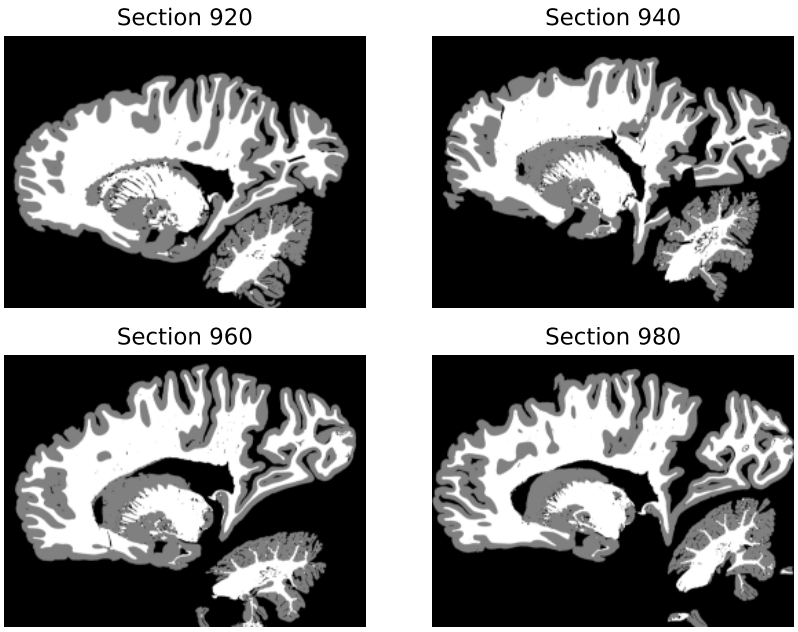

Figure 5.12: Masking estimates for the LAP measurements of the Amsterdam Brain sections 920, 940, 960, and 980 generated with the new, more robust approach.

The artifact denoising does not need perfect, but more robust segmentation. To continue with the workflow tooling without adjusting `PLImig` which is highly optimized for large sections, a simple program based on the Otsu's method solely for LAP was developed [94]. While `PLImig` is based on the analysis of Transmittance and Retardation to get better estimates regarding the segmentation of white and gray matter, this tool just takes the (normalized) Transmittance modality. The areas that are covered with nail polish or labels are intuitively dark because no light passes through. The signal of the background is high because the light passes through the glass without experiencing significant attenuation.

Because the nail polish is not always present (e.g., large sections where the field-of-view of the LAP solely consists of tissue) a nail polish threshold of < 0.45 was introduced and is defined as a constant in the program. The estimate for background, white-matter and gray-matter is then obtained by Otsu's method. The distinction between gray- and white matter is not important for the ICA for now and is included for completeness. The method is shown as a histogram in section 5.5.2. The results of this approach are shown in fig. 5.12, there, contrary to section 5.5.2 labels and nail polish are not present in the mask. In correspondance to `PLImig` the background is attributed the value 0, the estimate for the white matter is attributed the value 100, and the estimate for the gray matter is attributed the value 200. The mask to distinguish between background and tissue is then obtained by taking all pixels with a value greater than 0. The ICA input X is then obtained by applying this mask to the calibrated data. The resulting unmixing matrix W_d^{-1} is then applied to the flattened, non-masked calibration data in order to keep the full tissue environment for further processing, especially the following projective transform which is based on image-feature keypoint-matching.

5.5.3 Results

After the enhanced masking procedure, the Independent Component Analysis (ICA) separates the calibrated PLI signal into $N = 18$ components as the number of rotation angles ρ of the measurement. From this 18 measurement components C_1 to C_{18} the number of signal components is found to be three and the

number of noise components is found to be 15. In fig. 5.13 two of these three signal components and one of the 15 noise components are shown exemplarily. The signal components C_1 and C_2 show clear structure while component C_3 is dominated by noise. The corresponding activation functions W_1^{-1}, W_2^{-1}, W_3^{-1} have sinusoidal activation function in the case of signal (W_1^{-1}, W_2^{-1}) and a random or peak like function as for W_3^{-1}. After the discrimination of the sinusoidal and non-sinusoidal activation functions the denoising matrix W_d^{-1} is constructed from the sinusoidal activation functions and is multiplied by the components C. The resulting denoised signal is demonstrated on two points of white matter and two points of gray matter which have been marked in fig. 5.14. The corresponding signal profiles for the four points are shown in fig. 5.15. The profile of Point 1 of the white matter (WM) is not influenced by the denoising, the profile of Point 2 of the WM is cleared from one outlier. The signal profiles of the gray matter (GM), Point 1 (GM) and Point 2 (GM), have more variation and are greater influenced by the denoising and resemble more of a sinusoidal profile afterward.

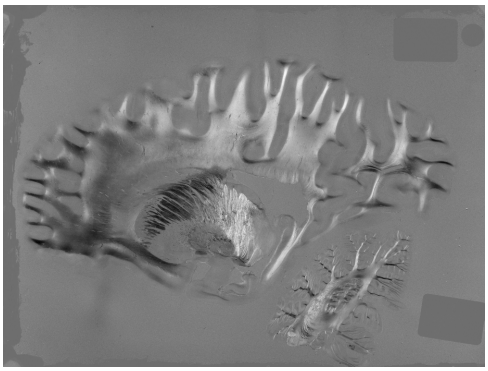

(a) C_1

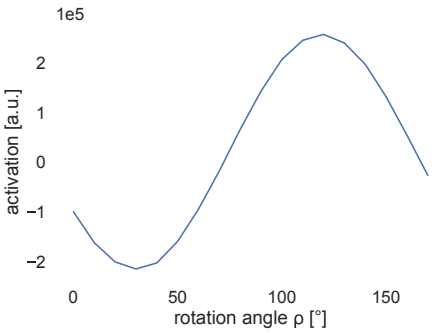

(b) W_1^{-1}

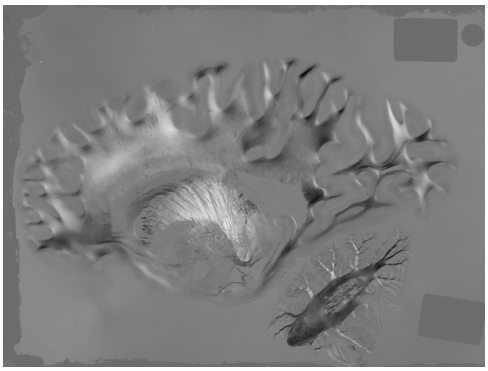

(c) C_2

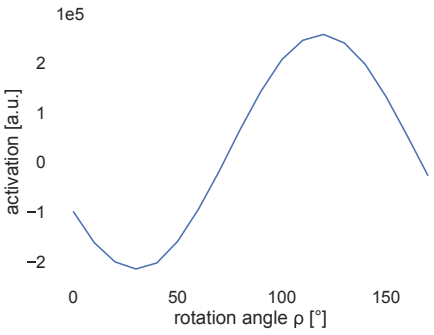

(d) W_2^{-1}

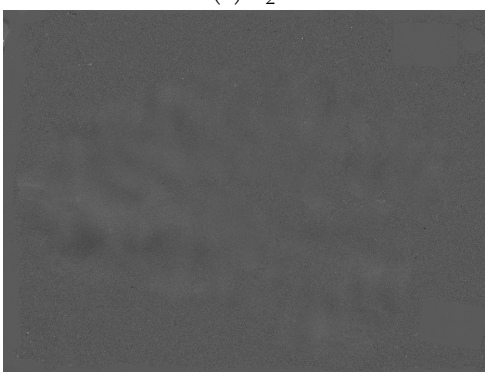

(e) C_3

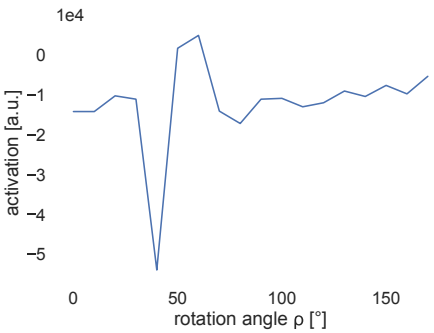

(f) W_3^{-1}

Figure 5.13: Results of the Independent Components Analysis of the LAP section. **Left**: Obtained Components with the background of the image, **Right**: Activation functions of the Components.

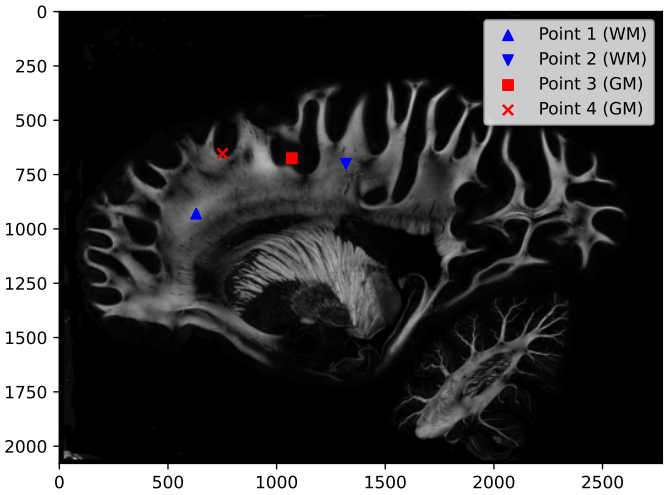

Figure 5.14: Retardation of section 920 of the Amsterdam Brain with four selected points to demonstrate the effect of the ICA denoising, two points in the white matter, and two points in the gray matter.

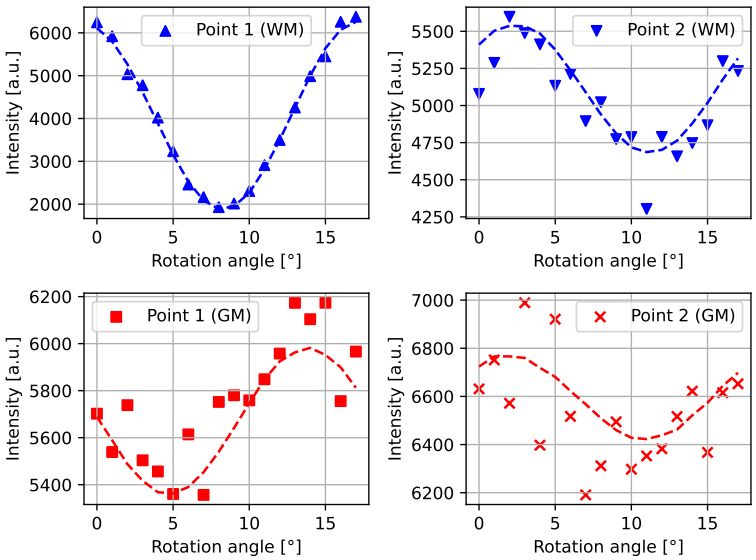

Figure 5.15: ICA denoising profiles of section 920 of the Amsterdam Brain in four selected points, two points in the white matter, and two points in the gray matter. The denoised signals are visualized by the dashed lines.

5.5.4 Discussion

The ICA-based denoising of PLI data was successfully integrated into the workflow. Because of the statistical nature of the ICA, it cannot be applied to the calibrated data directly, otherwise, the background (which can be quite large compared with the tissue depending on the section) would dominate the separation process. The new masking procedure based on Otsu's thresholding was found to be significantly more robust than `PLImig` because the latter was not designed to handle background features like nail polish and labels. However, `PLImig` is more sophisticated and makes case distinctions based on Transmittance and Retardation [81, 86]. So, a further objective should be to combine the two approaches. The impact of the denoising is visible for white matter and gray matter areas. For the white matter, it can provide a removal for outliers and for the gray matter, it additionally removes noise.

For the first time, it is now possible to perform LAP analysis from the calibrated data to the FOM with automatic ICA-based denoising. Previous studies focused only on the development and application of ICA [87, 88]. The prerequisite of a (robust) masking procedure was not mentioned until [86] and is now integrated into the workflow by multiplying the denoising matrix to the whole calibrated stack, allowing the perspective correction to function as before.

If the workflow should run without the denoising enabled it can be started with a `--skip-ica` flag. This can be helpful to further study the impact of the ICA on the result (FOM) and to process difficult sections where the automatic procedure might fail.

Part III

Estimating uncertainties

Chapter 6

Calculating uncertainties of fiber orientations

While the Least Squares approach from section 4.1.3 provides good and robust point estimates of the orientations it does neither provide a measure of uncertainty nor does it consider the underlying spherical distribution. This issue was first addressed by Schmitz et al. by utilizing Monte-Carlo Markow-Chain (MCMC) Sampling on a Bayesian formulation of the physical model of Polarized Light Imaging (PLI) with prior information. But this solution came with the high computational costs of $\geq 0.5s$ per pixel which is prohibitive for megapixel up to gigapixel data [85].

First, the Bayesian formulation of the 3D-PLI model is revisited. Second, in section 6.3, the computational shortcomings are addressed by porting the analysis to the Multi-threaded Optimization Toolbox (MOT)[1] which allows utilizing GPU resources via OpenCL [95]. This toolbox was developed for MCMC-Sampling of Diffusion MRI Microstructure Models [96]. Third, in section 6.4, a regression-based approach to estimate the uncertainties is presented.

Parts of this chapter have been previously published with shared first authorship in

- Schmitz D, Benning K, Schubert N, Minnerop M, Amunts K and Axer M (2022) Fast data-driven computation and intuitive visualization of fiber orientation uncertainty in 3D-polarized light imaging. Front. Phys. 10:958364. doi: 10.3389/fphy.2022.958364.

The first part uses the brain tissue and corresponding preparation of appendix A.1 (the Amsterdam Brain) and the second part uses the brain tissue and corresponding preparation of appendix A.2 (the Düsseldorf Brain).

[1] https://github.com/robbert-harms/MOT

6.1 Probabilities of Orientations in 3D-PLI

The Direction φ and the Inclination α describe a point on the surface of a half sphere, so while sampling the variable φ can be done linearly, sampling α is not straightforward, because the curvature from the pole to the equator as pictured in fig. 6.1. Here, we shortly derive the probability density functions for φ and α by using the surface area of the unit half sphere and marginalizing the joint distribution function [97].

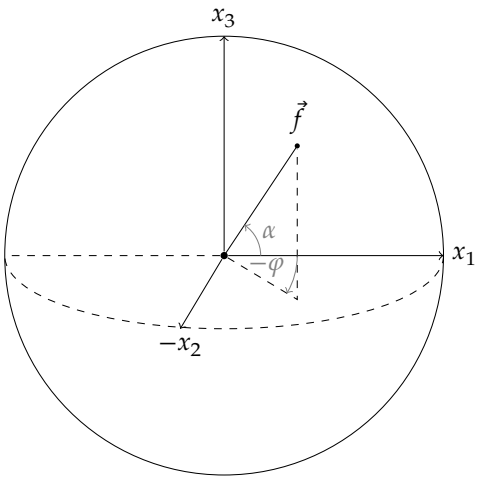

Figure 6.1: The Inclination angle α goes up from the plane to the pole at x_3 and the Direction angle φ goes counterclockwise from x_1. The angle φ and the axis x_2 are sign-reversed solely for the visualization.

The probability $f(\nu)$ to get a specifc fiber vector $\vec{f}$ is given by

$$f(\nu)\,\mathrm{d}A = \frac{1}{2\pi}\,\mathrm{d}A = g(\varphi,\alpha)\,\mathrm{d}\varphi\,\mathrm{d}\alpha\,, \tag{6.1}$$

where $\mathrm{d}A$ is the surface differential and 2π is the area of the unit half sphere. To obtain the joint probability density function $g(\varphi,\alpha)$, we have to introduce the jacobian determinant $\mathbf{J} = \cos\varphi$, so that

$$g(\varphi,\alpha) = \frac{1}{2\pi}\cos\alpha. \tag{6.2}$$

The probability density functions for α and φ are then found by marginalizing the joint distribution

$$h(\varphi) = \int_{-\frac{\pi}{2}}^{\frac{\pi}{2}} g(\varphi,\alpha)\,\mathrm{d}\alpha = \int_{-\frac{\pi}{2}}^{\frac{\pi}{2}} \frac{\cos\alpha}{2\pi}\,\mathrm{d}\alpha = \left[\frac{\sin\alpha}{2\pi}\right]_{-\frac{\pi}{2}}^{\frac{\pi}{2}} = \frac{1}{2\pi}\cdot(1-(-1)) = \frac{1}{\pi} = const., \tag{6.3}$$

$$j(\alpha) = \int_0^{\pi} g(\varphi,\alpha)\,\mathrm{d}\varphi = \int_0^{\pi} \frac{\cos\alpha}{2\pi}\,\mathrm{d}\varphi = \left[\varphi\frac{\cos\alpha}{2\pi}\right]_0^{\pi} = \frac{\cos\alpha}{2\pi}\pi - \frac{\cos\alpha}{2\pi}0 = \frac{\cos\alpha}{2}, \tag{6.4}$$

so as we can see, the probability of φ, along the equator, is constant, but the probability for α is dependent on α itself. This relationship was also empirically shown in [71] and translates to flat fibers occurring with a higher probability than steep fibers.

For the other parameters Transmittance T[2], relative Thickness t_{rel}, and Direction φ there is no non-trivial prior, but boundary conditions formulated as uniform sampling in the interval for

$$p(T) = \mathcal{U}(0, \infty), \tag{6.5}$$

and

$$p(t_{\text{rel}}) = \mathcal{U}(0, 1). \tag{6.6}$$

A more realistic model of PLI has to take these priors into account to estimate valid uncertainties on the orientation (Direction φ and Inclination α) and the relative Thickness of the fiber. The suitable method from probability theory is Bayes's theorem [98, 99]

$$P(A|B) = \frac{P(B|A)P(A)}{P(B)}, \text{with } P(B) \neq 0, \tag{6.7}$$

with the conditional probability of A if given B, the conditional probability of B is given A, and the probabilies of A and B. Assuming that the other probabilities are positive and greater than zero[3]: If the goal is to draw samples from the left-hand-side (the posterior probability), $P(B)$ can be left out since for two arbitrary samples we get

$$\frac{P(B|A_1)P(A_1)}{P(B)} > \frac{P(B|A_2)P(A_2)}{P(B)} \tag{6.8}$$

$$P(B|A_1)P(A_1) > P(B|A_2)P(A_2). \tag{6.9}$$

Furthermore, any multiplicative constant or normalization factor can be neglected, because only the shape of the distribution matters. After applying the logarithm, the product becomes a sum and all multiplicative constants become additive constants. So the log-posterior can be written as

$$\underbrace{\log P(A|B)}_{\text{posterior}} = \underbrace{\log P(B|A)}_{\text{log-likelihood}} + \underbrace{\log P(A)}_{\text{prior}} + \log(const.). \tag{6.10}$$

$$\tag{6.11}$$

In the literature this is referred to as writing the posterior *up to a constant* [99].

[2]Note that there is a Transmittance for the flat measurement and every tilt measurement.
[3]First Kolmogorov Axiom: The probability of an event is a non-negative real number.

Regarding PLI, the LHS can be identified with $\log P(\theta(T, \varphi, \alpha, t_{\text{rel}})|I)$, the probability for the PLI parameters θ given the intensities I. The RHS can be identified with the log-likelihood of the PLI model plus the prior information for the Inclination angle derived in eq. (6.4). For the priors we only get

$$\log P(\alpha) = \log(j(\alpha)) = \log \frac{\cos \alpha}{2} = \log(\cos \alpha) + const., \tag{6.12}$$

since the priors for T, φ, and t_{rel} are uniform. We derive the likelihood of the PLI model as

$$P(I|\theta(I_T, \varphi, \alpha, t_{\text{rel}})) = \prod_{\tau,\psi,\rho} \mathcal{N}(\hat{I}(I_T, \varphi, \alpha, t_{\text{rel}}; \tau, \psi, \rho), \sigma^2_{\tau,\psi,\rho}) \tag{6.13}$$

$$= \prod_{\tau,\psi,\rho} \frac{1}{\sqrt{2\pi}\sigma_{\tau,\psi,\rho}} \exp\left\{-\frac{(I_i - \hat{I}(I_T, \varphi, \alpha, t_{\text{rel}}; \tau, \psi, \rho))^2}{2\sigma^2_{\tau,\psi,\rho}}\right\}, \tag{6.14}$$

with the model variance $\sigma^2_{\tau,\psi,\rho} = g \cdot \hat{I}$ (see [85]). After taking the logarithm to obtain the log-likelihood we get

$$\log P(I|\theta(I_T, \varphi, \alpha, t_{\text{rel}}) = -\frac{1}{2} \sum_{\tau,\psi,\rho} \log\left(\sigma^2_{\tau,\psi,\rho}\right) + \frac{(I_i - \hat{I}(I_T, \varphi, \alpha, t_{\text{rel}}; \tau, \psi, \rho))^2}{\sigma^2_{\tau,\psi,\rho}} + \text{const.}. \tag{6.15}$$

Note that neglecting the noise model and assuming homoscedasticity, yields the least squares approach of section 4.1.3.

6.2 Monte-Carlo Markow-Chain (MCMC) for 3D-PLI

Markov-Chain Monte-Carlo for the uncertainty analysis of 3D-PLI was demonstrated and verified first in [85][4]. Schmitz et al. implemented the objective function and the priors with the `emcee` package [100]. This sampling library builds upon the Metropolis-Hastings algorithm in an ensemble [101].

The priors can be implemented as a function as seen in listing 6.1. The reparametrization was introduced in [60] to allow for an unbounded optimization, because of the symmetry of the fiber vector on a half sphere. An implementation is shown in listing 6.2. Before the application of the derived cosine prior, the Inclination α has to be projected into the interval $\alpha \in [-\pi/2, \pi/2)$, so that the log function obtains only positive values. The same function is, after the sampling, applied to the sampling results to reproject the Inclination samples as well as the Direction samples.

Listing 6.1: Python function of the MCMC analysis prior.

```
def _objective_function_prior(transmittances, alpha, t, phi):
    if (
    np.all(transmittances > 0) and 0 < t <= 1
    ):
        _, alpha = reparam_angles(phi, alpha)
        return np.log(np.cos(alpha))
    else:
        return -np.inf
```

[4]The implementation was dubbed **BA**yesian **M**ultivariate **B**irefringence **I**nference, short BAMBI.

Listing 6.2: Python function of the 3D-PLI reparametrization.

```
def project_alpha(phi, alpha):
    return ((alpha + np.pi / 2) % np.pi - np.pi / 2) * np.sign(
        -np.floor((phi / np.pi) % 2) + 0.5
    )

def project_phi(phi):
    return np.mod(phi, np.pi)

def reparam_angles(phi, alpha):
    alpha = project_alpha(phi, alpha)
    phi = project_phi(phi)
    return phi, alpha
```

The `emcee` sampler can be given several walkers with several defined sample steps. The walkers are members of an ensemble that explores the given parameter space. After a defined (and experimentally determined (see [85])) burn-in time in which the walker reaches equilibrium, samples are taken and stored in an array. The result can be visualized in a trace plot. Example traceplots of a fiber with Direction $\varphi = 45°$, rel. Transmittance $t_{\text{rel}} = 0.8$, and Inclination $\alpha = 20°$ after sampling are given in fig. 6.2. Here, the traces for Direction φ, relative Thickness, and Inclination α for 100 ensemble walkers with $5,000$ iterations are shown. For visualization purposes, only the first three walkers are displayed.

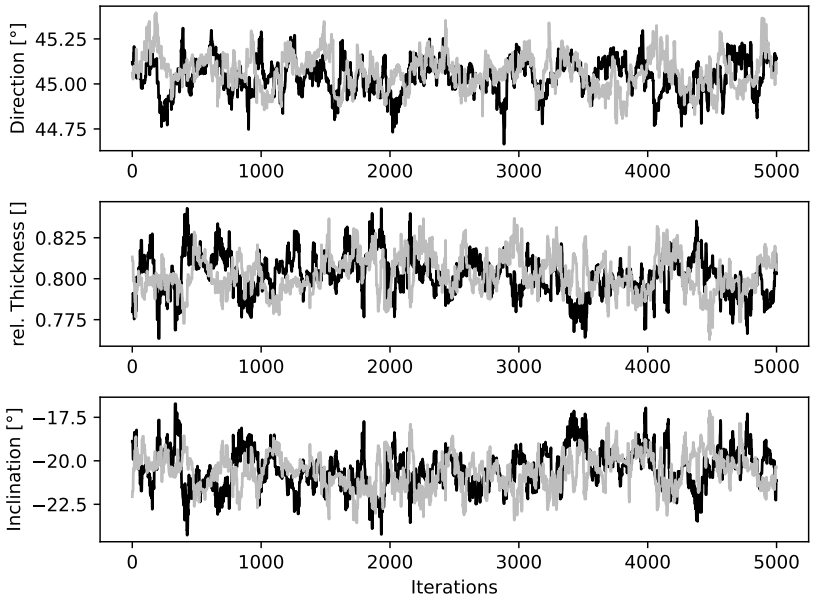

Figure 6.2: Traceplots of the MCMC sampling with the `emcee` implementation of the ensemble sampling strategy described in [101]: Of the 100 walkers, 3 walkers are isolated for $5,000$ iterations after burn-in, without thinning for Direction φ, rel. Thickness t_{rel}, and Inclination α.

Traceplots are useful to investigate whether the sampling explores the parameter space sufficiently and how well the mixing is. They are an essential part of MCMC sampling diagnostics [102]. However, trace plots do not show the projected distributions or the covariance between the variables. For this, the triangle or corner method can be used in which scatterplots between all traces are plotted and arranged

in a triangle [103]. In fig. 6.3 the traces of fig. 6.2 are shown.

From the scatter plot in the lower-right, it follows that the variables Inclination α and rel. Thickness t_{rel} are highly correlated. This results from the product of t_{rel} and $\cos^2 \alpha$ in the Retardation equation, which means manifold combinations of these two variables result in a specific Retardation. Furthermore, when looking at the projections, the spread of the Inclination samples is larger than the spread of the Direction samples, so the uncertainty on the Inclination estimate is larger. This result is intuitive since the Inclination α needs the additional work of incorporating the intensities of the oblique measurements into the analysis (see section 4.1.3) and cannot be straightforwardly computed by Fourier analysis like the Direction φ which is just a simple phase-shift (see section 4.1.2).

The projections of the variables are unimodal and align with the ground truth (the dashed line in the middle is close to the blue line representing the ground truth). Point estimates and credible intervals (CIs) via highest posterior density intervals (HPDi) are obtained using Principal Component Analysis (PCA) to calculate the principal orientation (constructed by Direction and Inclination). Post-PCA, the 95% HPDi for the orientation values is computed by projecting samples around the principal axis [85]. For the relative Thickness, the point estimate and the HPDi calculation is straightforward. Computation occurs in batches over `x` due to the potentially large array `(x, y, n, m)` in both the GPU and CPU implementations of section 6.2.

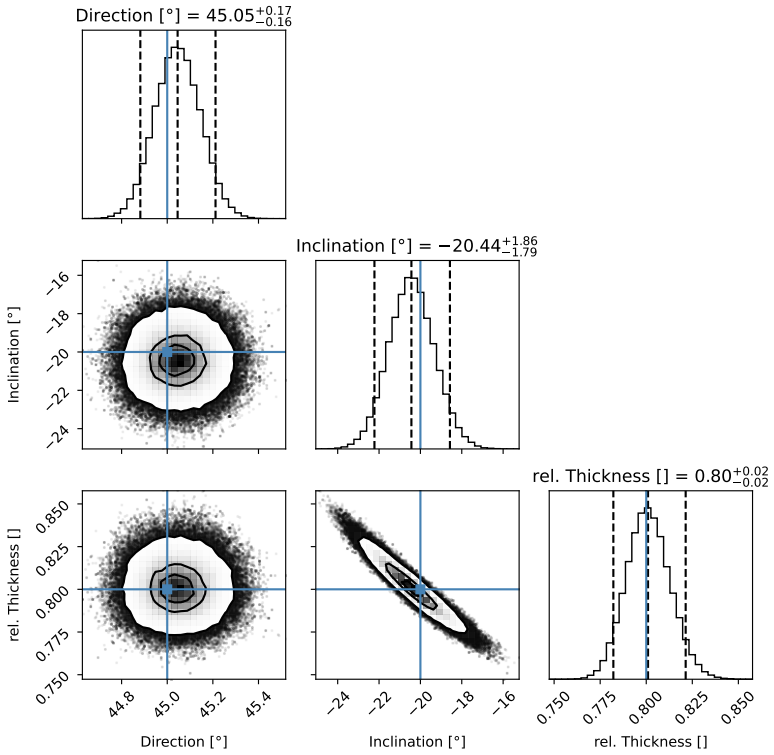

Figure 6.3: Corner plot via the `corner` package [103] of 5,000 iterations with 100 walkers after burn-in without thinning of Direction, rel. Thickness, and Inclination: Here, it can be seen that the Direction is not correlated with the Inclination or rel. Thickness, but rel. Thickness and Inclination are strongly correlated. The dashed lines on the left and right mark the 95% HPD interval. The blue lines represent the ground-truth values.

6.3 Accelerating the uncertainty analysis with GPUs

Schmitz et al. proposed that the resulting computational effort of the MCMC sampling for the sheer amount of data points in megapixel to gigapixel images could be counter-acted by the usage of GPUs. Since the Least Squares analysis `ROFL` [71] was also accelerated via GPU usage via the `Gpufit` library [77, 76], this seems like an obvious step. Here, the Multi-threaded Optimization Toolbox (MOT), a computational package of the Microstructure Diffusion Toolbox (MDT) which is used for the analysis of diffusion Magnetic Resonance Imaging (dMRI) [96] is applied to the uncertainty estimation computation.

6.3.1 Introduction

The Multi-threaded Optimization Toolbox (MOT) is a Python library offering voxel-wised parallelized MCMC sampling realized via the OpenCL framework [95]. `MOT` which uses `PyOpenCL` library [104] needs the objective function and the priors in `OpenCL` code. While the mathematics and the underlying concepts stay the same such a rewrite can be quite technical and requires some caution that the behavior of the software does not change [105].

6.3.2 Methods

For an easier translation of the 3D-PLI objective function to `OpenCL` the uncertainty analysis was first rewritten with the scalar expression for the 3D-PLI intensities derived in chapter 4. Since this expression does not require array or matrix algebra only scalar expressions can be used. We denote the new implementation as the reference implementation, the implementation by Schmitz et al. [85] as the original implementation. After comparison of these two implementations and ensuring their similarity the code was translated to `OpenCL`.

For the `MOT` library the `OpenCL` code has to be embedded in Python docstrings. An example embedding of the calculation of the Direction φ is shown in listing 6.4. To prevent double inclusions from the objective function, the function is enclosed by preprocessor directives. The same has to be done for the implementation of the Retardation function, for the 3D-PLI formula. The final posterior function is then piecewise assembled by combining the different `OpenCL` embeddings via string concatenation. The Inclination prior calculation for the `MOT` implementation can be simplified as

$$\log P(\alpha) = \log(|\cos\alpha|) \tag{6.16}$$

$$= \log\left(\sqrt{\cos^2(\alpha)}\right) \tag{6.17}$$

since there is no difference w.l.o.g. for $P(45°) = P(45° + 180° \cdot n)$, for $n \in \mathbb{N}$ regarding the probabilities. The respective `OpenCL` embedding is shown in listing 6.3.

The embeddings can then be read-in by the `MOT` module via the `SimpleCLFunction.from_string` method. These functions can then (together with the point-estimates from the Least Squares Analysis) be provided to an instance of the `AdaptiveMetropolisWithinGibbs` sampler which is used for sampling [106].

Listing 6.3: `OpenCL` code for the Inclination prior calculation

```
prior = """
double my_model_prior(local const mot_float_type* const x,
            void* data){

mot_float_type phi, alpha, trel;
phi = x[0];
alpha = x[1];
trel = x[2];
if ((trel <= 0) || (trel > 1) || (x[3] < 0)){
    return log(0.0);
}
return log(sqrt(cos(alpha) * cos(alpha)));
}
"""
```

Listing 6.4: Direction φ calculation for different tilting angles τ (`TAU`) and tilting directions ψ (`psi`) implemented as an OpenCL function inside a Python docstring.

```
get_phi_single_expression_function_code = """
#ifndef INCLUDE_GUARD_get_phi_single_expression
#define INCLUDE_GUARD_get_phi_single_expression
float get_phi_single_expression(float phi, float alpha, float TAU, float
   psi) {
        float second_arg = (
                cos(psi) * sin(alpha) * sin(TAU) -
                2 * cos(alpha) * cos(psi) * pow(sin(TAU / 2), 2) * sin(phi)
                    * sin(psi) +
                cos(alpha) * cos(phi) * (cos(TAU) * pow(cos(psi), 2) + pow(
                   sin(psi), 2))
        );

        float first_arg = (
                sin(alpha) * sin(TAU) * sin(psi) +
                cos(alpha) * (cos(psi) * sin(phi - psi) + cos(TAU) * cos(
                   phi - psi) * sin(psi))
        );

        return atan2(first_arg, second_arg);
}
        #endif // INCLUDE_GUARD_get_phi_single_expression
"""
```

The sampling result is stored as a `numpy` array on the `/scratch` partition for the following MCMC diagnostics. The saved array has the shape `(x,y,n,m)`, with `n` being the number of samples and `m` being the number of modalities. The sampling is for the `emcee`-based CPU implementation performed with

100 chains, 100 burn-in samples, and 500 stored samples [85]. The `MOT`-based GPU implementation is run with 500 burn-in samples and with 1,500 stored samples.

6.3.3 Results

The modalities Direction, Inclination, and relative Thickness as well as the credible intervals of Direction, Inclination, and relative Thickness of the original implementation of [85] is in accordance with the presented reference implementation. The CI maps of both implementations and the histogram comparison are shown in fig. 6.4. In the comparison of the Inclination CI values the main peak is a bit lower and a hump is appearing at $> 50°$.

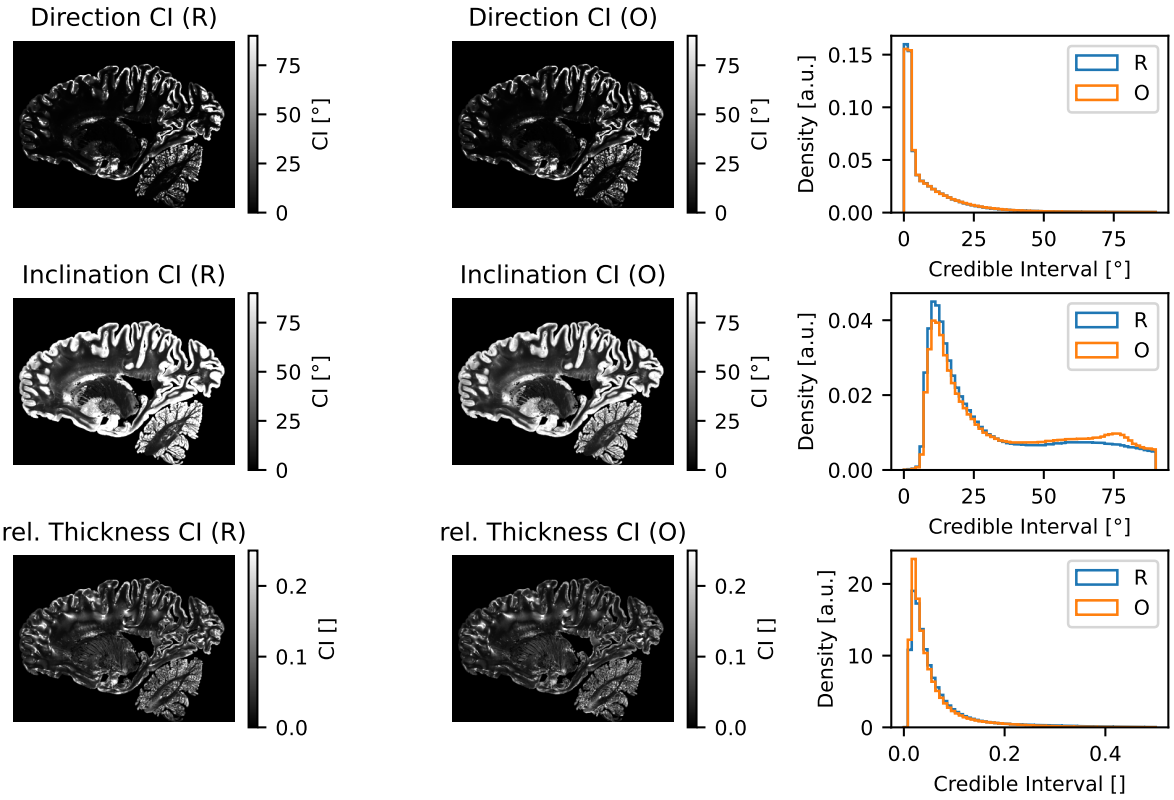

Figure 6.4: Comparison of the credible intervals (CI) of the original CPU implementation (O) and the developed reference CPU implementation (R).

The trace plots for Direction, Inclination, and relative Thickness for the GPU and CPU implementation are given in fig. 6.5. The GPU traces are in blue and the CPU traces are shown in red. Every sampling procedure is converged and stable around Direction $\varphi = 45°, \alpha = -20°$, and relative Thickness $t_{\text{rel}} = 0.8$. Both samplers explore the parameter space, but the variance of the CPU implementation is greater than that of the GPU implementation.

The corner plot of the GPU traces is shown in fig. 6.6. Compared with the corner plot of the CPU traces (see fig. 6.3), the distributions are unimodal and are also centered around the ground truth values (blue lines), but they are nosier and the borders of the percentiles are not as pronounced.

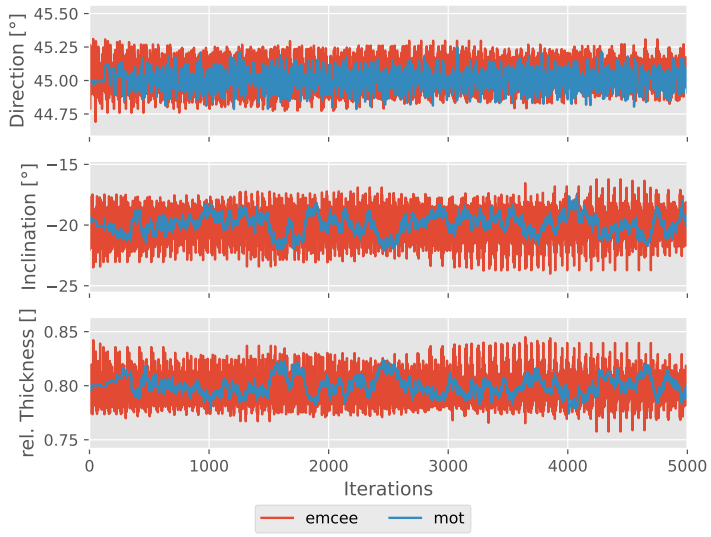

Figure 6.5: Traceplots comparison of the MCMC sampling with the `MOT` implementation of the Adaptive Metropolis-Within-Gibbs (AMWG) Strategy [106] with the `emcee` implementation of the Ensemble Sampler [101] (combination of 100 walkers). Here, 5,000 iterations after burn-in, without thinning for Direction φ, rel. Thickness t_{rel}, and Inclination α are shown.

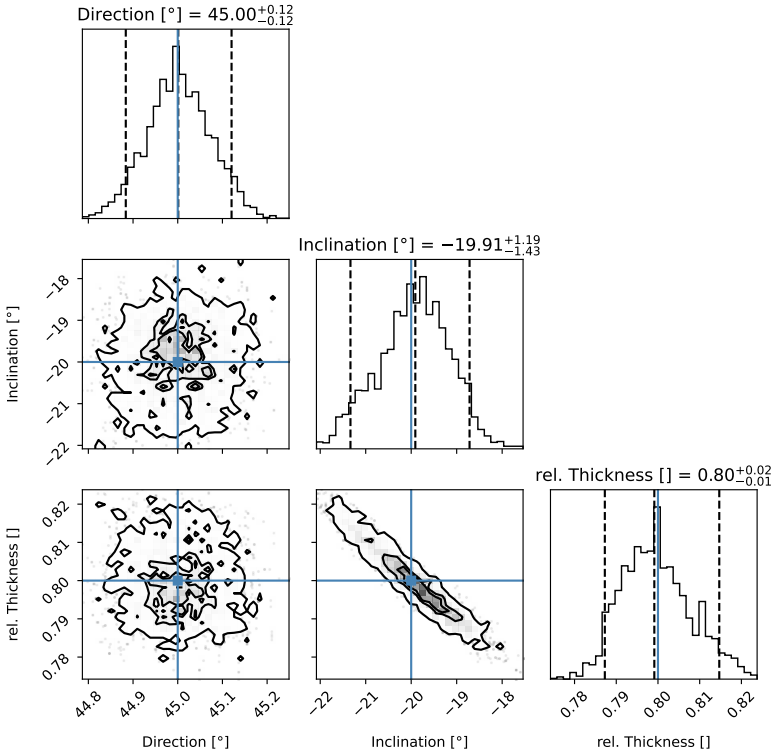

Figure 6.6: Corner plot of the `MOT` sampling [96] of 5,000 iterations after burn-in without thinning of Direction, rel. Thickness, and Inclination: Here, it can be seen that the Direction is not correlated with the Inclination or rel. Thickness, but rel. Thickness and Inclination are strongly correlated. The dashed lines left and right mark the 95% HPD interval. The blue lines represent the ground-truth values.

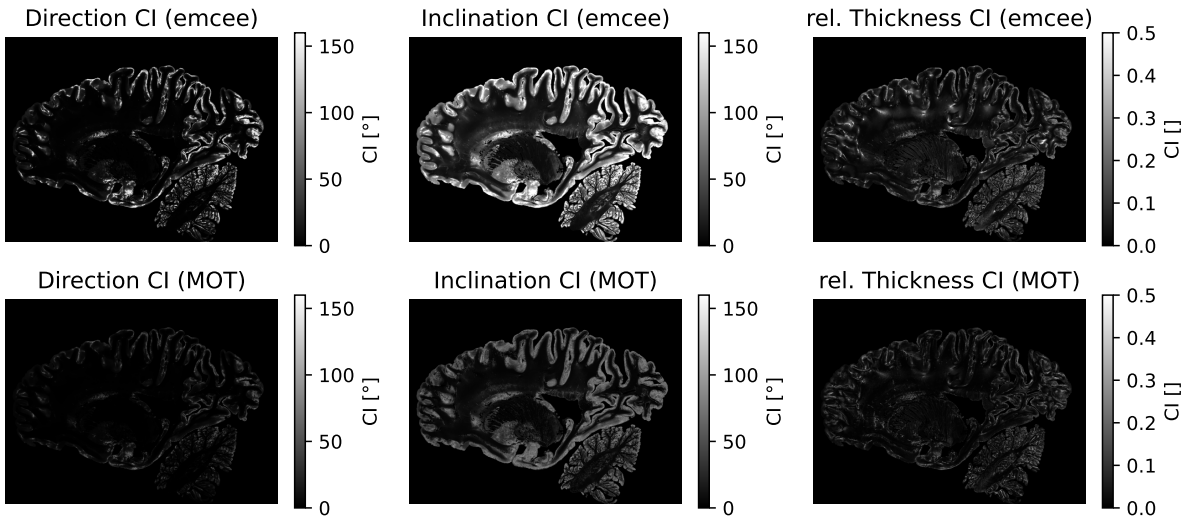

Figure 6.7: Comparison of the credible-interval maps of Direction, Inclination, and relative Thickness (T_{rel}) of the emcee and the `MOT` implementation.

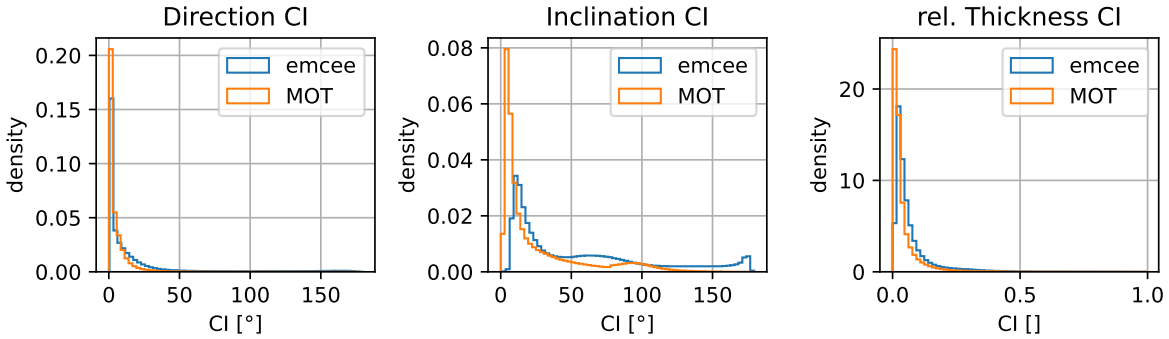

Figure 6.8: Comparison of the credible-interval histograms of Direction, Inclination, and relative Thickness T_{rel} of the emcee and the `MOT` implementation.

The runtime for the selected number of chains and number of samples in the two `emcee` implementations are $>$ 340 minutes per section when using 128 cores. In the original implementation, the diagnostic of the samples is combined with the sampling, contrary to the presented reference implementation and the corresponding GPU implementation (in order to have reusable code). The runtime for the diagnostics is about 30 minutes for both implementations[5]. The sampling runtime of the CPU reference implementation is about 310 minutes and the sampling runtime for the GPU implementation is 44 minutes when 4 GPUs are used. The speedup of using 2, and 4 GPUs behaves linearly and is shown in fig. 6.9b This results in a speedup of ≈ 7. The speedup with the diagnostic runtime included is ≈ 4.5.

The (unparallelized) runtime per pixel (here, the mask contains 2,642,985 in total) is for the original implementation (diagnostics included) $1.1^{\text{sec.}}/_{\text{pixel}}$. The reference implementation (diagnostics excluded) takes $0.9^{\text{sec.}}/_{\text{pixel}}$. The GPU implementation (diagnostics excluded) takes $0.004^{\text{sec.}}/_{\text{pixel}}$.

[5]Note that because of the shape of the sampling results `(x,y,n,m)` the diagnostics may require longer runtime, because of smaller sample sizes during iteration. The performance of the diagnostics is mainly memory bound.

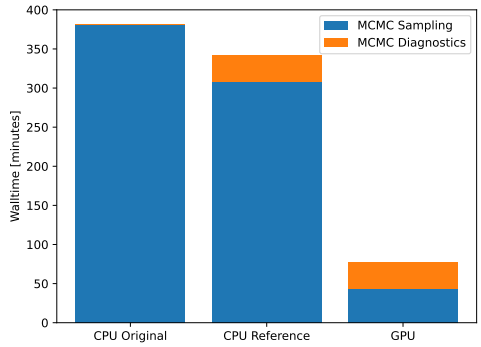

(a) Walltimes of the three different MCMC-based Directional Analysis implementations. The walltime for the CPU implementation is measured for 128 cores, and the walltime for the GPU implementation is measured for 4 GPUs.

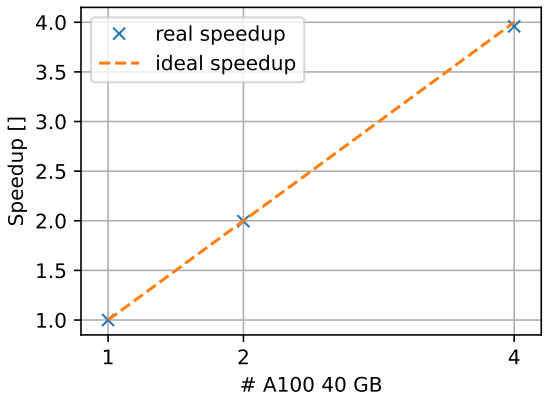

(b) Speedup of the MOT-based MCMC Directional Analysis for 1, 2, and 4 A100 GPUs.

Figure 6.9: Comparison of MCMC walltimes and speedup.

6.3.4 Discussion

A GPU acceleration of the MCMC-based uncertainty analysis was presented. As it is not based on an ensemble approach the trace plots show that the parameter space is not entirely explored (it underestimates the errors) and the resulting distributions are noisier, the results still resemble very much the results from the CPU-based implementation via `emcee` and significant speed-up is archived which might make up for the loss in precision.

However, bringing `OpenCL` to the scene and working with a C-based language inside the Python code-base can introduce errors and calls for care. Intermediate rewrites and continuous comparison of the results of different implementations are needed. Here, the synthetic data generation presented in chapter 5 can work as a reference during implementation and further adjustments.

6.4 Learning and visualizing uncertainties

Even after implementing the algorithms on GPUs the runtime of the uncertainty analysis is still significant. Additionally, the resulting credible interval (CI) modality maps are noisy. This is counter-intuitive since it seems unlikely that pixels in a direct neighborhood have very different CI values.

As machine learning (and artificial intelligence) have shown impressive results for large datasets without the need for analytical models, the question arises if this thinking can be applied to the calculations of fiber orientation uncertainties. However, these models have (with only a few counter-examples) the downside that they are behaving like *black boxes* which limits their trustworthiness [107, 108]. In this chapter, an interpretable and physically inspired machine-learning model based on Generative Additive Models (GAM) [109] is presented.

6.4.1 Introduction

If the credible intervals for Direction (σ_φ), Inclination (σ_α), and relative Thickness (σ_t) are plotted against Retardation ($\sin\delta$), relative Thickness, and the absolute Inclination ($|\alpha|$) correlations between

these pairs are observed [110]. We can identify these correlation pairs as a tuple of Target (Y) and Predictor (X) variables. Furthermore, these correlations show a monoton and convex behaviour which can be used as constraints. These pairs are listed in table 6.1.

Table 6.1: Correlation pairs of the uncertainty estimates: credible intervals vs. modality maps with their respective constraints. Taken from [110].

Target (Y)	Predictor (X)	Constraints
In-plane angle CI σ_φ	Retardation $\sin\delta$	mon. dec. and convex
Out-of-plane angle CI σ_α	rel. Thickness t_{rel}	mon. dec. and convex
Rel. Thickness CI σ_t	Out-of-plane angle $\lvert\alpha\rvert$	mon. inc. and convex

6.4.2 Methods

General Additive Models [109] offer a bridge between linear regression problems and arbitrary function modeling. They can be easily motivated by considering the liner regression formula

$$E(y|X) = \alpha + \beta X, \tag{6.18}$$

with β being a vector of coefficients, and X being a matrix of descriptor row-vectors. The matrix elements can be substituted by discretized second-order (pre-computed) spline functions. This leads to the flexible function

$$f(x) = \sum_{j=0}^{q} B_{ij}\beta_j = \mathbf{Bb}, \tag{6.19}$$

with B_{ij} being $j \in \{0, 1, \dots q\}$ splines functions represented as $q \in \mathbb{N}$ column vectors with the respective row index i being the precomputed spline value $f(x_i)$ at x_i.

Since the height of these splines is then proportional to the β_i, the constraints (or our prior knowledge) listed in table 6.1 can be appended to the regression model as penalties on the first-order and second-order differences of the coefficients [111]

$$\alpha, \beta = \underset{\alpha,\beta}{\operatorname{argmin}} \|y - (\alpha + \mathbf{Bb})\|_2^2 + \lambda \sum_{j=3}^{q} \left(\Delta^2 \beta_j\right)^2 \tag{6.20}$$

$$+ k \sum_{j=2}^{q} u_j(\beta) \left(\Delta^1 \beta_j\right)^2 + k \sum_{j=3}^{q} v_j(\beta) \left(\Delta^2 \beta_j\right)^2, \tag{6.21}$$

with the penalty variables λ (for smoothness) and k (for monotonicity and curvature). The indicator variables u and v are defined as

$$u_j(\beta) = \begin{cases} 0 & \text{if } \beta_j - \beta_{j-1} \geq 0 \\ 1 & \text{otherwise,} \end{cases} \tag{6.22}$$

$$v_j(\beta) = \begin{cases} 0 & \text{if } \beta_j - 2\beta_{j-1} + \beta_{j-2} \geq 0 \\ 1 & \text{otherwise.} \end{cases} \tag{6.23}$$

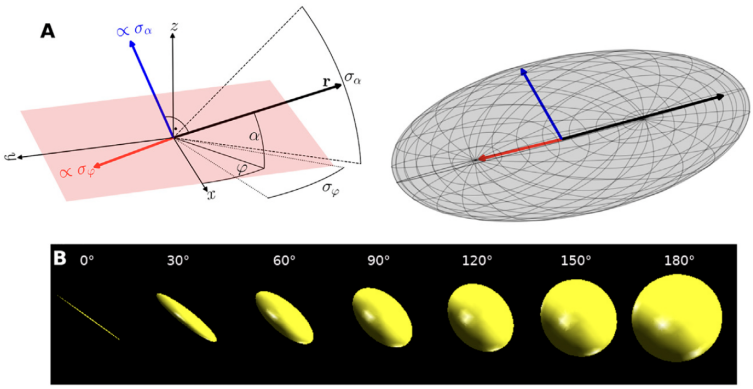

Figure 6.10: Ellipsoid construction (**A**) and visualization of a fiber with different orientation uncertainty $\sigma_\varphi = \sigma_{alpha} \in \{0°, 30°, \dots, 180°\}$. (**B**): The unit-length fiber vector **r** expresses the direction of the fiber-ellipsoid, the semi-axes are scaled correspondingly with σ_φ/π and σ_α/π. With increasing uncertainty, the fiber-ellipsoids become spherical which means that no specific orientation can be seen. Taken from [110].

These mathematical constraints can be incorporated into the model by a penalized iteratively reweighted least squares (P-IRLS) scheme [112, 110]. As implementation, the `pyGAM` package [113] is used. The penalty parameter k is set to $k = 10^9$, so the monotonicity ensuring terms have high influence in the optimization. The parameter λ is a hyperparameter which is optimized during the optimization. This happens in a grid search (a so-called hyper-parameter search) implemented by the `pygam` library by finding the lowest generalized cross-validation (GCV) of any model [109].

Preprocessing Because the data distribution $P(X|Y)$ has a large variance towards its maximum and the uncertainty CI values behave very steep, both axes undergo a log1p-transform ($f(x) = log(1 + x)$). This has also the advantage that the number of basis functions for the GAM model can be lower, so overfitting can be prevented. The number of basis functions was set to $q = 20$.

Preperation before sampling Given that only the function's shape is required, which will be learned, we can narrow down the selection in the predictor space (X) to limit the computational intensity of the MCMC sampling to a reasonable level. For each modality - Retardation, relative Thickness, and Inclination - a grid ranging from 0 to 1 (or 0° to 90°) was generated, with a grid size of N, such as $N = 200$. During the selection process for each modality, every grid point (with $N = 200$) was iterated through, and the image pixel $p(i, k)$ with the closest intensity value was chosen. It's worth noting that the same pixel $p(i, k)$ might be selected multiple times for different modalities. In such cases, the points are combined through the set union.

Visualization For the visualization of the fiber orientation as well as the respective uncertainty, the Direction φ, Inclination α, Direction CI σ_φ, and Inclination CI σ_α are translated to a triaxial ellipsoid with the main axis $\hat{x}$. The orientation vector gained from Direction and Inclination is normed to unit length vector **r** and the two orthogonal smaller semi-axes $\hat{y}$ and $\hat{z}$ are scaled as $\hat{x} = \sigma_\varphi/\pi$ and $\hat{z} = \sigma_\alpha/\pi$. The implementation was performed via `OpenGL` [114] in the software suite `PLIVis` [53]. The construction and the example visualization are shown in section 6.4.2.

Evaluation For the evaluation of the procedure 20 randomly selected brain sections from [71] were taken. On all selected sections 3D-PLI analysis as described in chapter 4 was performed with additional full section MCMC sampling on the CPU described in section 6.3 as a ground truth. For different sample sizes $N = 200, 400, 800, 1200, 1600, 2400, 3200$, the fitting performance, the median absolute prediction error, and visual inspection are performed.

6.4.3 Results

The uncertainty prediction evaluation for the out-of-plane angle CI with $N = 200, 400, 800$ is displayed in fig. 6.11. The smoothness of the GAM fit increases from $N = 200$ to $N = 400$. And from $N = 400$ to $N = 800$ further improvement can be seen. Subtracting the prediction map from the ground truth map shows similarly an improvement from $N = 200$ to $N = 400$, especially in the areas denoted by arrows 1 and 2. From $N = 400$ to $N = 800$ no further improvement can be seen. On the other hand, there is one prominent region in the lower part of the section, denoted by arrow 3, where the prediction error stays constant from $N = 200$ to $N = 800$. In general, the prediction error for the WM is lower than the prediction error of the GM.

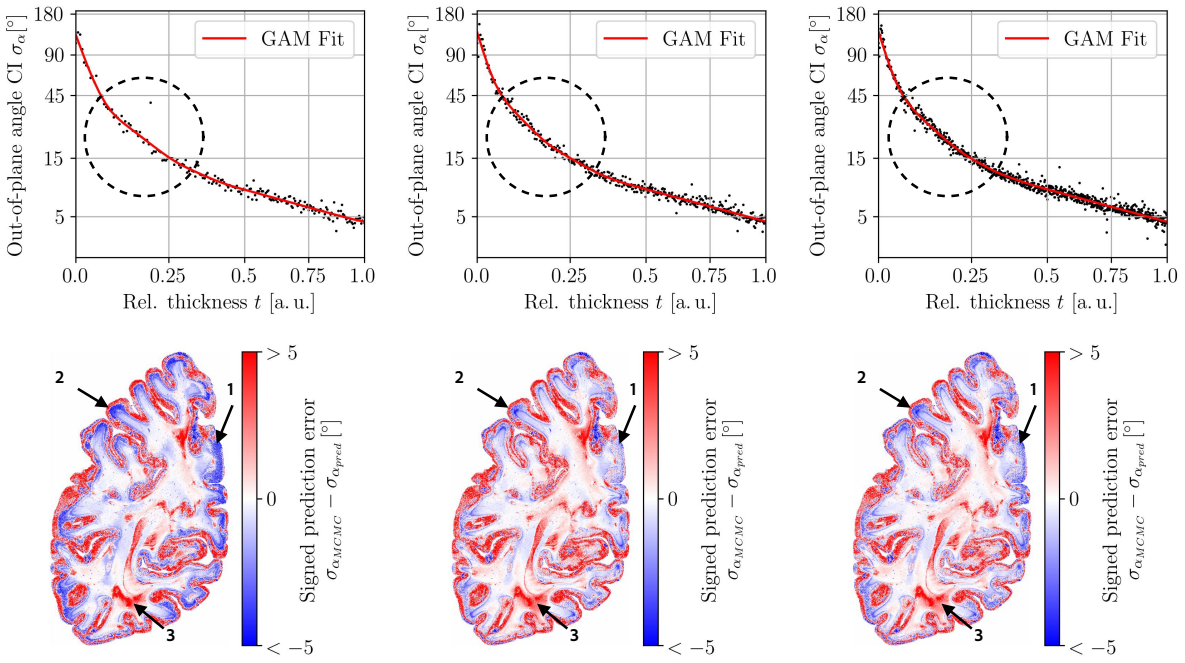

Figure 6.11: Uncertainty prediction results of the Out-of-plane angle CI (σ_α) for $N = \{200, 400, 800\}$ from **left column** to **right column**. In the **Top Row** the GAM Fit results of σ_α vs. the predictor variable rel. Thickness (t) is shown. In the **Bottom Row** the signed prediction error is shown. The fitted line in the region enclosed by the dashed circle shows a smoother behavior for increased sample size. The arrows 1 and 2 point to areas where the prediction error decreases with sample size. The arrow 3 points to an area where the prediction errors stay large with increasing sample size. Taken from [110].

Proceeding from this intermediate result the uncertainty prediction evaluation for $N = 800$ for the In-plane angle CI, the Out-of-plane angle CI, and the rel. Thickness CI is shown in fig. 6.12. All comparisons of prediction vs. ground truth show strong agreement.

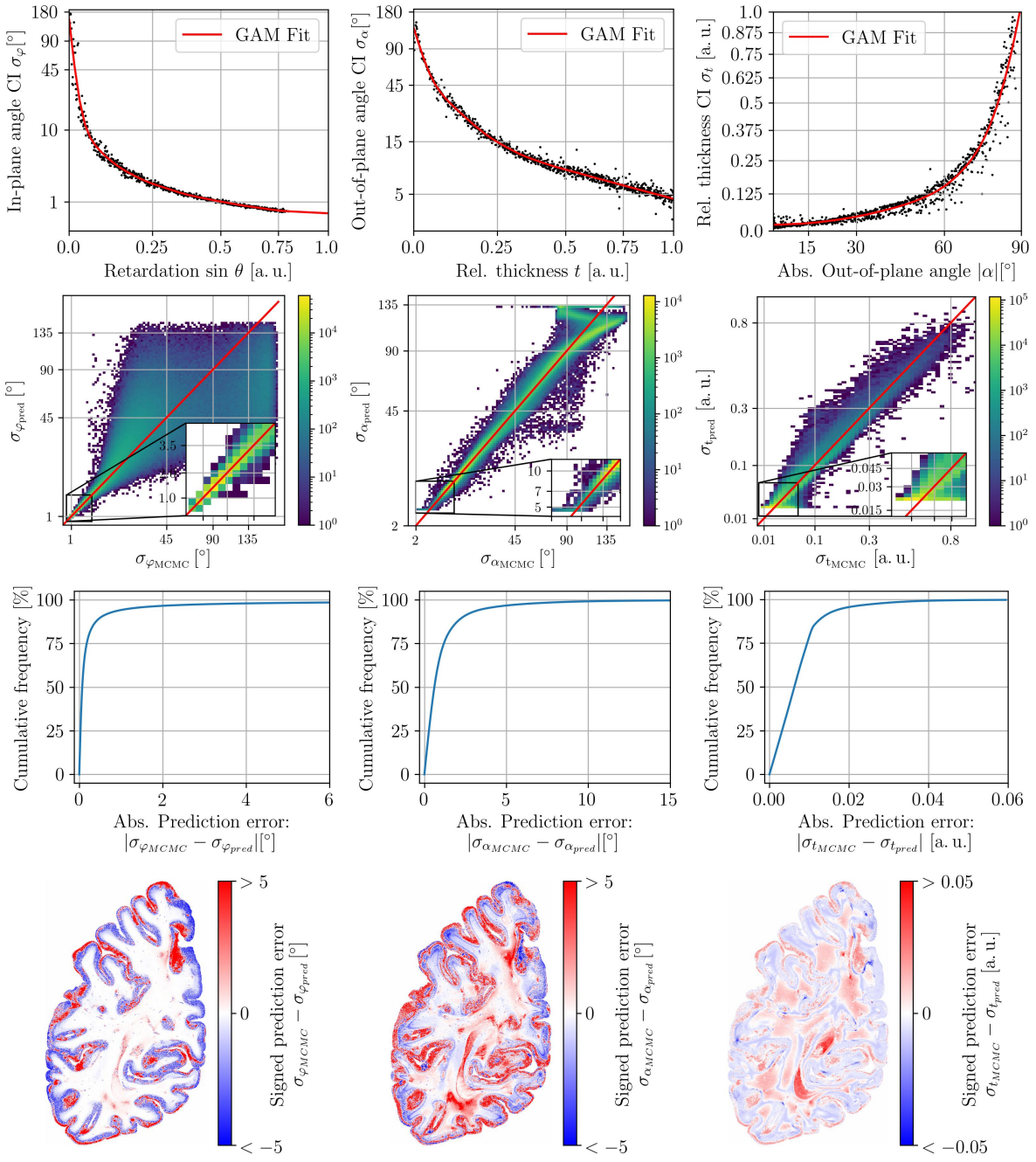

Figure 6.12: Uncertainty prediction results for $N = 800$ samples: In the **left column** the results for the In-plane angle CI ($\sigma_{\varphi,\text{pred}}$) are shown, followed by the results for the Out-of-plane angle ($\sigma_{\alpha,\text{pred}}$) in the **central column**, and by the results of the rel. Thickness CI $\sigma_{t,\text{pred}}$ in the **right column**. From **Top** to **Bottom** for each prediction the 1. GAM Fit with the corresponding predictor variable, 2. the scatter plot of the prediction vs. the ground truth, 3. the cumulative absolute prediction error, and 4. signed prediction error is shown. Taken from [110].

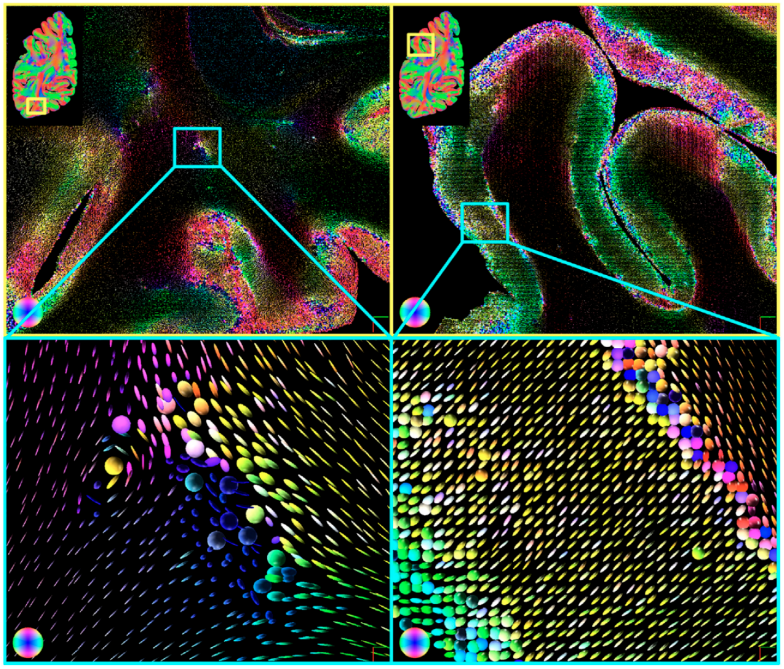

Figure 6.13: Ellipsoid visualization of two selected areas in a human brain section. The images on the **Left** show an area with crossing fibers and the images on the **Right** show an area of a transition of white matter to gray matter. Here, green indicates horizontal orientation, red indicates vertical orientation, and blue indicates out-of-plane orientation. Taken from [110].

The cumulative frequency plots show that more than 80% of the predicted values have an absolute prediction error of smaller than 2° (5°) for the In-plane angle CI (Out-of-plane angle CI) regarding the orientation CI values, and smaller than 0.02 for the rel. Thickness.

Signed prediction error maps show that the prediction error for the orientation CIs is lower in the WM than in the GM. For the In-plane angle CI the prediction error in the white matter is close to zero. Large deviations are solely visible in the outer layer. Contrarily, the signed prediction error map of the Out-of-plane angle CI shows a wider deviation *ribbon* in the cortex and only the core areas of the WM are close to zero. The predicted rel. Thickness CI values express a different behavior. Here, the deviations are almost overall homogeneously distributed.

The ellipsoid visualization is exemplarily shown for two ROIs of the processed section in fig. 6.13. The fiber orientations are more uncertain in the GM, in regions of crossing fibers (see the left image), and in the transition zone (see the right image). Regions of high uncertainty are right away visible through the spherical-becoming ellipsoids. In regions with high certainty the eye of the observer is guided by the prominent main axis of the ellipsoids with little scaling of the semi-axes.

6.4.4 Discussion

An uncertainty estimation via physically inspired regression was successfully implemented. Contrarily, to standard machine learning techniques such generalized regression approaches are much more interpretable without trading off flexibility. No mathematical modelling was needed, except for intuitive constraints on monotonicity and curvature. The predicted uncertainty maps are in great accordance with the (fully computed) ground-truth. The new ellipsoid visualization can potentially serve as an alternative to the established Fiber Orientation Maps when the MCMC-based uncertainty sampling is applied after the least-squares analysis. This workflow extension is outlined in fig. 6.14. This could

serve as guidance for neuroscientists when parcellation on the basis of FOMs and visible fiber tracts is performed, because then the uncertainties could also be incorporated, see e.g., [115, 67]. Furthermore, the obtained uncertainties can inform tractography [116]. Proceeding from the 3D-PLI workflow the uncertainty estimation provides an extension of the workflow demonstrated in fig. 6.14. Additionally, overlays of the ellipsoid visualization onto PLI modality maps can be performed, an implementation using `VTK` [117] is demonstrated in fig. 6.15.

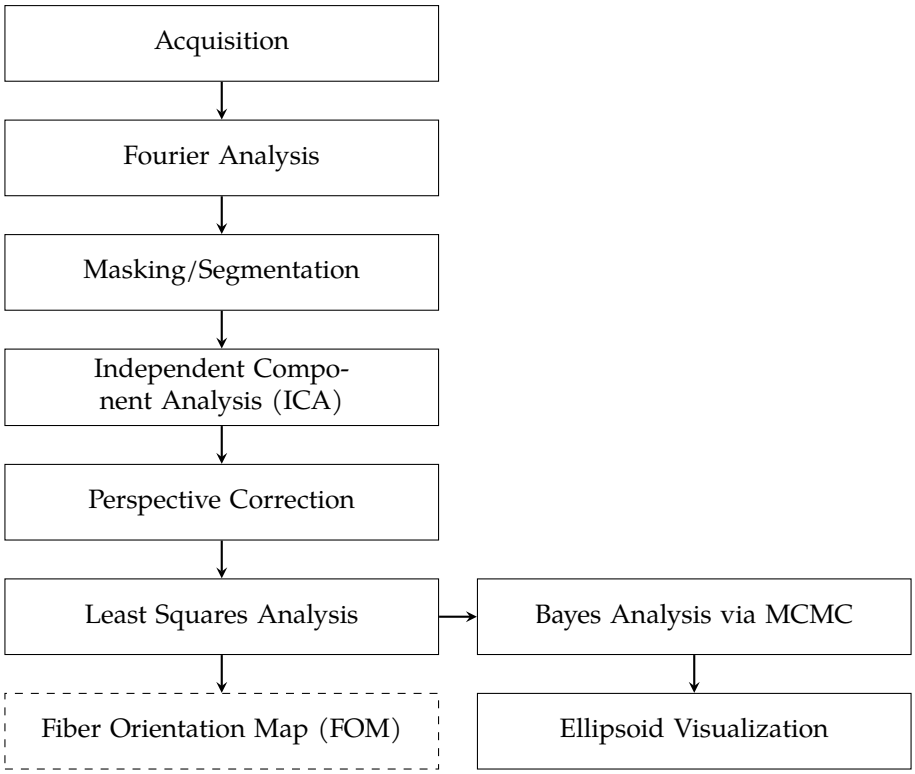

Figure 6.14: Workflow of the analysis considering the MCMC-based Bayes Analysis and the following visualization via ellipsoids.

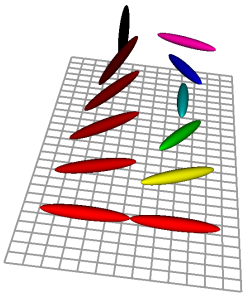

(a) **Left Row**: Change of Value if the Inclination α is increasing. **Right Row**: Change of Hue when the Direction φ is increasing.

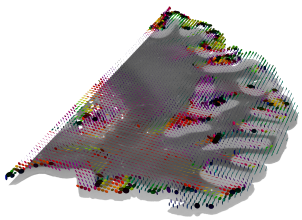

(b) Ellipsoids visualization of the frontal part of the 920er section with underlying Transmittance.

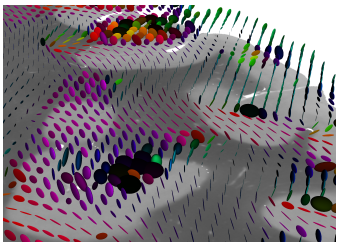

(c) Ellipsoids visualization of the frontal part of the 920er section with underlying Transmittance, zoomed in.

Figure 6.15: Ellipsoid visualization and overlay onto 3D-PLI Transmittance modality using `VTK` [117].

The runtime for the analysis becomes negligible, since for $\approx 1\,\mathrm{s/pixel}$, e.g., $N = 400$, translates to about 400 s, which can be reduced to a few seconds with the CPU implementation using up to 128 cores.

Part IV

Bridging Modalities and Scales

Chapter 7

Bridging Modalities and Scales

While the previous chapters dealt with the workflow and analysis of two-dimensional sections, the ultimate goal is to reconstruct the brain as a three-dimensional volume. In recent years, much effort has been devoted to the registration of 3D-PLI measurements to accommodate multi-scale, multi-modality data, and the utilization of realistic deformation models [118]. Additionally, because the 3D-PLI modalities Direction and Inclination contain directional information, the orientation values have to be corrected after registration [119]. Finally, tractography and visualizations can be performed using the reconstructed volumes, enabling visualization of the resulting fiber pathways [53].

However, the analysis for all the steps from image acquisition, workflow processing, registration, and volume reconstruction presents a huge undertaking. For the macaque brain, registration and coregistration with histological staining and MRI have been achieved, and new approaches for a hybrid (PLI-DWI) tractography ansatz have been studied [120]. But a systematic approach that uses the Blockface images to reconstruct 3D-PLI volumes for bias-free registration is missing, see [120]. Additionally, correlation studies of DWI vs. 3D-PLI have not yet used 3D-PLI with oblique views to infer the 3D fiber orientation directly (or respectively the rel. Thickness) [121].

This chapter focuses on building upon the developed workflow to bridge the gap between workflow results and established research software, facilitating correlational analysis between MRI and 3D-PLI (with oblique views). Finally, first results of the correlational analysis of myelin measurement with MRI, specifically the Myelin Water Fraction (MWF), and 3D-PLI modalities in the human brain are presented.

7.1 Introduction

Mollink et al. claimed that the Retardation maps can be used as a semiquantitative measure for myelin density to detect pathological changes in histologic sections if the sections and the ROIs are carefully chosen [122]. Complementary, from the studies by Menzel et al., we know that Retardation and Transmittance have to be taken into account to distinguish between areas of low myelination and high myelination [81, 86]. However, as Retardation is impaired by steep and crossing fibers and the Transmittance is also impaired by steep fibers, steep fibers remain a problem. Since the Least Squares Analysis of 3D-PLI data with oblique views enables reconstruction of the Inclination angle, the introduced rel. Thickness might be an Inclination-corrected measure of myelination.

Furthermore, no studies have been performed to examine the relationship between 3D-PLI modalities and myelin measures besides rough visual comparison (e.g., see [14]). Furthermore, myelin-staining is not quantitative [123]. Instead, we will compare unstained histological sections measured with 3D-PLI with myelin-water-fraction (MWF) [124, 125] volumes from MRI of the same brain. The MRI measurements were performed, and the dataset was provided by the group of Cyril Poupon at Neurospin in Saint-Aubin/Saclay. The corresponding preparation of the tissue (the Chenonceau Brain) after the MRI scan is described in appendix A.3.

7.2 Material and Methods

The 3D-PLI modalities are first prealigned with the Blockface images via 90°, 180°, or 270° rotation following a geometric initialization. Because the distortions are large, a ROI is selected in both the Transmittance and the Blockface image. After performing this manual process on consecutive sections, the transformations are used as initial transformations for further Rigid, Affine, and SyN[1] registration. The resulting affine transformation and the warp field are then applied to the different modalities, and image volumes are created for further processing. For the Direction and Inclination, the reorientation after warping and transformation is performed as described by Palm et al. [119].

The Blockface volume is initially aligned and registered on the MRI anatomy volume within 3D-Slicer utilizing the `SlicerANTs` extension[2] with Rigid, Affine, and SyN in 3D. This transformation is then used to transform the (Blockface registered) PLI modality volumes. The following correlative analysis can then be performed staying inside the 3D-Slicer software ecosystem[3].

The necessary steps for correlative analysis of 3D-PLI and MRI include therefore:

1. Interactive Preregistration
2. Registration and Reorientation
3. Volume creation
4. 3D-Registration and Correlative Analysis.

In the following study, the reorientation of Direction and Inclination is only applied from the registration step of 3D-PLI to the Blockface images, but not from the Blockface to the MRI volume. Here, the Inclination is only used as a measure of flatness.

[1] "SyN": Symmetric normalization: Affine + deformable transformation, with mutual information as an optimization metric [126].

[2] `https://github.com/netstim/SlicerANTs`

[3] Furthermore, the analysis steps can be written programmatically inside of Jupyter Notebooks through the `SlicerJupyter` Extension, see `https://github.com/Slicer/SlicerJupyter`.

7.2.1 Interactive Preregistration

The measured and processed 3D-PLI images represent objects in physical space. In 3D-PLI, these are the measurements of the sections cut from the respective brain. While the data is saved on the disk as an array and is constituted by pixel values addressed by the indices i and j, the corresponding sections have a certain thickness ($\Delta s = 50\,\mu\text{m}$) and the pixels have a specific spacing in the x and y directions, here called x_s and y_s. (Since the camera pixel are of quadratic size, we have $x_s = y_s$). The pixel size of the LAP images is 60.0 µm or 40.0 µm, depending on the camera configuration, and the pixel size of the LMP-3D is 1.85 µm. Every 2D-tuple (i, j) can thus be converted to a 3D-coordinate-tuple (x, y, z) by considering an origin point (x_o, y_o, z_o). The first two, x_o and y_o, can be chosen arbitrarily (e.g., $x_o = y_o = 0\,\mu\text{m}$), and the latter shall be set to $z_o = \texttt{section\_id} \cdot 50\,\mu\text{m}$. This is illustrated in fig. 7.1.

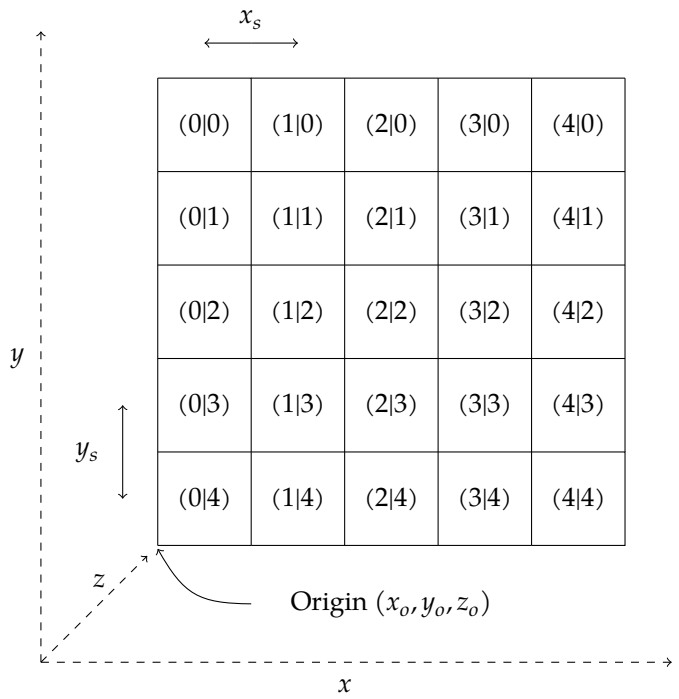

Figure 7.1: Example image with five pixel in width and five pixel in height. The indices $(i|j)$ are denoted with an integer starting from the top-left. The image is a representation of an object in the physical domain, so its pixel have a specific spacing and the object is lying in some depth z_0 and is expanding from the origin (x_0, y_0, z_0).

When the sections are transferred from the microtome to the object slide, the orientation of the section or parts of the section can vary concerning the Blockface images. They can be placed e.g., by 90° rotated on the object slice (in the trivial case) or parts of the sections can rupture and float in every which way. As denoted in chapter 3 the Blockface images (with a pixel size of 32.2 µm) can be seen as the reference space of the PLI images, because they show the shape and orientation of the sections before the cutting process. Thus, the measured sections have to be mapped to the Blockface sections or respectively, the Blockface volume.

This process of mapping the PLI image, here the *moving image*, to the Blockface, here the *fixed image* is called image registration [127]. But before the (complete) registration, a starting point is needed to account for the described difficulties.

The initial alignment of images in the field of histology is difficult because they can differ in appearance (multimodal acquisition) and can be strongly deformed [128]. However, for some use cases, we might not need to register every part of the measured section to the Blockface image or we need to perform the registration in multiple steps, so that the registration of a ROI would be enough. For this, an interactive Preregistration tool was developed using `plotly` and `dash` [129]. The screenshot of the program is shown in fig. 7.2.

The ROI has first to be selected in the 3D-PLI image (*moving image*) (here, in the Transmittance) as well as in the Blockface image (*fixed image*). Afterward, the ROI of the moving image has to be rotated (interactively) clockwise or counter-clockwise to match the orientation of the ROI of the fixed image (see fig. 7.4). The translational alignment is implemented via geometric alignment.

The initial transformation is then constructed internally with the `SimpleITK` [130, 131] function `CenteredTransformInitializerFilter` as shown in listing 7.1. The constructed (affine) transform $\mathbf{A}_{\text{init}}$ can be saved afterward. Additionally, the ROIs for the *moving image* and the *fixed image* can be saved as masks (see fig. 7.3).

Listing 7.1: Python code for creation of the initial transformation (`init`) consisting of a rotation around the geometric center and a translation of the geometric center of the moving image to the geometric center of the fixed image.

```
init = sitk.CenteredTransformInitializer(
    self.fixed_image,
    self.moving_image,
    euler_transform,
    sitk.CenteredTransformInitializerFilter.GEOMETRY,
)
```

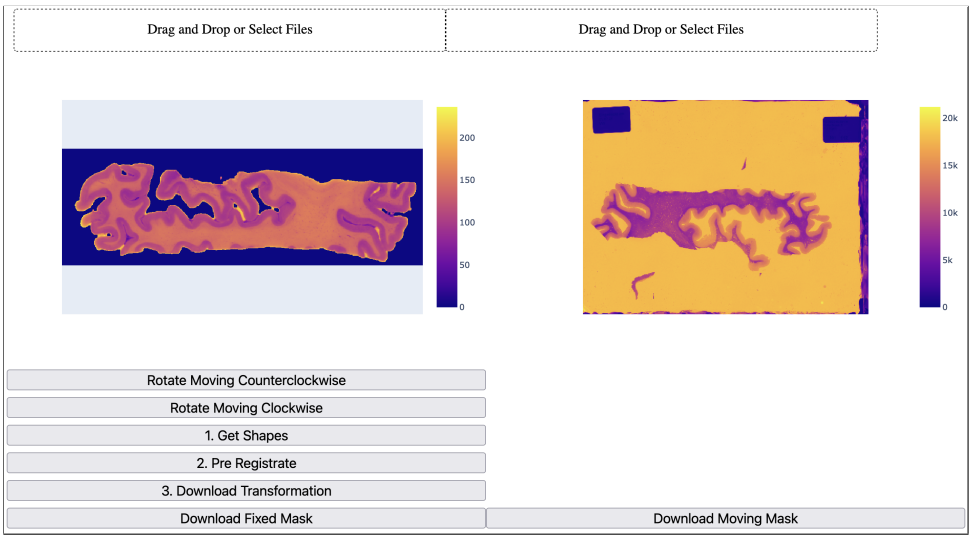

Figure 7.2: Screenshot of the Preregistration tool after loading the images, **Left:** Blockface image and **Right:** PLI Image. Here, the `plasma` colormap is used.

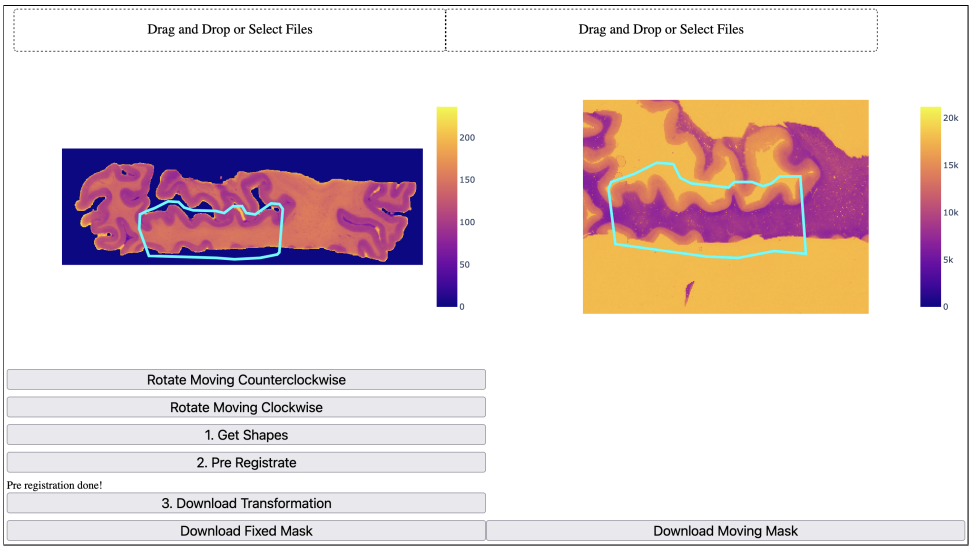

Figure 7.3: Screenshot of the Preregistration tool after marking the ROIs and two 90° rotations of the moving image (B). The shapes are internally converted into polygons and the vertices are used for the fixed-mask and the moving-mask generation. In the case of the moving image, the rotational transformation is inverted so that the generated moving mask matches the unrotated file. The two masks can then be downloaded. The preregistration transform is saved as an Euler2DTransform-File and can also be downloaded to be used as an initial transform for later registration. Here, the `plasma` colormap is used.

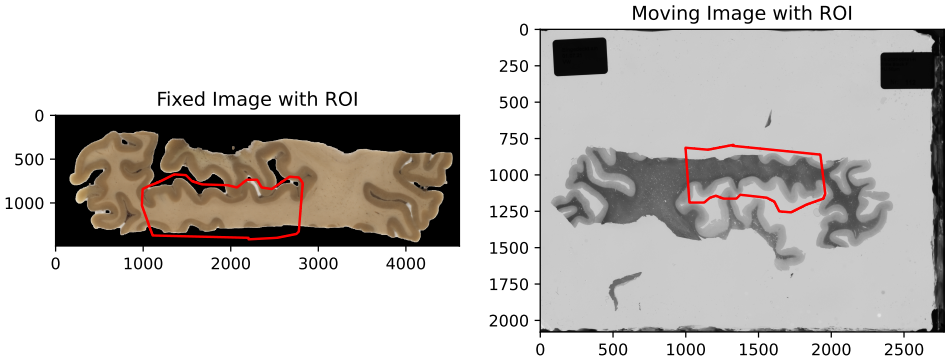

Figure 7.4: The fixed image (left), the Blockface image, and the moving image (right), the Transmittance Image, with their corresponding ROIs (red). The results of the Preregistration consist of a translation and a rotation to align the centers of both ROIs in the right orientation. Here, the rotation is a simple rotation of 180° with a following translation to align the geometric centers.

7.2.2 Registration and Reorientation

After the generation of an initial transform and a mask for the ROI. The registration of the PLI images (using the Transmittance) on the Blockface images can be performed. While the construction of the initial transform is done via `SimpleITK` (see section 7.2.1), the registration is performed with `ANTsPy`[4]. Because of the large deformities, `SyNRA` was chosen as a model. This model consists of an initial Rigid registration, followed by an Affine registration, and finalized by a diffeomorphic registration. After saving the linear transformation **A** (combining the Rigid and the Affine transformations) and the displacement field **T**, the transformations can be applied to all the other modalities to resample them into the domain of the Blockface image.

In resampling, the obtained transformation is applied on all the pixels in the *fixed image* to get the respective neighborhood of pixel in the *moving image*. From this neighborhood, the final pixel value is then evaluated via interpolation. Here, nearest neighbor interpolation is used. After interpolation, the pixel value is extracted to the pixel position of the fixed image. This process is called inverse mapping [84].

While the resampling of images with scalar values (e.g., Transmittance, Retardation) is straightforward, the Direction and Inclination need to be reoriented, because the orientation (given by Direction and Inclination) is not adjusted by the resampling. If we apply e.g., a rotation around 90° on a Direction image and resample the Direction values, the orientation resembled by this value will still point in the same (former) direction. This problem is outlined in fig. 7.5. Note that a 90° rotation in the space of the *moving* image is equivalent to a -90° resampling transformation.

To incorporate the changes in orientations through the transformations (the linear transformation A, and the displacement field B), we need to apply some (local) inverse linear transformation $\mathfrak{A}^{-1}$ to the fiber vector

$$\begin{pmatrix} x' \\ y' \\ z \end{pmatrix} = \mathfrak{A}^{-1} \begin{pmatrix} x \\ y \\ z \end{pmatrix} = \mathfrak{A}^{-1} \begin{pmatrix} \cos\alpha\cos\varphi \\ \cos\alpha\sin\varphi \\ \sin\alpha \end{pmatrix} = \mathfrak{A}^{-1}\vec{f}. \tag{7.1}$$

Since the registration is happening in the XY-plane it is sufficient for the reorientation to consider the first two components of the fiber vector

$$\begin{pmatrix} x' \\ y' \end{pmatrix} = \mathcal{A}^{-1} \begin{pmatrix} x \\ y \end{pmatrix} = \mathcal{A}^{-1} \begin{pmatrix} \cos\alpha\cos\varphi \\ \cos\alpha\sin\varphi \end{pmatrix}. \tag{7.2}$$

The reoriented fiber vector is then obtained via normalization

$$\vec{f'} = \left(\frac{x' - \sqrt{1-z^2}}{\sqrt{x'^2 + y'^2}}, \frac{y' - \sqrt{1-z^2}}{\sqrt{x'^2 + y'^2}}, z \right)^T. \tag{7.3}$$

In eq. (7.2) $\mathcal{A}^{-1}$ can be identified with the inverse (global) affine transformation $\mathbf{A}^{-1}$ in case no diffeomorphic registration is performed, or with the approximated (local) affine transformations

$$\mathcal{A}_{ij}^{-1} = \mathbf{A}^{-1} \left(\mathbf{J} + \mathbf{I}\right)_{ij}, \tag{7.4}$$

with **J** being the Jacobian of the inverse displacement field $\mathbf{T}^{-1}$ and **I** being the identity matrix, if the complete registration is performed. Note that i, j denotes the index of the Direction and Inclination

[4] `https://github.com/ANTsX/ANTsPy`

images since the transformation is local. In both cases, we need the full affine transformation since we need to account for sheering [119].

Afterwards, the reoriented Direction and Inclination map can be obtained via pixel-wise (i, j) computation of

$$\varphi' = \arctan2(x', y') \tag{7.5}$$

and reparametrization

$$\varphi' \mapsto \varphi \in [0°, 180°) \tag{7.6}$$

$$\alpha' \mapsto \alpha \in [-90°, 90°). \tag{7.7}$$

Since `ANTsPy` performs the registration on the transposed array (and returns the transposed transformed array, contrary to `SimpleITK`) the composition of the affine linear transformation of the preregistration $\mathbf{A}_{\text{init}}^{-1}$ and the local affine transformations $\mathbf{A}^{-1}(\mathbf{J}+\mathbf{I})_{ij}$ for the reorientation needs to be of the form $a_{ji}b_{jk}$ rather than $a_{ij}b_{jk}$. This is realized via the `np.einsum` function, where vectorization over subsequent indices is indicated by ellipsis as shown in listing 7.2.

Listing 7.2: Vectorized chaining of transformations and application to the vector image via `np.einsum`.

```
# Composition of affine (A^{-1}_{init}) and local affine transformations A
    ^{-1}(J+I)
trafo_combined = np.einsum(
"ji,jk...->ik...",
trafo_affine_inverted,
trafo_syn_inverted,
)

# Vectorized dot-product of composite transform and vector image
moving_vector_stack_upper_part_reoriented = np.einsum(
"ij...,j...->i...", trafo_combined, moving_vector_stack[:2, :, :]
)
```

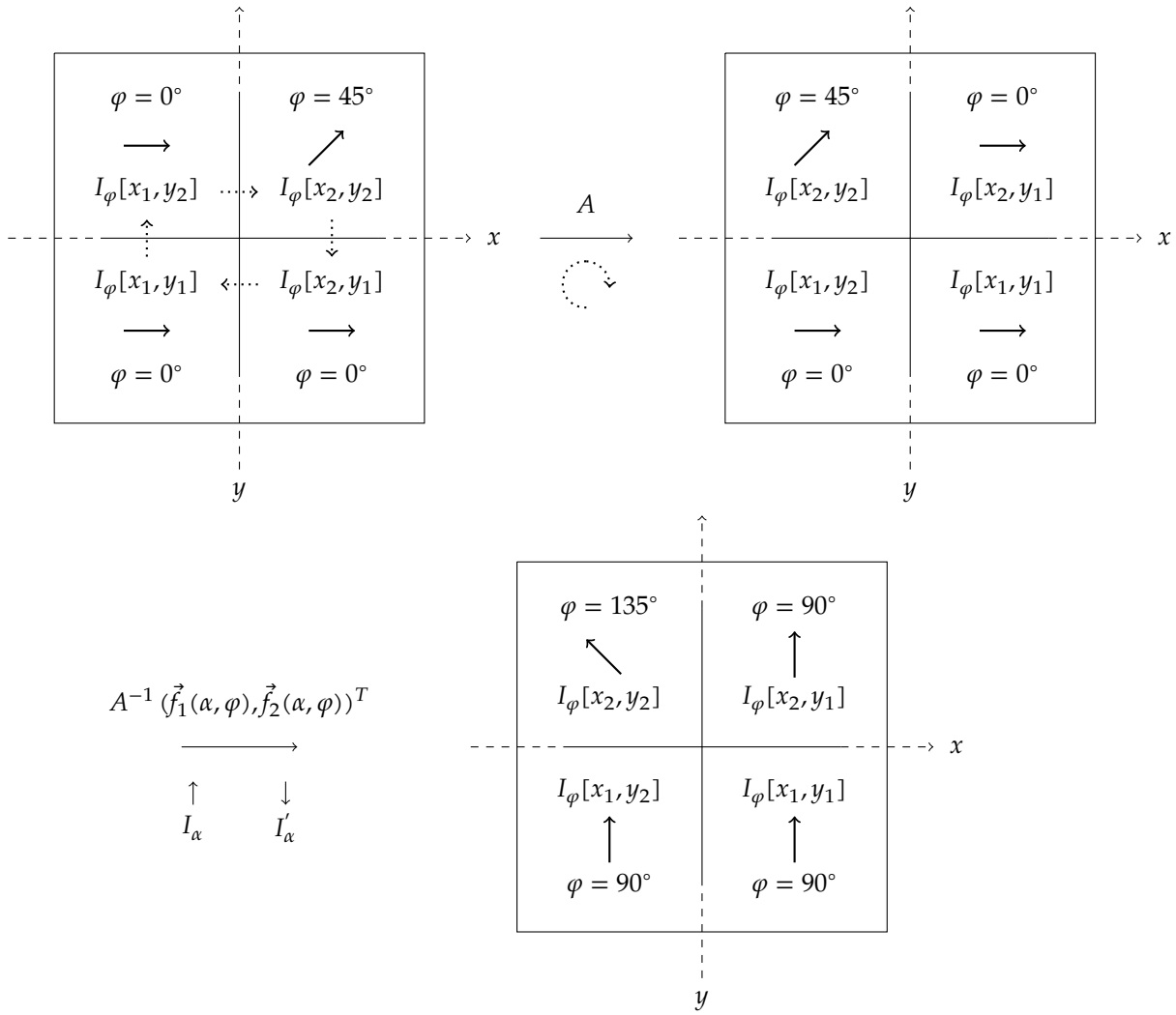

Figure 7.5: The Direction image I_φ consisting of four pixels is rotated CCW via resampling CW with the linear transformation A in the same image domain. The values are *pulled* against the dotted arrows representing the transformation (inverse mapping). The change of the position of the pixel values $I_\varphi[x_i, y_i]$ results in a 90° CCW rotation for the viewer in front of the image. However, after the first step in the **Top-Row**, all φ values are still the same and the corresponding orientations represented by the black arrows are still pointing in the same direction. As a consequence, in the **Bottom-Row**, the inverse transformation A^{-1} has to be applied on the x, and y coordinates of the fiber vector (constructed by the entries of I_φ and I_α) of each pixel (followed by normalization). Note that afterward a reparametrization might be needed to project the orientation values back to $\varphi \in [0°, 180°)$ and $\alpha \in [-90°, 90°)$.

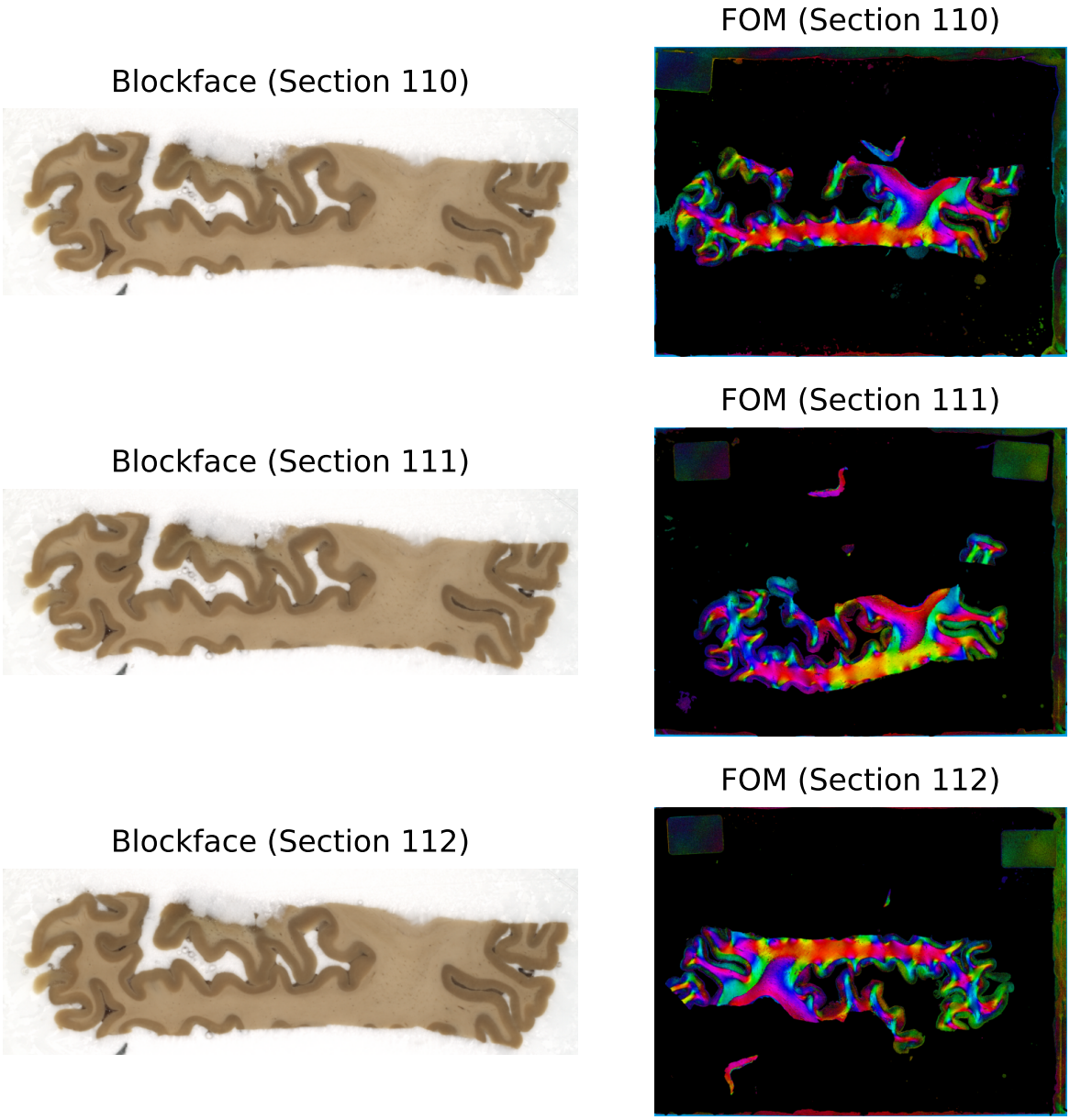

Figure 7.6: On the left **Left:** Blockface images of sections 110, 111, 112 and on the **Right:** Fiber Orientation Maps (FOMs) of the 3D-PLI prior to registration.

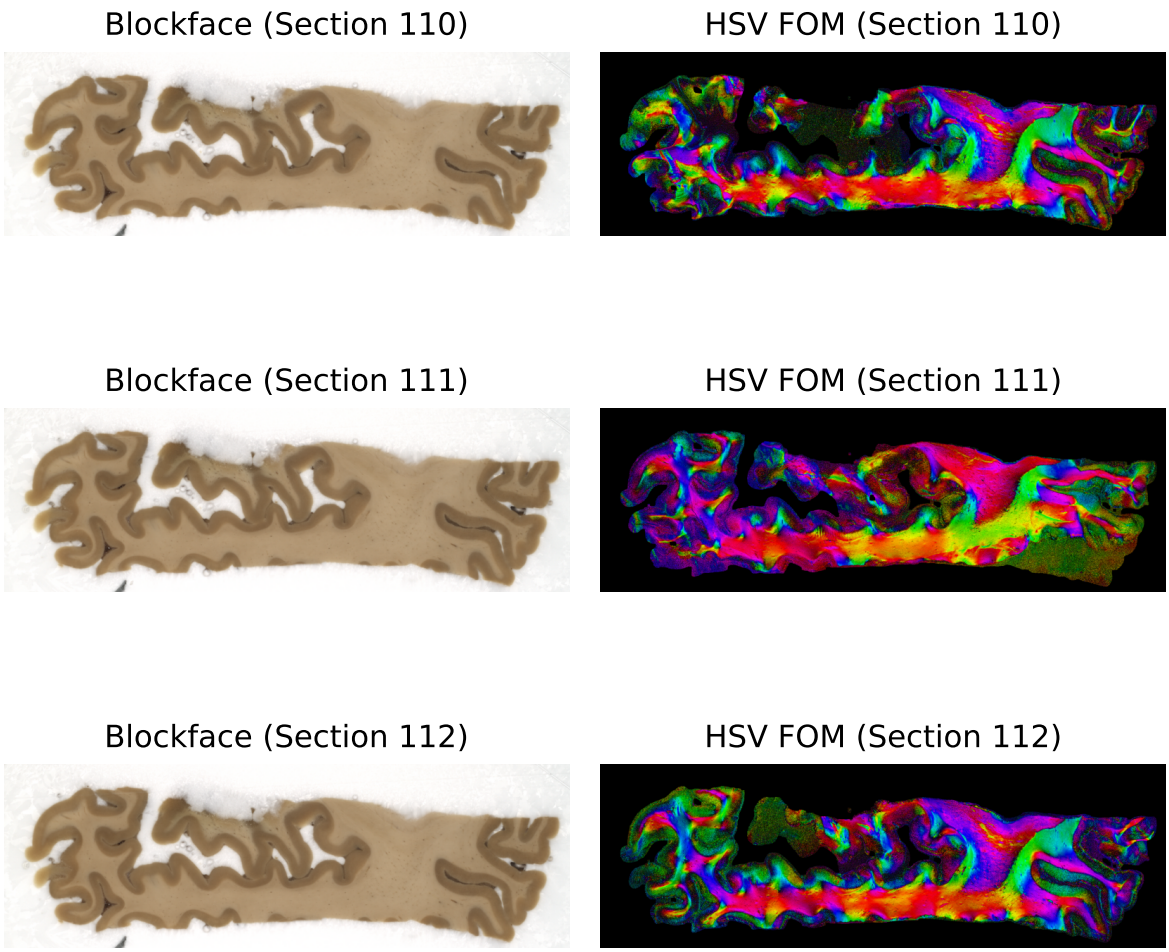

Figure 7.7: On the left **Left:** Blockface images of sections 110, 111, 112 and on the **Right:** Fiber Orientation Maps (FOMs) of the 3D-PLI after (partial) registration.

7.2.3 Volume creation

After registration and resampling of the scalar modalities (Transmittance, Retardation, and relative Thickness), the resampling and reorientation of the directional modalities (Direction, Inclination), as well as resampling of the corresponding scalar uncertainty modalities (see chapter 6), the individual modalities have to be combined to volumes. This is implemented e.g., for the Transmittance images by creating an array of images and defining the corresponding spacing for each dimension as a list. This is exemplarily shown in listing 7.3. Since for comparison with MRI the units for length are mm and the units in 3D-PLI are given in µm the values need to be divided by `1e3`. As described in section 7.2.1 we can set the physical origin to $(50\,\mu m, 0\,\mu m, 0\,\mu m)$.

Listing 7.3: Creation of an image volume with the `sitk` library.

```
spacing_z = section_thickness / 1e3
spacing_x = pixel_width / 1e3
spacing_y = pixel_height / 1e3

physical_origin = [(section_id - 1) * section_thickness / 1e3, 0, 0]

volume = sitk.GetImageFromArray(combined_arrs.astype(np.float32).T)
volume.SetSpacing([spacing_z, spacing_x, spacing_y])
volume.SetOrigin(physical_origin)
```

7.2.4 3D-Registration and Correlative Analysis

After the 2D registration of the resampling of the 3D-PLI modalities onto the Blockface image, the Blockface volume has to be registered to the MRI anatomy volume in 3D. For this, an anatomical scan of the Chenonceau was provided in the resolution 150 µm and 200 µm. The volumes loaded into 3D-Slicer [132] were first manually aligned and then automatically registered via the `SlicerANTs` plugin. The MRI volume is the fixed image (since it serves as the reference), and the Blockface volume is the moving image. For the 3D registration, a Rigid transformation followed by an Affine and SyN registration was used. The different registration steps are visualized (from the initial alignment to the deformable registration) in figs. 7.8 to 7.11.

The obtained transformation of the Blockface image onto the MRI anatomy volume can then be applied to every 3D-PLI modality volume and resampled into the MRI volume to enable multi-modal comparison.

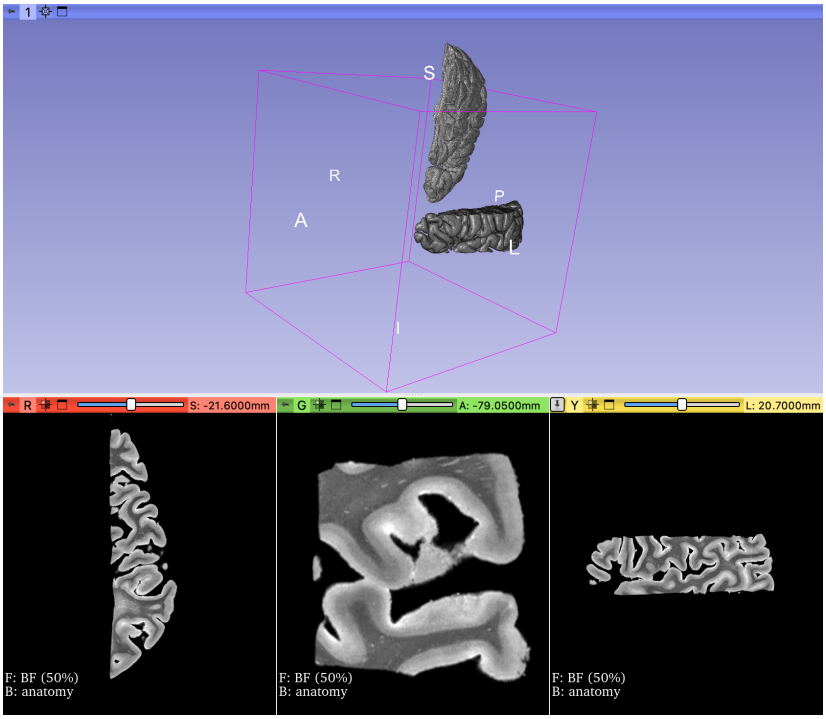

Figure 7.8: MRI (anatomy) and Blockface prior to initial alignment. The MRI volume appears in the lower row in gray and the Blockface volume appears in the lower row in magenta (here not visible, because the volumes have no overlap.)

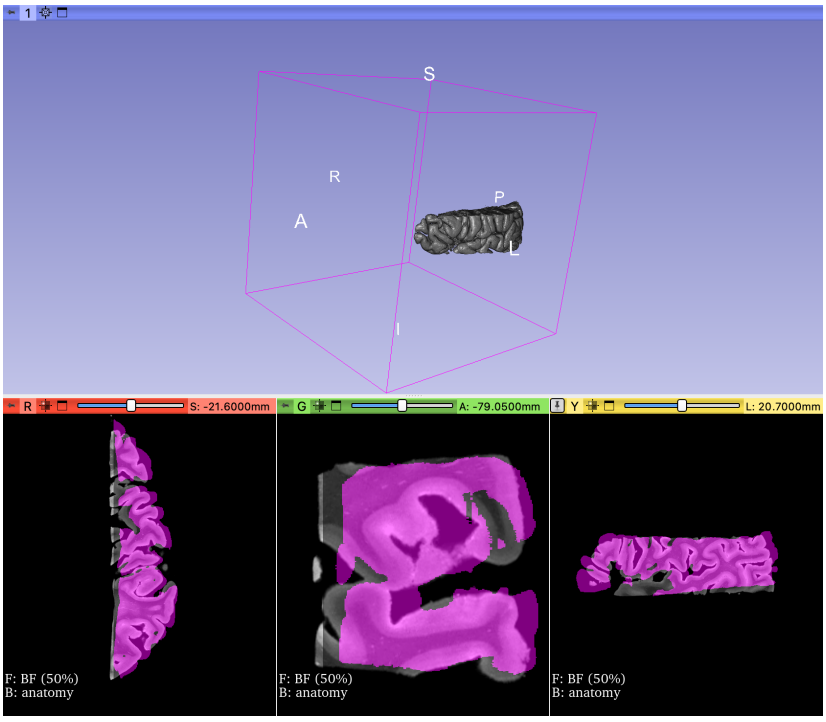

Figure 7.9: MRI (anatomy) and Blockface after manual initial alignment. The MRI volume appears in the lower row in gray and the Blockface volume appears in the lower row in magenta.

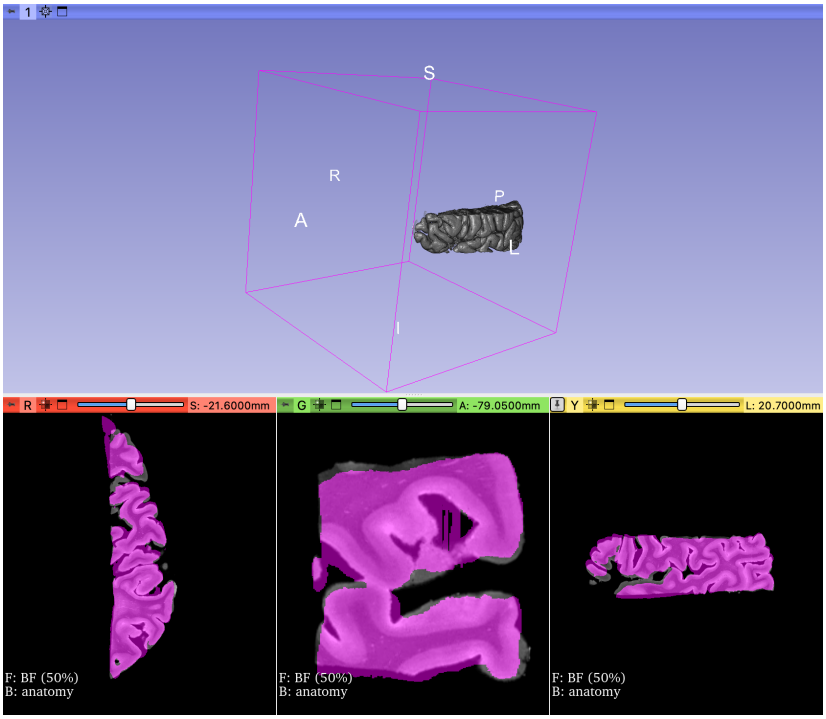

Figure 7.10: MRI (anatomy) and Blockface after rigid+affine registration. The MRI volume appears in the lower row in gray and the Blockface volume appears in the lower row in magenta.

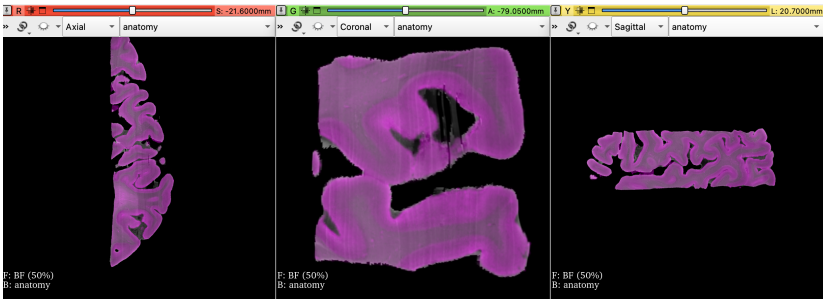

Figure 7.11: MRI (anatomy) and Blockface after rigid+affine+deformable registration. The MRI volume appears in the lower row in gray and the Blockface volume appears in the lower row in magenta.

7.3 Results

The registered ROI is shown in fig. 7.12. It is the result of rigid+affine+free-field deformation from the Blockface Volume (32 µm x 32 µm x 50 µm) to the MRI Volume (150 µm isotropic voxel size) and rigid+affine+free-field deformation from the histological sections (section 105 to 115), the PLI measurements (60 µm x 60 µm), to the Blockface sections (32 µm x 32 µm).

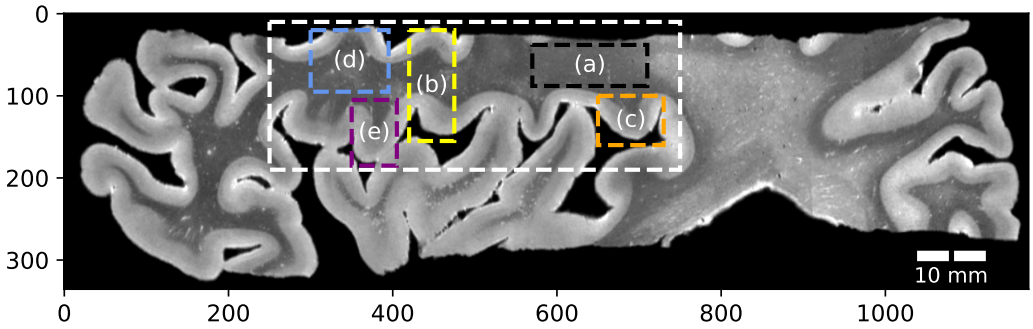

Figure 7.12: The selected ROI for the analysis with five ((a) to (e)) specified regions for further analysis. Here, the anatomy (MRI, 150 µm) is shown. The white dashed square denotes the area where the registration is adequate for correlational analysis.

The analysis is split into five different parts ((a) to (e)), which are annotated in fig. 7.12. Part (a) represents an area of high Retardation, part (b) is for results of Retardation vs. MWF and rel. Thickness vs. MWF, part (c) for a transition between Gray Matter and White Matter, and parts (d) and (e) show low-myelinated areas in the white matter.

Results of Part (a) The highest Retardation value was found to be 0.44 [a.u.], with a corresponding reference Transmittance of 8680 [a.u.], analogously the reference Inclination measures −3° and the reference relative Thickness measures 0.32 [a.u.]. The sub ROI is shown in fig. 7.13.

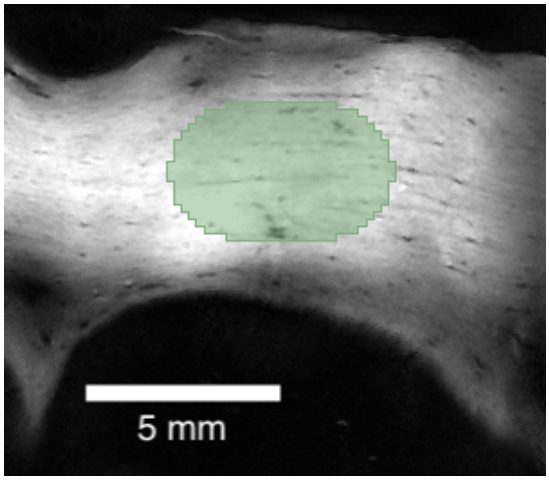

(a) Retardation map of the selected brain section: The area of maximum Retardation is marked with a green segmentation area.

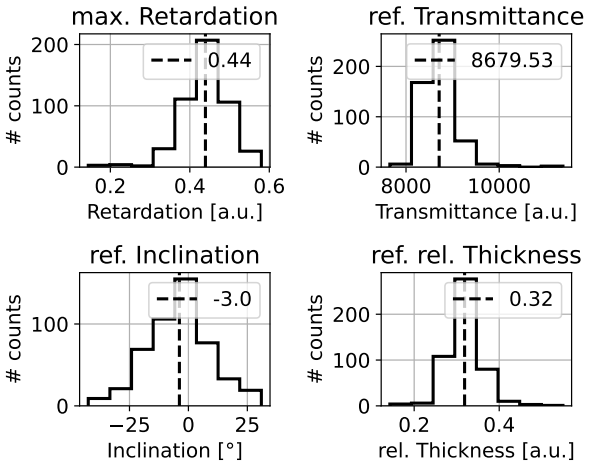

(b) Histograms of the area of maximal Retardation for (from left to right) Retardation, Transmittance, Inclination, and relative Thickness. The dashed line marks the respective mean values.

Figure 7.13: Retardation, and histograms of the different modalities in the area of maximal Retardation found in area (a) in fig. 7.12.

Results of Part (b) In fig. 7.14a five points of diameter 1.3 mm on a line of length 10.9 mm from gray matter to white matter and back to gray matter are chosen and segmented, and their mean and standard deviation are plotted as a line profile in fig. 7.14b. The Retardation and MWF of the five sampled points (0 - 4) are positively correlated. The transition of gray matter to white matter from point 0 to point 1 is characterized by an increasing Retardation and an increasing MWF. From point 2 to point 3 the MWF stays at the same value, and the Retardation is slightly increasing. After point 2 to point 3 and continuing to point 4 the MWF is again decreasing at the same rate as the Retardation and returns to the same values as the starting point.

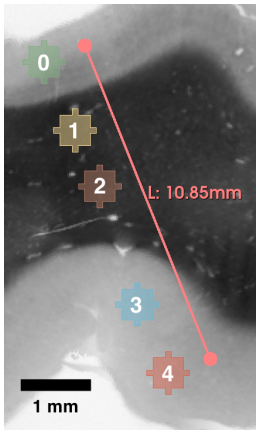

(a) Sampling of the Transition of GM to WM to GM with five selected points across the tissue.

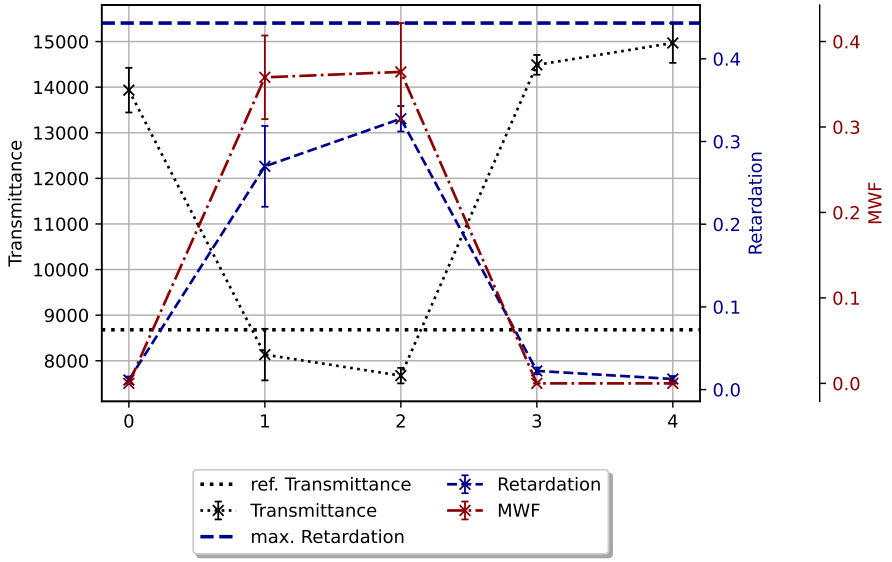

(b) Pointwise measuring of Transmittance, Retardation, and Myelin Water Fraction from Point 0 to Point 4. The dotted lines mark the area of maximum Retardation and the corresponding reference Transmittance.

Figure 7.14: Transition from gray matter to white matter and back to gray matter in ROI (c) in fig. 7.12.

The Transmittance values are negatively correlated to MWF and Retardation. It starts at a point 0 at a value of 14000 [a.u.] and decreases to a value of 8000 lower than the reference Transmittance. From point 1 to point 2 it stays below the reference Transmittance. After point 3 the Transmittance increases again to a value greater than 14000 and stays at this level to point 4.

Results of Part (c) Inside of ROI (c) an area of 7x11=77 sample points of size 0.6 x 0.6 mm^2 is selected. The area spans the gray-to-white matter area of a gyrus. The sample points are shown in fig. 7.15 for MWF (fig. 7.15a), Retardation (fig. 7.15b), rel. Thickness (fig. 7.15c), and Transmittance (fig. 7.15d). (The latter is displayed solely for an overview.) They are split into three groups: white matter, grey matter, and segments that are lying on the border of white matter and gray matter. The resolution of the MWF (fig. 7.15a) is significantly lower and less structure is visible in the white matter part, contrary to the PLI modalities. For each segment in MWF, Retardation, and rel. Thickness the mean and standard deviation are calculated, following linear regression analysis of MWF vs. Retardation (see fig. 7.15b) and MWF vs. rel. Thickness (see: fig. 7.15c).

(a) Myelin Water Fraction (MWF, 200 µm)

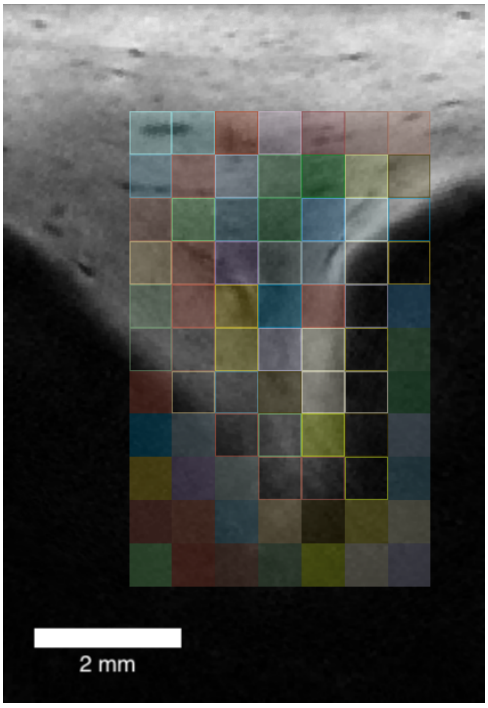

(b) Retardation (60 µm)

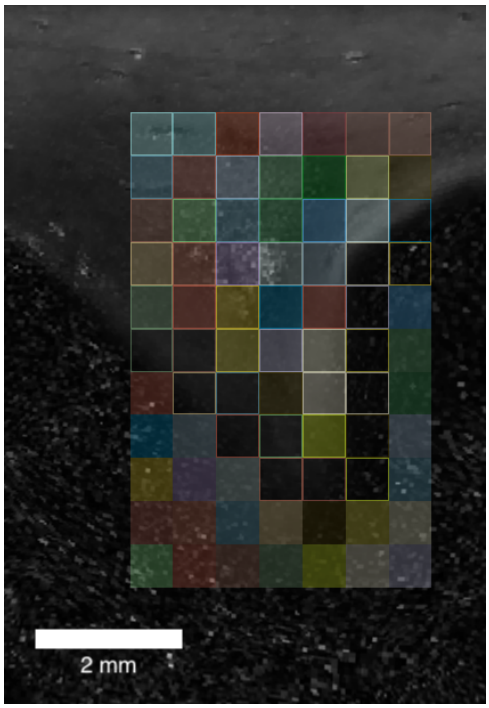

(c) rel. Thickness (60 µm)

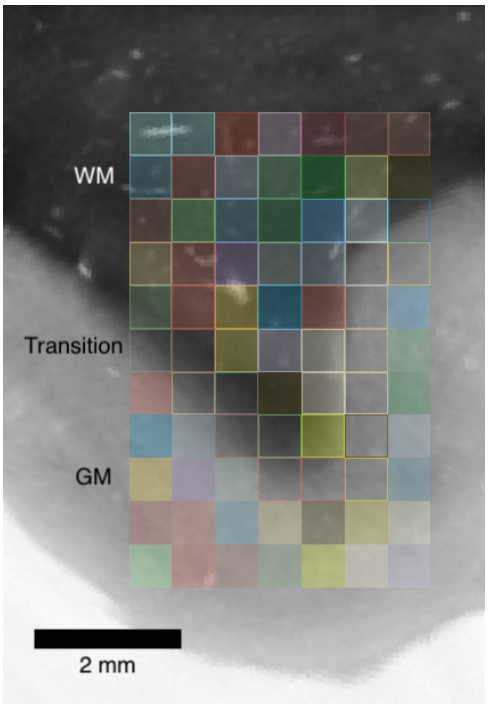

(d) Transmittance (60 µm)

Figure 7.15: Myelin Water Fraction (MWF), Retardation, rel. Thickness, and Transmittance map of the selected ROI. From the ROI $7 \times 11 = 77$ sample ROIs are selected. This selection is separated into White Matter (WM), Gray Matter (GM), and a Transition Zone which contains the area in between. From these samples, the mean and standard deviation is calculated.

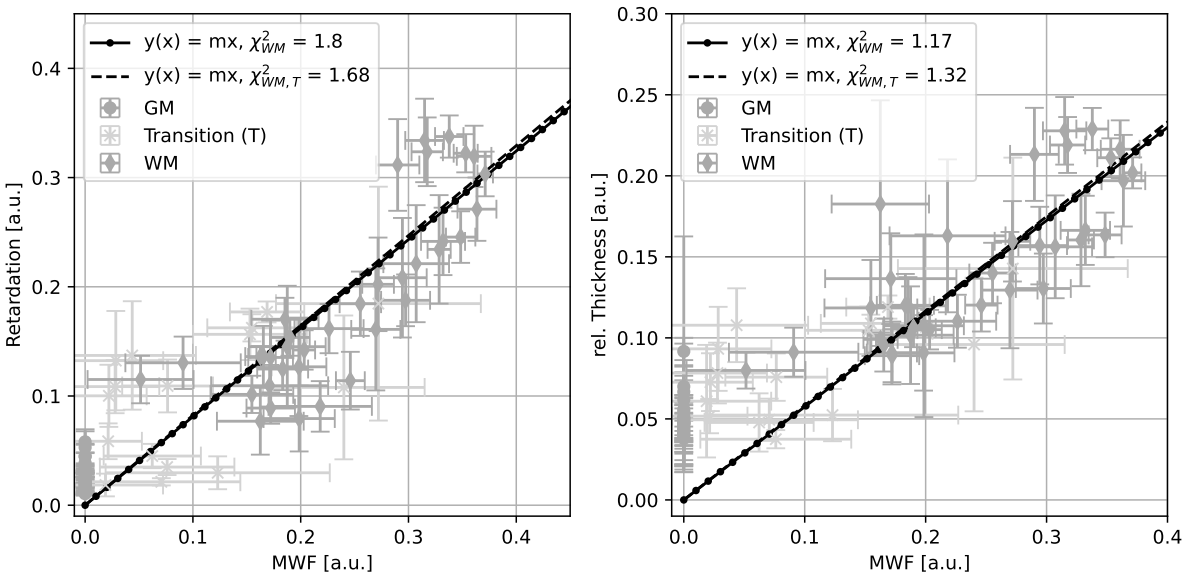

Figure 7.16: Scatter plot and regression analysis. **Left:** Myelin Water Fraction vs. Retardation and **Right:** Myelin Water Fraction vs. rel. Thickness.

The segments for MWF in the WM are close to zero, while the samples for Retardation and rel. Thickness show a distribution between 0.0 and 0.07 for Retardation and 0.0 and 0.1 for rel. Thickness. For the WM, and the Transition an increase in MWF shows an increase in Retardation and rel. Thickness. Orthogonal distance regression including WM points, as well as WM and Transition points, yields a reduced chi-square of 1.8 (1.68) for MWF vs. Retardation and 1.17 (1.32) for MWF vs. rel. Thickness. The GM segments are excluded from the ODR.

Results of Part (d) and (e) In fig. 7.17, two lines through Part (d) and Part (e) are shown. Line 1 is displayed on the left and Line 2 is displayed on the right. The lines consist of 13 (15) segments along a distance of 7.2 mm (12.2 mm) and crossing two local low-myelin areas which are visible as dark spots in the MWF maps (see fig. 7.17a and fig. 7.17b), and as white spots in the Transmittance maps (see fig. 7.17e and fig. 7.17f). In the two Retardation maps (see fig. 7.17c and fig. 7.17d) no spatial corresponding are directly apparent. Furthermore, in the Retardation map of Part (e) (see fig. 7.17d) an area of inclined fibers is visible by a darker spot adjacent to the middle of the line.

The line profiles for MWF, Retardation, Transmittance and additionally Inclination are shown in fig. 7.18 and fig. 7.19. Line Profile 1 shows a positive correlation between MWF and Retardation and a negative correlation between MWF and Transmittance. The Inclination values are for the points 0 to 12 around 0°. Line Profile 2 shows a weak correlation between MWF and Retardation, the broad local minimum of the Retardation from Point 6 to Point 9 does partially overlap with the local minimum of the MWF from Point 8 to Point 10. For the MWF vs. Transmittance, the position of the local maximum of the Transmittance in Points 8 and 10 corresponds to the position of the local minimum of the MWF. The Inclination for Line Profile 2 starts around 0° and falls to -30° from Point 2 to Point 5 and stays between -20° and -30° to the end of the Profile.

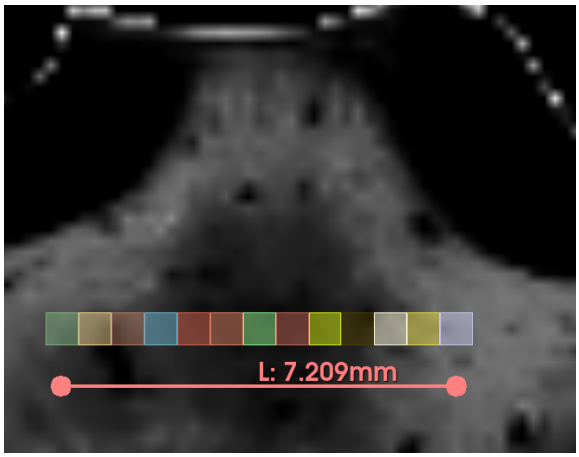

(a) Myelin Water Fraction (200 µm). Line 1.

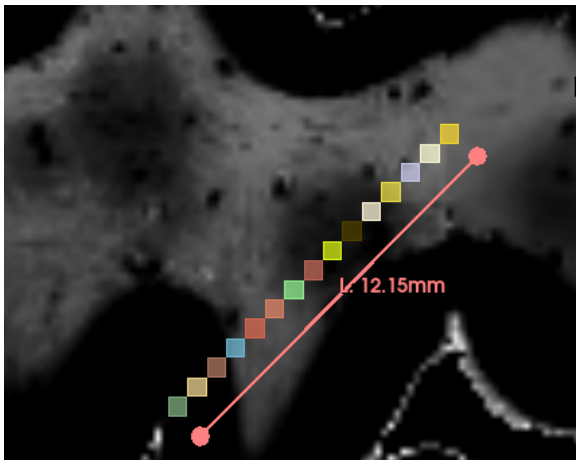

(b) Myelin Water Fraction (200 µm). Line 2.

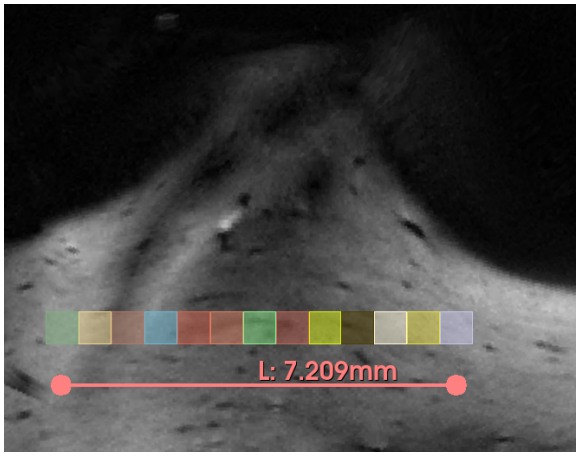

(c) Retardation (60 µm). Line 1.

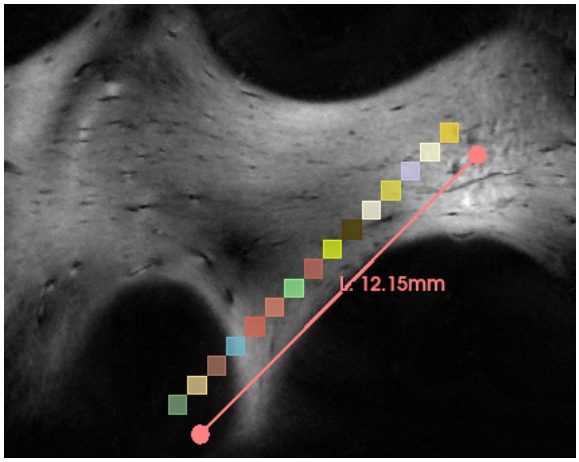

(d) Retardation (60 µm). Line 2.

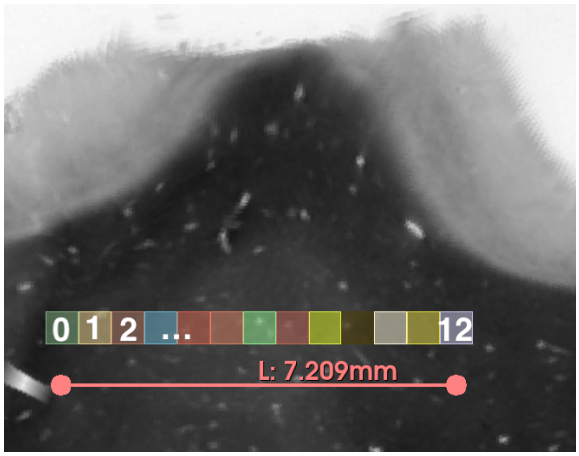

(e) Transmittance (60 µm). Line 1.

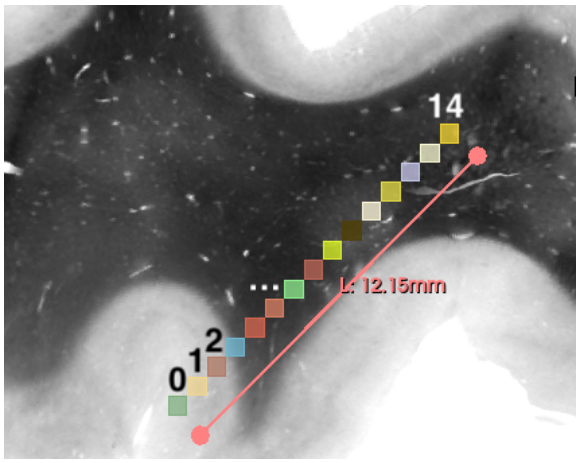

(f) Transmittance (60 µm). Line 2.

Figure 7.17: Line Profile 1 (13 Segments á 0.6 × 0.6 mm^2) and Line Profile 2 (15 Segments á 0.6 × 0.6 mm^2)

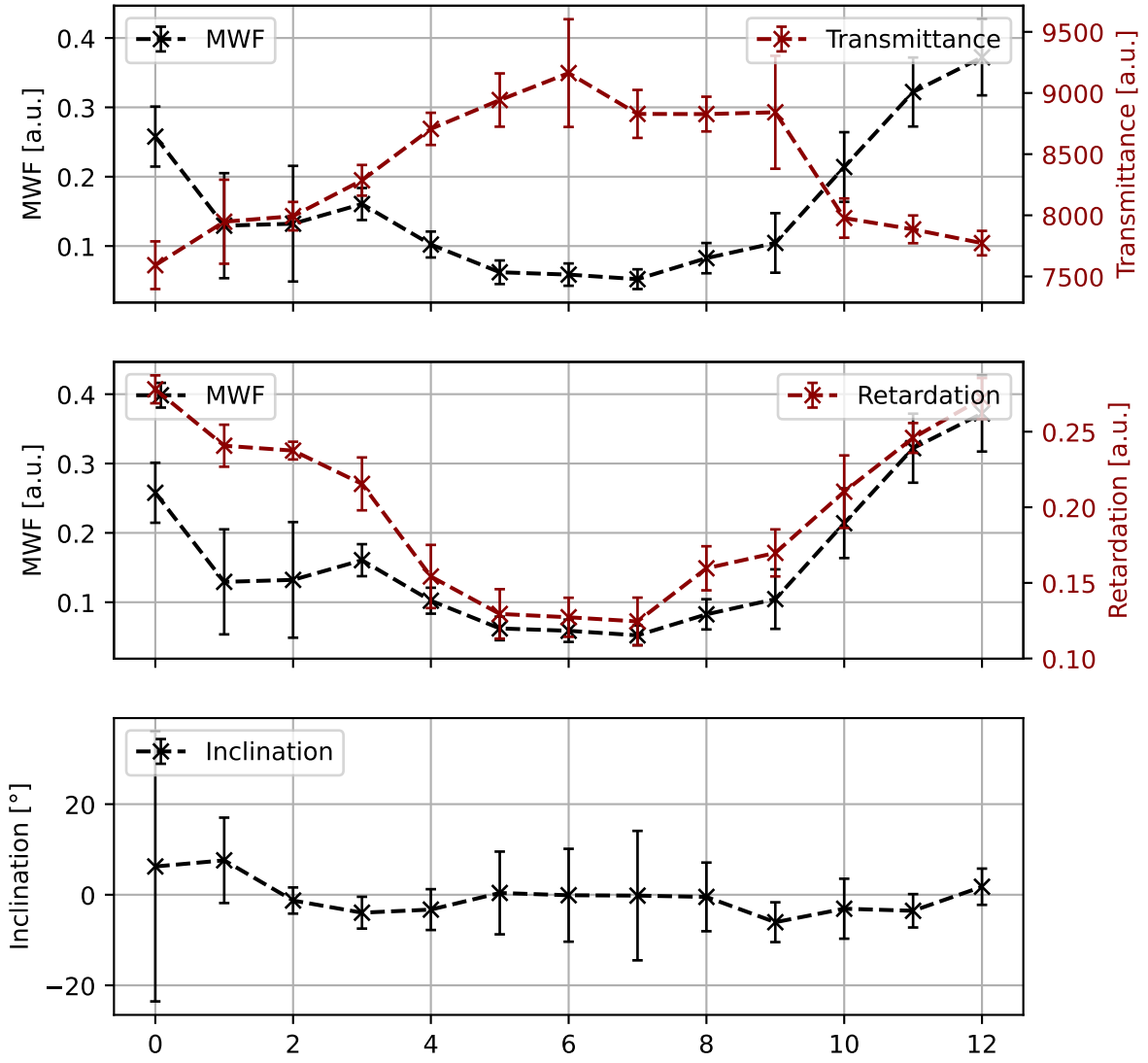

Figure 7.18: Line Profile of Line 1 for MWF, Transmittance, Retardation, and Inclination. MWF is plotted and displayed individually in combination with Transmittance and Retardation for visibility.

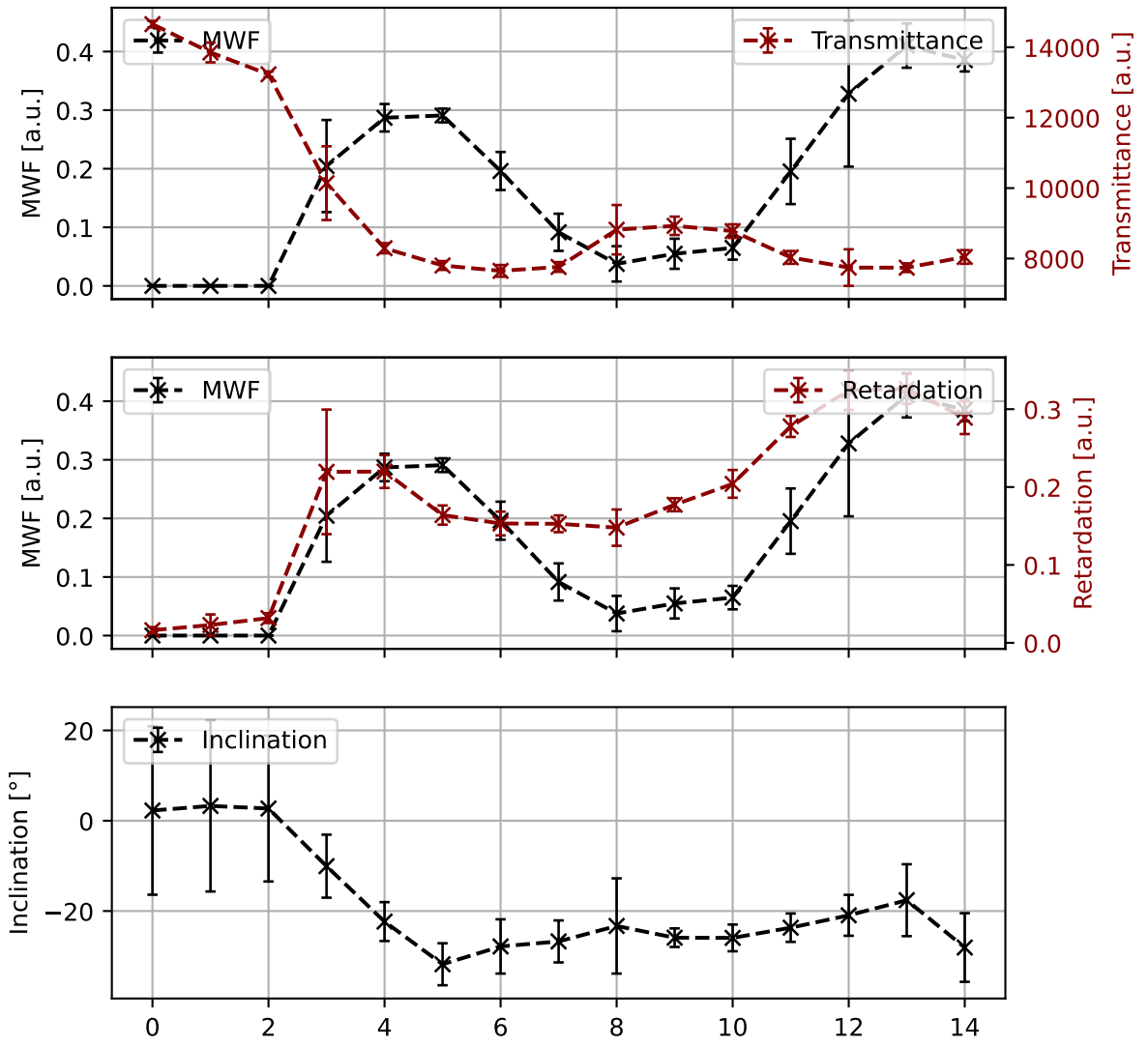

Figure 7.19: Line Profile of Line 2 for MWF, Transmittance, Retardation, and Inclination. MWF is plotted and displayed individually in combination with Transmittance and Retardation for visibility.

7.4 Discussion

In this study 3D-PLI modalities, namely Transmittance, Retardation, rel. Thickness and Inclination were combined and correlated with MWF for the first time. A step-by-step system was laid out consisting of **1.** pre-registering and **2.** registering ROIs of strongly distorted histological sections and **3.** transforming them into registered volumes with the necessary metadata to bridge the gap between the processed sections and already widely used open-source, quantitative image analysis software `3DSlicer` [132] which has been used in this study to perform 3D registration, following segmentation and statistical analysis. This approach dramatically decreased the required development time and kept the number of tools that require *in-house* maintenance low.

The study showed while MWF and rel. Thickness (as well as Retardation if areas with flat fibers are chosen) can correspond linearly, the Transmittance might be a better choice (or rather an additional feature) for classification of low myelinated regions in the WM *if and only if* the Inclination is known and is not a free-moving parameter as in [81]. Since the development of 3D-PLI with oblique views this is guaranteed.

Though this study concentrated on the LAP with a resolution of 60 µm rather than 1.85 µm of the LMP-3D it paves the way for future correlational analysis studies. Still, the tools used in the process, from the finished 3D-PLI workflow results need to be optimized or adjusted to work with Gigapixel 3D-PLI modality maps which is certainly non-trivial. Additionally, for correlational studies of orientations, the reorientation after the registration in 3D has to be integrated [133].

Part V

Overarching Discussion

Chapter 8

Conclusion and Outlook

This work was dedicated to streamlining the data processing and analysis of 3D-PLI imaging, building upon it, and delivering a methodology for performing multimodal correlations scalable to the whole human brain level. A systematic approach to data processing is crucial as the datasets grow in scan size and number and the workflow is getting more complex. All steps must be well-defined, including the registration to Blockface and MRI. Otherwise, the sheer number of scans will become overwhelming, impeding the exploration of relationships in the multi-scale data and hindering the acquisition of new insights.

Conclusion In Part I in chapter 2 a short overview of the neuroanatomic approach to the human brain was given, followed by the explanation in chapter 3 of the underlying birefringence effect and the presentation of the two Polarizing Microscopes developed by the INM-1 or Taorad, the LAP and LMP-3D, which enable imaging with oblique views which enables the reconstruction of the Inclination angle. In chapter 4 the physical model of 3D-PLI was written in a more concise way (which is a small, but first contribution of this thesis) and the up-to-here 3D-PLI analysis was introduced.

In Part II in chapter 5, an automated workflow of 3D-PLI for LAP and LMP-3D was presented. First, synthetic data generation was introduced for fast testing of orientation analysis software, which simplifies future development and maintenance of 3D-PLI analysis software. After this, the minimal workflow of 3D-PLI, from calibration to FOM generation on HPC, was laid out, followed by Multi-GPU parallelization and runtime reduction of the Least Squares Analysis [71, 76] to utilize all available GPUs on the accelerator nodes. Then, the workflow was extended by the incorporation of automatic ICA-based artifact removal, which requires robust mask generation, which was also (*ad hoc*) developed in this thesis. This is the first time that automatic analysis of LAP and LMP-3D on HPC is possible.

In Part III, the uncertainty estimation of fiber orientations [71] reconstructed by 3D-PLI was revisited in chapter 6, implemented on GPU (using the `MOT` library [96]) to reduce runtime (see section 6.3), and was further improved and accelerated by utilizing explainable and physical-inspired machine learning based on General Additive Models (GAMs [109]) in section 6.4. This study was published in [110]. By providing uncertainties to orientations, fiber tractography can get better informed about which pathways are more likely than others. Also, by visualizing certainty and uncertainty by ellipsoids, neuroanatomists studying the parcellation of the brain based on fiber distributions can make more informed decisions.

Finally, in Part IV in chapter 7, correlational analysis between 3D-PLI and MRI was performed. Previous studies only made rough visual comparisons about the myelination of areas made by careful selection and manual alignment of 3D-PLI and stained images. In this study, the whole methodology from registration of certain ROIs using Blockface imaging to the creation of volumes, which are further registered and correlated with MRI, here MWF volumes, was described in detail. First results of the correlation of MWF vs. Retardation and MWF vs. rel. Thickness was given. Supplemented by the discovery that low-myelin areas in the WM indicated by MWF correlate with (local maxima of) the Transmittance.

In fig. 8.1, these three Parts (II to IV), from workflow analysis (**Top**) over uncertainty estimation to multi-modal correlation (**Bottom**), are summarized.

Outlook The presented work can be extended in a number of ways. Regarding Part I, the whole workflow could be automatically tested and deployed on the HPC system via CI/CD [134]. The Least Squares Analysis as well as the MCMC-based uncertainty estimation (Part II) are based on the paradigm of pixel-wise analysis and do not incorporate spatial information of neighboring pixel in the analysis. New machine learning approaches using invertible networks [135] and incorporating attention [136] could be developed to overcome this limitation.

Greater challenges come with the utilization of fiber orientations on the microscale in tractography to overcome the gyral bias [137] or even global tractography in order to overcome the challenges of crossing fiber constellations [138]. As well in multi-modal studies incorporating MRI, TPFM [46], and EM [139], OCT [40] on a larger scale. Here, image registration must be further improved to account for the large deformations often encountered in histological imaging using e.g., polyaffine registration [140] or machine learning [141]. Correlative studies could be automated by extending the clustering studies by machine learning for 3D-PLI [142] into the multimodal domain.

New studies must not only focus on transforming the results and insights of 3D-PLI to other imaging domains and the enhancement of algorithms for analysis but simultaneously try to keep the note of the nested, multi-scaled fiber networks [16] in mind. With the arrival of Exascale Computing, this might be achievable.

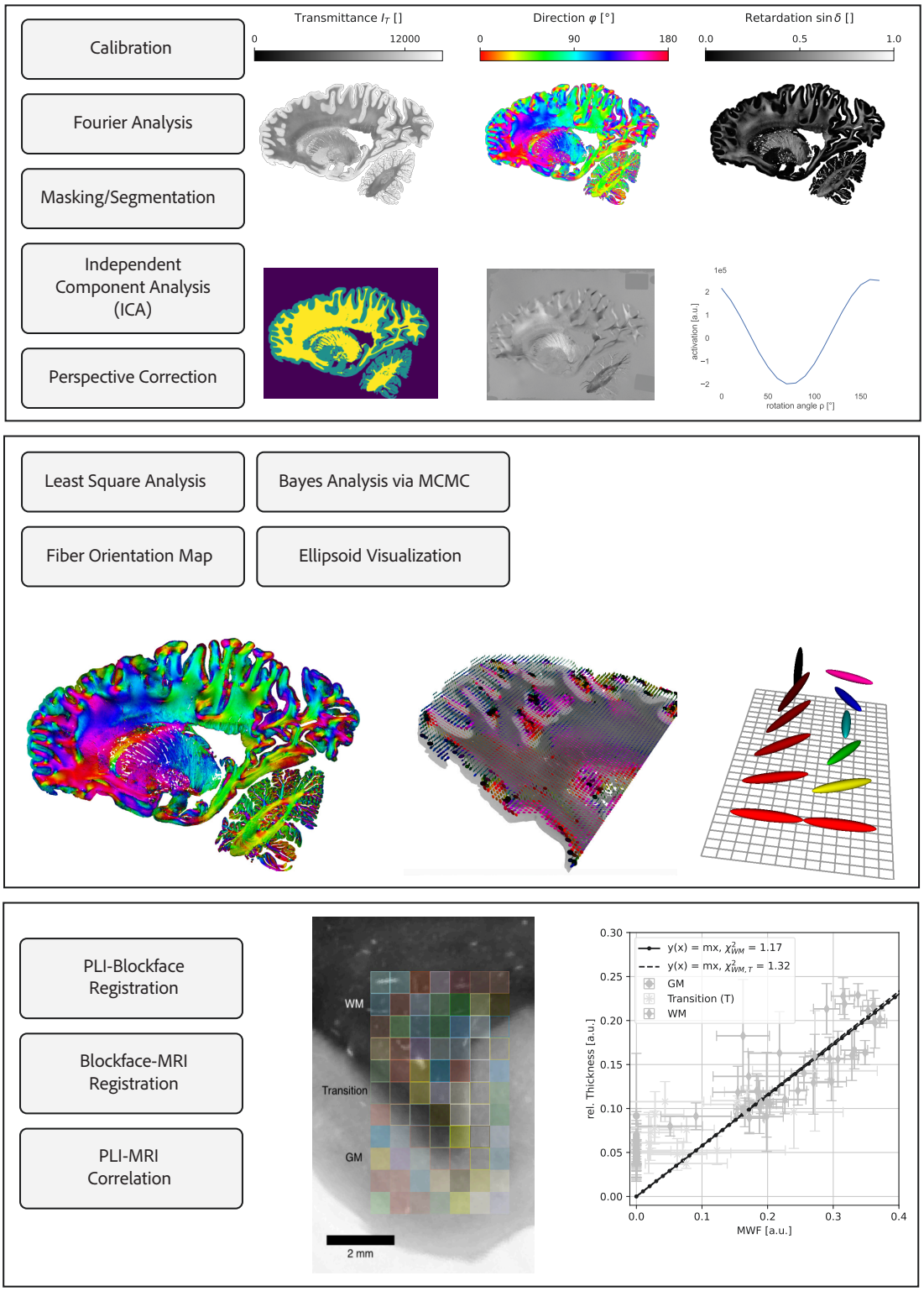

Figure 8.1: Graphical summary of the workflow developed in this thesis, the visualization of the results and the following correlational multimodal analysis.

List of Figures

List of Tables

List of Abbreviations

3D-PLI 3D-Polarized Light Imaging.

BAMBI BAyesian Multivariate Birefringence Inference.

BRIEF Binary Robust Independent Elementary Features.

BSS Blind Source Separation.

CCW Counterclockwise.

CI Credible Interval.

CI/CD Continuous Integration/Continuous Deployment.

CLI Command Line Interface.

CPU Central Processing Unit.

CT Computed Tomography.

CUDA Compute Unified Device Architecture.

CW Clockwise.

dMRI Diffusion Magnetic Resonance Imaging.

DTI Diffusion Tensor Imaging.

DWI Diffusion Weighted Imaging.

EEG Electroencephalography.

FAST Features from Accelerated Segment Test.

FOM Fiber Orientation Map.

GAM General Additive Models.

GCV Generalized cross-validation.

GM Gray Matter.

GPU Graphics Processing Unit.

HDF5 Hierarchical Data Format 5.

HPC High Performance Computing.

HPD Highest Posterior Density.

HPDi Highest Posterior Density interval.

ICA Independent Component Analysis.

INM-1 Institut für Neurowissenschaften und Medizin (INM): Strukturelle und funktionelle Organisation des Gehirns (INM-1).

ITK Insight Toolkit.

IUPAC International Union of Pure and Applied Chemistry.

JURECA Juelich Research and Development Cluster.

JURECA-DC Juelich Research and Development Cluster - Data Centric.

LAP Large Area Polarimeter.

LMP-3D Large Metripol Polarimeter-3D.

MCMC Markov Chain Monte Carlo.

MDT Microstructure Diffusion Toolbox.

MEG Magnetoencephalography.

MOT Multi-threaded Optimization Toolbox.

MPI Message Passing Interface.

MRI Magnetic Resonance Imaging.

MWF Myelin Water Fraction.

OCT Optical Coherence Tomography.

OpenCL Open Computing Language.

ORB Oriented FAST and Rotated BRIEF.

P-IRLS Penalized-Iteratively Reweighted Least-Squares.

PCA Principal Component Analysis.

PLI Polarized Light Imaging.

PM Polarizing Microscope.

RANSAC Random Sample Consensus.

ROFL Robust Orientation Fitting via Least Squares.

ROI Region of Interest.

SyN Symmetric Normalization.

TPFM Two-Photon Fluorescence Microscopy.

VTK Visualization Toolkit.

WM White Matter.

Appendix A

Tissue Preparation and Sectioning

A.1 Amsterdam Brain

Study The images were acquired in tissue awarded to Dr. R.N. Kooijmans under ethics protocol 1037 by the Netherlands Brain Bank.

PLI Preparation The tissue was fixed for 16 weeks in a phosphate-buffered 4% formaldehyde solution. Subsequently, it was washed in running tap water for 1 week, and finally cryoprotected in a 20% glycerin solution, deeply frozen, cut with a large-scale cryostat microtome (Polycut CM 3500, Leica Microsystems, Germany), mounted on glass slides, and stored at -80°C.

A.2 Düsseldorf Brain

Study Study no.: 2023-2636-other research pioneering High-resolution
Multimodal imaging approach to study multisystem atrophy.

(from ger: *Studien-Nr.: 2023-2636-andere Forschung erstvotierend Hochauflösender Multimodaler-Bildgebungsansatz zur Untersuchung der Multisystematrophie.*)

PLI Preparation The examined brain was removed within 24 hours after the donor's death. The right hemisphere was fixed in 4% buffered formaldehyde solution for 15 days to prevent tissue degeneration. After immersion in a 20% solution of glycerin with dimethyl sulfoxide (DMSO) for cryoprotection the brain was frozen at a temperature of -80°C. The sectioning resulted in 843 coronal sections of 70 µm thickness (Polycut CM 3500, Leica, Germany), which is a factor of 3–4 thicker than a brain section suitable for classical histological cell or fiber staining. However, polarization-based imaging imposes no fundamental restriction on using thinner sections, but cryo-sectioning and handling of large-area sections intended to be 3D-reconstructed led to this compromise of section thickness [110].

A.3 Chenonceau Brain

Study A human brain was acquired from the Body Donation program of the Anatomy Laboratory of Tours University (Pr C. Destrieux, Faculty of Medicine, CHU Bretonneau, Tours, France). The sample acquisition and fixation protocol were approved by the French national CODECOH procedure which monitors all manipulations of human samples for research purposes. The donor was a 92-year-old male, with a history of macular degeneration and early stages of cognitive disorders. The sample was extracted with a post-mortem interval (PMI) of 8 hours and the subsequent fixation protocol combined immersion and perfusion of the brain with 4%buffered formalin [Latini et al. 2015]. This process lasted an extended period of 5 months, at a low temperature of 5°C to ensure an optimal fixation of the brain. The brain was then thoroughly washed and immersed in 0.1M phosphate-buffered saline (PBS) for 4 months. This re-hydration stage improved significantly the proton density and T2 recovery [T. M. Shepherd, Thelwall, et al. 2009]. While immersed, the brain was suspended in the fluid, to avoid deformations from the mechanical pressure of the container [143].

PLI Preparation The brain was immersed in a 20% solution of glycerin with dimethyl sulfoxide (DMSO) for cryoprotection and then frozen at a temperature of -80°C. Sectioning was performed with a 50 μm section size (Polycut CM 3500, Leica, Germany).

Appendix B

Specifications of the 3D-PLI systems

	LAP	LMP-3D
Camera	Zeiss Axiocam HRc	SVS vistek evo4070 GigE
Sensorpixel	2776 x 2080	2048 x 2048
Pixel size	40 µm, 60 µm	1.85 µm
Light Source	(525 ±25) nm	520 nm
Wavelength Filter	—	(532 ±10) nm
Pol-Filters	• LinPol • Ret [568 nm] • LinPol • (large, "low-quality", all separately rotatable)	• LinPol [rotatable] • Ret [532 nm] +LinPol [fix] • ("high-quality")
Stage	no x/y-movement	motorized x/y stage (each tile: 3.8 mm x 3.8 mm)
Scantime	15 min	6 h
Datasize	2 GB	up to 600 GB
Oblique views	4	4
Oblique angle	8.0°	3.9° (by 2.5 mm shifted aperture)
Objective lens	camera objective lens: f=50 mm	microscope objective lens: Nikon 4x, NA0.2 (+ TubeLens)

Appendix C

Mathematica notebook of the derivation of Direction and Retardation under oblique views.

Definition of the PLI fiber vector.

In[4]:=
```
fiberVec[ϕ_, α_] = {Cos[α] Cos[ϕ], Cos[α] Sin[ϕ], Sin[α]};
Print[MatrixForm[fiberVec[ϕ, α]]];
```

$$\begin{pmatrix} \text{Cos}[\alpha]\,\text{Cos}[\phi] \\ \text{Cos}[\alpha]\,\text{Sin}[\phi] \\ \text{Sin}[\alpha] \end{pmatrix}$$

Definition of the rotation matrices of the tilting stage.

In[6]:=
```
Print[MatrixForm[RotationMatrix[ψ, {0, 0, 1}]]]
Print[MatrixForm[RotationMatrix[τ, {0, 1, 0}]]]
Print[MatrixForm[RotationMatrix[-ψ, {0, 0, 1}]]]
```

$$\begin{pmatrix} \text{Cos}[\psi] & -\text{Sin}[\psi] & 0 \\ \text{Sin}[\psi] & \text{Cos}[\psi] & 0 \\ 0 & 0 & 1 \end{pmatrix}$$

$$\begin{pmatrix} \text{Cos}[\tau] & 0 & \text{Sin}[\tau] \\ 0 & 1 & 0 \\ -\text{Sin}[\tau] & 0 & \text{Cos}[\tau] \end{pmatrix}$$

$$\begin{pmatrix} \text{Cos}[\psi] & \text{Sin}[\psi] & 0 \\ -\text{Sin}[\psi] & \text{Cos}[\psi] & 0 \\ 0 & 0 & 1 \end{pmatrix}$$

Composition of the rotation matrices.

In[9]:=
```
PliRotationMatrix[τ_, ψ_] = RotationMatrix[ψ, {0, 0, 1}].
   RotationMatrix[τ, {0, 1, 0}].RotationMatrix[-ψ, {0, 0, 1}];
```

Tilting matrix.

In[10]:=
```
Print[MatrixForm[PliRotationMatrix[τ_, ψ_]]];
```

$$\begin{pmatrix} \text{Cos}[\tau_]\,\text{Cos}[\psi_]^2 + \text{Sin}[\psi_]^2 & -\text{Cos}[\psi_]\,\text{Sin}[\psi_] + \text{Cos}[\tau_]\,\text{Cos}[\psi_]\,\text{Sin}[\psi_] & \text{Cos}[\\ -\text{Cos}[\psi_]\,\text{Sin}[\psi_] + \text{Cos}[\tau_]\,\text{Cos}[\psi_]\,\text{Sin}[\psi_] & \text{Cos}[\psi_]^2 + \text{Cos}[\tau_]\,\text{Sin}[\psi_]^2 & \text{Sin}[\\ -\text{Cos}[\psi_]\,\text{Sin}[\tau_] & -\text{Sin}[\tau_]\,\text{Sin}[\psi_] & \end{pmatrix}$$

Definition of the fiber tilting process.

In[11]:=
```
tiltedFiberParams[ϕ_, α_, t_, τ_, ψ_] =
  Module[{rotFiber, newInclination, newDirection, newTrel},
    rotFiber = PliRotationMatrix[τ, ψ] . fiberVec[ϕ, α];
    newDirection = FullSimplify[ArcTan[rotFiber[[1]], rotFiber[[2
      ]]]];
    newInclination = FullSimplify[ArcSin[rotFiber[[3]]]];
    newTrel = FullSimplify[t / Cos[τ]];
    {newDirection, newInclination, newTrel}
  ];
```

Obtaining the formula for the tilted Direction.

In[12]:=
```
Print[tiltedFiberParams[ϕ, α, t, τ, ψ][[1]]];
```

$$\text{ArcTan}\Big[\text{Cos}[\psi]\,\text{Sin}[\alpha]\,\text{Sin}[\tau] - 2\,\text{Cos}[\alpha]\,\text{Cos}[\psi]\,\text{Sin}\Big[\frac{\tau}{2}\Big]^2\,\text{Sin}[\phi]\,\text{Sin}[\psi] + \text{Cos}[\alpha]\,\text{Cos}[\phi]\,\left(\text{Cos}[\tau]\,\text{Cos}[\psi]^2 + \text{Sin}[\psi]^2\right),\ \text{Sin}[\alpha]\,\text{Sin}[\tau]\,\text{Sin}[\psi] + \text{Cos}[\alpha]\,\left(\text{Cos}[\psi]\,\text{Sin}[\phi - \psi] + \text{Cos}[\tau]\,\text{Cos}[\phi - \psi]\,\text{Sin}[\psi]\right)\Big]$$

Obtaining the formula for the tilted Inclination.

In[13]:=
```
Print[tiltedFiberParams[ϕ, α, t, τ, ψ][[2]]];
```

```
ArcSin[Cos[τ] Sin[α] - Cos[α] Cos[ϕ - ψ] Sin[τ]]
```

Inserting the formula for the tilted Inclination into the formula of the retardation.

In[14]:=
```
Print[π / 2 * t * Cos[tiltedFiberParams[ϕ, α, t, τ, ψ][[2]]] ^ 2];
```

$$\frac{1}{2}\,\pi\,\mathtt{t}\,\left(1-\left(\mathtt{Cos}[\tau]\,\mathtt{Sin}[\alpha]-\mathtt{Cos}[\alpha]\,\mathtt{Cos}[\phi-\psi]\,\mathtt{Sin}[\tau]\right)^2\right)$$

Appendix D

CPU and GPU node specification of the JURECA DC Module (Phase 2: as of May 2021)[1]

- CPU node (480 available)
  - 2× AMD EPYC 7742, 2× 64 cores, 2.25 GHz
  - 512 (16× 32) GB DDR4, 3200 MHz
  - InfiniBand HDR100 (NVIDIA Mellanox Connect-X6)
- GPU node (192 available)
  - 2 × AMD EPYC 7742, 2× 64 cores, 2.25 GHz
  - 512 (16× 32) GB DDR4, 3200 MHz
  - 4× NVIDIA A100 GPU, 4× 40 GB HBM2e
  - 2× InfiniBand HDR (NVIDIA Mellanox Connect-X6)

[1] `https://apps.fz-juelich.de/jsc/hps/jureca/configuration.html` (Retrieved: 29. April 2024)

Bibliography

[1] Frederico A.C. Azevedo et al. "Equal Numbers of Neuronal and Nonneuronal Cells Make the Human Brain an Isometrically Scaled-up Primate Brain". In: *Journal of Comparative Neurology* 513.5 (Apr. 10, 2009), pp. 532–541. ISSN: 0021-9967, 1096-9861. DOI: 10.1002/cne.21974.

[2] Jiawei Zhang. *Basic Neural Units of the Brain: Neurons, Synapses and Action Potential*. May 30, 2019. arXiv: 1906.01703 [q-bio]. URL: http://arxiv.org/abs/1906.01703 (visited on 03/16/2024). Pre-published.

[3] Olaf Sporns, Giulio Tononi, and Rolf Kötter. "The Human Connectome: A Structural Description of the Human Brain". In: *PLoS Computational Biology* 1.4 (2005), e42. ISSN: 1553-734X, 1553-7358. DOI: 10.1371/journal.pcbi.0010042.

[4] Christian Otte et al. "Major Depressive Disorder". In: *Nature Reviews Disease Primers* 2.1 (Sept. 15, 2016), p. 16065. ISSN: 2056-676X. DOI: 10.1038/nrdp.2016.65.

[5] Seth A. Gale, Diler Acar, and Kirk R. Daffner. "Dementia". In: *The American Journal of Medicine* 131.10 (Oct. 2018), pp. 1161–1169. ISSN: 00029343. DOI: 10.1016/j.amjmed.2018.01.022.

[6] Philip Scheltens et al. "Alzheimer's Disease". In: *The Lancet* 397.10284 (Apr. 2021), pp. 1577–1590. ISSN: 01406736. DOI: 10.1016/S0140-6736(20)32205-4.

[7] Hui Ye et al. "Genetics and Pathogenesis of Parkinson's Syndrome". In: *Annual Review of Pathology: Mechanisms of Disease* 18.1 (Jan. 24, 2023), pp. 95–121. ISSN: 1553-4006, 1553-4014. DOI: 10.1146/annurev-pathmechdis-031521-034145.

[8] E. Ray Dorsey et al. "The Emerging Evidence of the Parkinson Pandemic". In: *Journal of Parkinson's Disease* 8.s1 (Dec. 18, 2018). Ed. by Patrik Brundin, J. William Langston, and Bastiaan R. Bloem, S3–S8. ISSN: 18777171, 1877718X. DOI: 10.3233/JPD-181474.

[9] Stephen L. Hauser and Bruce A.C. Cree. "Treatment of Multiple Sclerosis: A Review". In: *The American Journal of Medicine* 133.12 (Dec. 2020), 1380–1390.e2. ISSN: 00029343. DOI: 10.1016/j.amjmed.2020.05.049.

[10] Stephen D Silberstein. "Migraine". In: *The Lancet* 363.9406 (Jan. 2004), pp. 381–391. ISSN: 01406736. DOI: 10.1016/S0140-6736(04)15440-8.

[11] Katrin Amunts et al. "The Coming Decade of Digital Brain Research: A Vision for Neuroscience at the Intersection of Technology and Computing". In: *Imaging Neuroscience* (Apr. 2, 2024). ISSN: 2837-6056. DOI: 10.1162/imag_a_00137.

[12] A. Paul Alivisatos et al. "The Brain Activity Map". In: *Science* 339.6125 (Mar. 15, 2013), pp. 1284–1285. ISSN: 0036-8075, 1095-9203. DOI: 10.1126/science.1236939.

[13] Markus Axer et al. "A Novel Approach to the Human Connectome: Ultra-high Resolution Mapping of Fiber Tracts in the Brain". In: *NeuroImage* 54.2 (Jan. 2011), pp. 1091–1101. ISSN: 10538119. DOI: 10.1016/j.neuroimage.2010.08.075.

[14] Markus Axer et al. "High-Resolution Fiber Tract Reconstruction in the Human Brain by Means of Three-Dimensional Polarized Light Imaging". In: *Frontiers in Neuroinformatics* 5 (2011). ISSN: 1662-5196. DOI: 10.3389/fninf.2011.00034.

[15] Svenja Caspers and Markus Axer. "Decoding the Microstructural Correlate of Diffusion MRI". In: *NMR in Biomedicine* 32.4 (Apr. 2019), e3779. ISSN: 0952-3480, 1099-1492. DOI: 10.1002/nbm.3779.

[16] Markus Axer and Katrin Amunts. "Scale Matters: The Nested Human Connectome". In: *Science* 378.6619 (Nov. 4, 2022), pp. 500–504. ISSN: 0036-8075, 1095-9203. DOI: 10.1126/science.abq2599.

[17] Martin Stacho et al. "A Cortex-like Canonical Circuit in the Avian Forebrain". In: *Science* 369.6511 (Sept. 25, 2020), eabc5534. ISSN: 0036-8075, 1095-9203. DOI: 10.1126/science.abc5534.

[18] Karl Zilles. "Brodmann: A Pioneer of Human Brain Mapping—His Impact on Concepts of Cortical Organization". In: *Brain* 141.11 (Nov. 1, 2018), pp. 3262–3278. ISSN: 0006-8950, 1460-2156. DOI: 10.1093/brain/awy273.

[19] Katrin Amunts et al. "Broca's Region Revisited: Cytoarchitecture and Intersubject Variability". In: *The Journal of Comparative Neurology* 412.2 (Sept. 20, 1999), pp. 319–341. ISSN: 0021-9967, 1096-9861. DOI: 10.1002/(SICI)1096-9861(19990920)412:2<319::AID-CNE10>3.0.CO;2-7.

[20] Suraj Thulung et al. "Morphometric Measurement of Cranial Vault Thickness: A Tertiary Hospital Based Study". In: *Journal of Nepal Medical Association* 57.215 (Feb. 28, 2019). ISSN: 1815-672X, 0028-2715. DOI: 10.31729/jnma.3949.

[21] Henry Gray, Peter Llewellyn Williams, and Roger Warwick. *Anatomy: Ed. by Peter L[Lewellyn] Williams & Roger Warwick*. 36. ed. Edinburgh [usw.]: Livingstone, 1980. 1578 pp. ISBN: 978-0-443-01505-2.

[22] P. Hartmann et al. "Das Normgewicht Des Gehirns Beim Erwachsenen in Abhängigkeit von Alter, Geschlecht, Körpergröße Und Gewicht". In: *Der Pathologe* 15.3 (June 1, 1994), pp. 165–170. ISSN: 0172-8113, 1432-1963. DOI: 10.1007/s002920050040.

[23] Kelly P. Cosgrove, Carolyn M. Mazure, and Julie K. Staley. "Evolving Knowledge of Sex Differences in Brain Structure, Function, and Chemistry". In: *Biological Psychiatry* 62.8 (Oct. 2007), pp. 847–855. ISSN: 00063223. DOI: 10.1016/j.biopsych.2007.03.001.

[24] Stanley Finger. *Minds Behind the Brain*. Oxford University Press, Mar. 3, 2005. ISBN: 978-0-19-518182-1. DOI: 10.1093/acprof:oso/9780195181821.001.0001.

[25] Dale Purves and Stephen Mark Williams, eds. *Neuroscience*. 2. ed. Sunderland, Mass: Sinauer Associates, 2001. ISBN: 978-0-87893-742-4 978-0-87893-917-6 978-0-87893-740-0.

[26] Mohanlall Narine and Holly Colognato. "Current Insights Into Oligodendrocyte Metabolism and Its Power to Sculpt the Myelin Landscape". In: *Frontiers in Cellular Neuroscience* 16 (Apr. 28, 2022), p. 892968. ISSN: 1662-5102. DOI: 10.3389/fncel.2022.892968.

[27] Paul Broca. "Sur le siège de la faculté du langage articulé". In: *Bulletins de la Société d'anthropologie de Paris* 6.1 (1865), pp. 377–393. ISSN: 0301-8644. DOI: 10.3406/bmsap.1865.9495.

[28] Korbinian Brodmann. *Vergleichende Lokalisationslehre Der Grosshirnrinde: In Ihren Prinzipien Dargestellt Auf Grund d. Zellenbaues*. Repr. d. 1. Aufl. von 1909. Leipzig: Barth, 1985. 335 pp. ISBN: 978-3-335-00010-5.

[29] Per E. Roland and Karl Zilles. "Structural Divisions and Functional Fields in the Human Cerebral cortex1Published on the World Wide Web on 20 February 1998.1". In: *Brain Research Reviews* 26.2-3 (May 1998), pp. 87–105. ISSN: 01650173. DOI: 10.1016/S0165-0173(97)00058-1.

[30] John C. Mazziotta and Toga, Arthur W. *Brain Mapping: The Methods*. Academic Press, 2002. ISBN: 978-1-281-03738-1.

[31] Simon B. Eickhoff et al. "A New SPM Toolbox for Combining Probabilistic Cytoarchitectonic Maps and Functional Imaging Data". In: *NeuroImage* 25.4 (May 2005), pp. 1325–1335. ISSN: 10538119. DOI: 10.1016/j.neuroimage.2004.12.034.

[32] A. Schleicher et al. "Observer-Independent Method for Microstructural Parcellation of Cerebral Cortex: A Quantitative Approach to Cytoarchitectonics". In: *NeuroImage* 9.1 (Jan. 1999), pp. 165–177. ISSN: 10538119. DOI: 10.1006/nimg.1998.0385.

[33] Nathan Blanke et al. "Quantitative Birefringence Microscopy for Imaging the Structural Integrity of CNS Myelin Following Circumscribed Cortical Injury in the Rhesus Monkey". In: *Neurophotonics* 8.01 (Mar. 22, 2021). ISSN: 2329-423X. DOI: 10.1117/1.NPh.8.1.015010.

[34] A. F. Huxley and R. Stämpeli. "Evidence for Saltatory Conduction in Peripheral Myelinated Nerve Fibres". In: *The Journal of Physiology* 108.3 (May 15, 1949), pp. 315–339. ISSN: 0022-3751, 1469-7793. DOI: 10.1113/jphysiol.1949.sp004335.

[35] E. Leray et al. "Epidemiology of Multiple Sclerosis". In: *Revue Neurologique* 172.1 (Jan. 2016), pp. 3–13. ISSN: 00353787. DOI: 10.1016/j.neurol.2015.10.006.

[36] Vinit Baliyan et al. "Diffusion Weighted Imaging: Technique and Applications". In: *World Journal of Radiology* 8.9 (2016), p. 785. ISSN: 1949-8470. DOI: 10.4329/wjr.v8.i9.785.

[37] Chantal M.W. Tax et al. "What's New and What's next in Diffusion MRI Preprocessing". In: *NeuroImage* 249 (Apr. 2022), p. 118830. ISSN: 10538119. DOI: 10.1016/j.neuroimage.2021.118830.

[38] Justine Beaujoin et al. "Post-Mortem Inference of the Human Hippocampal Connectivity and Microstructure Using Ultra-High Field Diffusion MRI at 11.7 T". In: *Brain Structure and Function* 223.5 (June 2018), pp. 2157–2179. ISSN: 1863-2653, 1863-2661. DOI: 10.1007/s00429-018-1617-1.

[39] Daniel C. Alexander et al. "Imaging Brain Microstructure with Diffusion MRI: Practicality and Applications". In: *NMR in Biomedicine* 32.4 (Apr. 2019). ISSN: 0952-3480, 1099-1492. DOI: 10.1002/nbm.3841.

[40] Hui Wang et al. "As-PSOCT: Volumetric Microscopic Imaging of Human Brain Architecture and Connectivity". In: *NeuroImage* 165 (Jan. 2018), pp. 56–68. ISSN: 10538119. DOI: 10.1016/j.neuroimage.2017.10.012.

[41] Ludovico Silvestri et al. "Correlative Two-Photon and Light Sheet Microscopy". In: *Methods* 66.2 (Mar. 2014), pp. 268–272. ISSN: 10462023. DOI: 10.1016/j.ymeth.2013.06.013.

[42] Karel Svoboda and Ryohei Yasuda. "Principles of Two-Photon Excitation Microscopy and Its Applications to Neuroscience". In: *Neuron* 50.6 (June 2006), pp. 823–839. ISSN: 08966273. DOI: 10.1016/j.neuron.2006.05.019.

[43] Stephen P. Amato et al. "Whole Brain Imaging with Serial Two-Photon Tomography". In: *Frontiers in Neuroanatomy* 10 (Mar. 22, 2016). ISSN: 1662-5129. DOI: 10.3389/fnana.2016.00031.

[44] David Grant Colburn Hildebrand et al. "Whole-Brain Serial-Section Electron Microscopy in Larval Zebrafish". In: *Nature* 545.7654 (May 2017), pp. 345–349. ISSN: 0028-0836, 1476-4687. DOI: 10.1038/nature22356.

[45] Sahil Loomba et al. "Connectomic Comparison of Mouse and Human Cortex". In: *Science* 377.6602 (July 8, 2022), eabo0924. ISSN: 0036-8075, 1095-9203. DOI: 10.1126/science.abo0924.

[46] Irene Costantini et al. “Combination of Two-Photon Fluorescence Microscopy and Label-Free near-Infrared Reflectance: A New Complementary Approach for Brain Imaging”. In: *Biomedical Optics 2016*. Cancer Imaging and Therapy. Fort Lauderdale, Florida: OSA, 2016, JW3A.23. ISBN: 978-1-943580-10-1. DOI: 10.1364/CANCER.2016.JW3A.23.

[47] Katrin Amunts et al. “Linking Brain Structure, Activity, and Cognitive Function through Computation”. In: *eneuro* 9.2 (Mar. 2022), ENEURO.0316–21.2022. ISSN: 2373-2822. DOI: 10.1523/ENEURO.0316-21.2022.

[48] Daniel Liewald et al. “Distribution of Axon Diameters in Cortical White Matter: An Electron-Microscopic Study on Three Human Brains and a Macaque”. In: *Biological Cybernetics* 108.5 (Oct. 2014), pp. 541–557. ISSN: 0340-1200, 1432-0770. DOI: 10.1007/s00422-014-0626-2.

[49] Kathleen S. Rockland. “What We Can Learn from the Complex Architecture of Single Axons”. In: *Brain Structure and Function* 225.4 (May 2020), pp. 1327–1347. ISSN: 1863-2653, 1863-2661. DOI: 10.1007/s00429-019-02023-3.

[50] Benjamin Danner et al. “Brain Banking in the United States and Europe: Importance, Challenges, and Future Trends”. In: *Journal of Neuropathology & Experimental Neurology* 83.4 (Mar. 20, 2024), pp. 219–229. ISSN: 0022-3069, 1554-6578. DOI: 10.1093/jnen/nlae014.

[51] Rooban Thavarajah et al. “Chemical and Physical Basics of Routine Formaldehyde Fixation”. In: *Journal of Oral and Maxillofacial Pathology* 16.3 (2012), p. 400. ISSN: 0973-029X. DOI: 10.4103/0973-029X.102496.

[52] Kodela Vani, Steven A. Bogen, and Seshi R. Sompuram. “A High Throughput Combinatorial Library Technique for Identifying Formalin-Sensitive Epitopes”. In: *Journal of Immunological Methods* 317.1-2 (Dec. 2006), pp. 80–89. ISSN: 00221759. DOI: 10.1016/j.jim.2006.09.009.

[53] Nicole Schubert et al. “3D Polarized Light Imaging Portrayed: Visualization of Fiber Architecture Derived from 3D-PLI”. In: *High-Resolution Neuroimaging - Basic Physical Principles and Clinical Applications*. Ed. by Ahmet Mesrur Halefoğlu. InTech, Mar. 14, 2018. ISBN: 978-953-51-3865-5. DOI: 10.5772/intechopen.72532.

[54] Richard S. Bear and Francis O. Schmitt. “The Optics of Nerve Myelin”. In: *Journal of the Optical Society of America* 26.5 (May 1, 1936), p. 206. ISSN: 0030-3941. DOI: 10.1364/JOSA.26.000206.

[55] John David Jackson. *Klassische Elektrodynamik:* DE GRUYTER, Dec. 12, 2013. ISBN: 978-3-11-033446-3. DOI: 10.1515/9783110334470.

[56] Daniel Schmitz. “Reconstruction of Three-Dimensional Nerve Fiber Orientations from Histological Brain Sections in Three-Dimensional Polarized Light Imaging”. PhD thesis. Bergische Universität Wuppertal, 2020, 150 p.

[57] Francis O. Schmitt and Richard S. Bear. “THE ULTRASTRUCTURE OF THE NERVE AXON SHEATH”. In: *Biological Reviews* 14.1 (Jan. 1939), pp. 27–50. ISSN: 1464-7931, 1469-185X. DOI: 10.1111/j.1469-185X.1939.tb00922.x.

[58] G.F. Göthlin. “Die Doppelbrechenden Eigenschaften Des Nervengewebes, Ihre Ursachen Und Ihre Biologischen Konsequenzen: Mit 3 Taf. Und 1 Fig. Im Texte”. In: *Kungliga Svenska Vetenskapsakademiens Handlingar* 51.1 (1913).

[59] Nirmalya Ghosh. “Tissue Polarimetry: Concepts, Challenges, Applications, and Outlook”. In: *Journal of Biomedical Optics* 16.11 (Nov. 1, 2011), p. 110801. ISSN: 1083-3668. DOI: 10.1117/1.3652896.

[60] Hendrik Wiese. “Enhancing the Signal Interpretation and Microscopical Hardware Concept of 3D Polarized Light Imaging”. PhD thesis. Bergische Universität Wuppertal, 2016, 145 p.

[61] Miriam Menzel. *Finite-Difference Time-Domain Simulations Assisting to Reconstruct the Brain's Nerve Fiber Architecture by 3D Polarized Light Imaging*. Vol. RWTH Aachen University. RWTH Aachen University, 2018, pages ix, 296 S. DOI: 10.18154/RWTH-2018-230974.

[62] David Brewster. *A Treatise on the Microscope : Forming the Article under That Head in the Seventh Edition of the Encyclopaedia Britannica*. Medical Heritage Library. Edinburgh: A. and C. Black, 1837. 193 pp.

[63] H.F. Talbot. "XLIV. *Experiments on Light*". In: *The London, Edinburgh, and Dublin Philosophical Magazine and Journal of Science* 5.29 (Nov. 1834), pp. 321–334. ISSN: 1941-5966, 1941-5974. DOI: 10.1080/14786443408648474.

[64] Bernardo Cesare, Nicola Campomenosi, and Michael Shribak. "Polychromatic Polarization: Boosting the Capabilities of the Good Old Petrographic Microscope". In: *Geology* 50.2 (Feb. 1, 2022), pp. 137–141. ISSN: 0091-7613, 1943-2682. DOI: 10.1130/G49303.1.

[65] Tatiana Novikova et al. "Mueller Polarimetry of Brain Tissues". In: *Polarized Light in Biomedical Imaging and Sensing*. Ed. by Jessica C. Ramella-Roman and Tatiana Novikova. Cham: Springer International Publishing, 2023, pp. 205–229. ISBN: 978-3-031-04740-4. DOI: 10.1007/978-3-031-04741-1_8.

[66] Hui Wang et al. "Polarization Sensitive Optical Coherence Microscopy for Brain Imaging". In: *Optics Letters* 41.10 (May 15, 2016), p. 2213. ISSN: 0146-9592, 1539-4794. DOI: 10.1364/OL.41.002213.

[67] Karl Zilles et al. "High-Resolution Fiber and Fiber Tract Imaging Using Polarized Light Microscopy in the Human, Monkey, Rat, and Mouse Brain". In: *Axons and Brain Architecture*. Elsevier, 2016, pp. 369–389. ISBN: 978-0-12-801393-9. DOI: 10.1016/B978-0-12-801393-9.00018-9.

[68] Philipp Thörnig. "JURECA: Data Centric and Booster Modules Implementing the Modular Supercomputing Architecture at Jülich Supercomputing Centre". In: *Journal of large-scale research facilities JLSRF* 7 (Oct. 29, 2021), A182. ISSN: 2364-091X. DOI: 10.17815/jlsrf-7-182.

[69] Hans Müller. "Memorandum on the Polarization Optics of the Photo-Elestic Shutter". In: Report No. 2 of the OSRD project OEMsr-576 (1943).

[70] R. Clark Jones. "A New Calculus for the Treatment of Optical SystemsI. Description and Discussion of the Calculus". In: *Journal of The Optical Society of America* 31.7 (July 1941), pp. 488–493. DOI: 10.1364/JOSA.31.000488.

[71] Daniel Schmitz et al. "Derivation of Fiber Orientations From Oblique Views Through Human Brain Sections in 3D-Polarized Light Imaging". In: *Frontiers in Neuroanatomy* 12 (Sept. 27, 2018), p. 75. ISSN: 1662-5129. DOI: 10.3389/fnana.2018.00075.

[72] Benedicto De Campos Vidal et al. "Anisotropic Properties of the Myelin Sheath". In: *Acta Histochemica* 66.1 (Jan. 1980), pp. 32–39. ISSN: 00651281. DOI: 10.1016/S0065-1281(80)80079-1.

[73] F Bryant. "Snell's Law of Refraction". In: *Physics Bulletin* 9.12 (Dec. 1958), pp. 317–317. ISSN: 0031-9112. DOI: 10.1088/0031-9112/9/12/004.

[74] Siu Kwan Lam, Antoine Pitrou, and Stanley Seibert. "Numba: A LLVM-based Python JIT Compiler". In: *Proceedings of the Second Workshop on the LLVM Compiler Infrastructure in HPC*. SC15: The International Conference for High Performance Computing, Networking, Storage and Analysis. Austin Texas: ACM, Nov. 15, 2015, pp. 1–6. ISBN: 978-1-4503-4005-2. DOI: 10.1145/2833157.2833162.

[75] Lisandro Dalcin and Yao-Lung L. Fang. "Mpi4py: Status Update After 12 Years of Development". In: *Computing in Science & Engineering* 23.4 (July 1, 2021), pp. 47–54. ISSN: 1521-9615, 1558-366X. DOI: 10.1109/MCSE.2021.3083216.

[76] *Nvidia-Gtc19-Dc-Poster-Resizing-Web-1920x1607-JanOliver-Kropp.Jpg (1920×1607)*. URL: https://www.nvidia.com/content/dam/en-zz/Solutions/gtc/conference-posters/nvidia-gtc19-dc-poster-resizing-web-1920x1607-JanOliver-Kropp.jpg (visited on 02/18/2022).

[77] Adrian Przybylski et al. "Gpufit: An Open-Source Toolkit for GPU-accelerated Curve Fitting". In: *Scientific Reports* 7.1 (Nov. 16, 2017), p. 15722. ISSN: 2045-2322. DOI: 10.1038/s41598-017-15313-9.

[78] The HDF Group. *Hierarchical Data Format, Version 5*. 1997–2023.

[79] Charles R. Harris et al. "Array Programming with NumPy". In: *Nature* 585.7825 (Sept. 17, 2020), pp. 357–362. ISSN: 0028-0836, 1476-4687. DOI: 10.1038/s41586-020-2649-2.

[80] Irene Costantini et al. "Autofluorescence Enhancement for Label-Free Imaging of Myelinated Fibers in Mammalian Brains". In: *Scientific Reports* 11.1 (Apr. 13, 2021), p. 8038. ISSN: 2045-2322. DOI: 10.1038/s41598-021-86092-7.

[81] Miriam Menzel et al. "Automated Computation of Nerve Fibre Inclinations from 3D Polarised Light Imaging Measurements of Brain Tissue". In: *Scientific Reports* 12.1 (Mar. 14, 2022), p. 4328. ISSN: 2045-2322. DOI: 10.1038/s41598-022-08140-0.

[82] G. Bradski. "The OpenCV Library". In: *Dr. Dobb's Journal of Software Tools* (2000).

[83] Martin A. Fischler and Robert C. Bolles. "Random Sample Consensus: A Paradigm for Model Fitting with Applications to Image Analysis and Automated Cartography". In: *Communications of the ACM* 24.6 (June 1981), pp. 381–395. ISSN: 0001-0782, 1557-7317. DOI: 10.1145/358669.358692.

[84] Rafael C. Gonzalez and Richard E. Woods. *Digital Image Processing*. Fourth edition, global edition. New York, NY: Pearson, 2018. 1019 pp. ISBN: 978-1-292-22304-9.

[85] Daniel Schmitz et al. "Quantification of Fiber Orientation Uncertainty in Polarized Light Imaging of the Human Brain". In: *Medical Imaging 2020: Physics of Medical Imaging*. Physics of Medical Imaging. Ed. by Hilde Bosmans and Guang-Hong Chen. Houston, United States: SPIE, Mar. 16, 2020, p. 117. DOI: 10.1117/12.2548935.

[86] Kai Benning et al. "Independent Component Analysis for Noise and Artifact Removal in Three-dimensional Polarized Light Imaging". Nov. 30, 2020. arXiv: 2011.14786 [physics].

[87] Jürgen Dammers et al. "Signal Enhancement in Polarized Light Imaging by Means of Independent Component Analysis". In: *NeuroImage* 49.2 (Jan. 2010), pp. 1241–1248. ISSN: 10538119. DOI: 10.1016/j.neuroimage.2009.08.059.

[88] Lukas Breuer, Markus Axer, and Jürgen Dammers. "A New Constrained ICA Approach for Optimal Signal Decomposition in Polarized Light Imaging". In: *Journal of Neuroscience Methods* 220.1 (Oct. 2013), pp. 30–38. ISSN: 01650270. DOI: 10.1016/j.jneumeth.2013.08.022.

[89] Jürgen Dammers et al. "Automatic Identification of Gray and White Matter Components in Polarized Light Imaging". In: *NeuroImage* 59.2 (Jan. 2012), pp. 1338–1347. ISSN: 10538119. DOI: 10.1016/j.neuroimage.2011.08.030.

[90] Jurgen Dammers et al. "Integration of Amplitude and Phase Statistics for Complete Artifact Removal in Independent Components of Neuromagnetic Recordings". In: *IEEE Transactions on Biomedical Engineering* 55.10 (Oct. 2008), pp. 2353–2362. ISSN: 0018-9294, 1558-2531. DOI: 10.1109/TBME.2008.926677.

[91] A. Hyvärinen and E. Oja. "Independent Component Analysis: Algorithms and Applications". In: *Neural Networks* 13.4-5 (June 2000), pp. 411–430. ISSN: 08936080. DOI: 10.1016/S0893-6080(00)00026-5.

[92] Te-Won Lee, Mark Girolami, and Terrence J. Sejnowski. "Independent Component Analysis Using an Extended Infomax Algorithm for Mixed Subgaussian and Supergaussian Sources". In: *Neural Computation* 11.2 (Feb. 1, 1999), pp. 417–441. ISSN: 0899-7667, 1530-888X. DOI: 10.1162/089976699300016719.

[93] F. Pedregosa et al. "Scikit-Learn: Machine Learning in Python". In: *Journal of Machine Learning Research* 12 (2011), pp. 2825–2830.

[94] Nobuyuki Otsu. "A Threshold Selection Method from Gray-Level Histograms". In: *IEEE Transactions on Systems, Man, and Cybernetics* 9.1 (Jan. 1979), pp. 62–66. ISSN: 0018-9472, 2168-2909. DOI: 10.1109/TSMC.1979.4310076.

[95] John E. Stone, David Gohara, and Guochun Shi. "OpenCL: A Parallel Programming Standard for Heterogeneous Computing Systems". In: *Computing in Science & Engineering* 12.3 (May 2010), pp. 66–73. ISSN: 1521-9615. DOI: 10.1109/MCSE.2010.69.

[96] Robbert L. Harms and Alard Roebroeck. "Robust and Fast Markov Chain Monte Carlo Sampling of Diffusion MRI Microstructure Models". In: *Frontiers in Neuroinformatics* 12 (Dec. 18, 2018), p. 97. ISSN: 1662-5196. DOI: 10.3389/fninf.2018.00097.

[97] Arak M. Mathai and Hans J. Haubold. *Probability and Statistics: A Course for Physicists and Engineers*. De Gruyter, Dec. 18, 2017. ISBN: 978-3-11-056254-5. DOI: 10.1515/9783110562545.

[98] "LII. An essay towards solving a problem in the doctrine of chances. By the late Rev. Mr. Bayes, F. R. S. communicated by Mr. Price, in a letter to John Canton, A. M. F. R. S". In: *Philosophical Transactions of the Royal Society of London* 53 (Dec. 31, 1763), pp. 370–418. ISSN: 0261-0523, 2053-9223. DOI: 10.1098/rstl.1763.0053.

[99] Andrew Gelman et al. *Bayesian Data Analysis*. Third edition. Texts in Statistical Science Series. Boca Raton London New York: CRC Press, Taylor and Francis Group, 2014. 667 pp. ISBN: 978-1-4398-4095-5.

[100] Daniel Foreman-Mackey et al. "Emcee : The MCMC Hammer". In: *Publications of the Astronomical Society of the Pacific* 125.925 (Mar. 2013), pp. 306–312. ISSN: 00046280, 15383873. DOI: 10.1086/670067.

[101] Jonathan Goodman and Jonathan Weare. "Ensemble Samplers with Affine Invariance". In: *Communications in Applied Mathematics and Computational Science* 5.1 (Jan. 31, 2010), pp. 65–80. ISSN: 2157-5452, 1559-3940. DOI: 10.2140/camcos.2010.5.65.

[102] Vivekananda Roy. "Convergence Diagnostics for Markov Chain Monte Carlo". In: *Annual Review of Statistics and Its Application* 7.1 (Mar. 9, 2020), pp. 387–412. ISSN: 2326-8298, 2326-831X. DOI: 10.1146/annurev-statistics-031219-041300.

[103] Daniel Foreman-Mackey. "Corner.Py: Scatterplot Matrices in Python". In: *The Journal of Open Source Software* 1.2 (June 8, 2016), p. 24. ISSN: 2475-9066. DOI: 10.21105/joss.00024.

[104] Andreas Klöckner et al. "PyCUDA and PyOpenCL: A Scripting-Based Approach to GPU Run-Time Code Generation". In: *Parallel Computing* 38.3 (2012), pp. 157–174. ISSN: 0167-8191. DOI: 10.1016/j.parco.2011.09.001.

[105] Ben Van Werkhoven, Willem Jan Palenstijn, and Alessio Sclocco. "Lessons Learned in a Decade of Research Software Engineering GPU Applications". In: *Computational Science – ICCS 2020*. Ed. by Valeria V. Krzhizhanovskaya et al. Vol. 12143. Cham: Springer International Publishing, 2020, pp. 399–412. ISBN: 978-3-030-50435-9 978-3-030-50436-6. DOI: 10.1007/978-3-030-50436-6_29.

[106] Gareth O. Roberts and Jeffrey S. Rosenthal. "Examples of Adaptive MCMC". In: *Journal of Computational and Graphical Statistics* 18.2 (Jan. 2009), pp. 349–367. ISSN: 1061-8600, 1537-2715. DOI: 10.1198/jcgs.2009.06134.

[107] Cynthia Rudin and Joanna Radin. "Why Are We Using Black Box Models in AI When We Don't Need To? A Lesson From An Explainable AI Competition". In: *Harvard Data Science Review* 1.2 (Nov. 1, 2019). DOI: 10.1162/99608f92.5a8a3a3d.

[108] Cynthia Rudin. "Stop Explaining Black Box Machine Learning Models for High Stakes Decisions and Use Interpretable Models Instead". In: *Nature Machine Intelligence* 1.5 (May 13, 2019), pp. 206–215. ISSN: 2522-5839. DOI: 10.1038/s42256-019-0048-x.

[109] T. J. Hastie and R. J. Tibshirani. *Generalized Additive Models*. New York: Routledge, Oct. 25, 2017. 352 pp. ISBN: 978-0-203-75378-1. DOI: 10.1201/9780203753781.

[110] Daniel Schmitz et al. "Fast Data-Driven Computation and Intuitive Visualization of Fiber Orientation Uncertainty in 3D-polarized Light Imaging". In: *Frontiers in Physics* 10 (Sept. 26, 2022), p. 958364. ISSN: 2296-424X. DOI: 10.3389/fphy.2022.958364.

[111] Kaatje Bollaerts, Paul H. C. Eilers, and Iven Van Mechelen. "Simple and Multiple P-splines Regression with Shape Constraints". In: *British Journal of Mathematical and Statistical Psychology* 59.2 (Nov. 2006), pp. 451–469. ISSN: 0007-1102, 2044-8317. DOI: 10.1348/000711005X84293.

[112] Natalya Pya and Simon N. Wood. "Shape Constrained Additive Models". In: *Statistics and Computing* 25.3 (May 2015), pp. 543–559. ISSN: 0960-3174, 1573-1375. DOI: 10.1007/s11222-013-9448-7.

[113] Daniel Servén et al. *Dswah/pyGAM: V0.8.0*. Version v0.8.0. Zenodo, Oct. 31, 2018. DOI: 10.5281/ZENODO.1208723.

[114] Mason Woo et al. *OpenGL Programming Guide: The Official Guide to Learning OpenGL, Version 1.2*. Addison-Wesley Longman Publishing Co., Inc., 1999.

[115] Michael M. Zeineh et al. "Direct Visualization and Mapping of the Spatial Course of Fiber Tracts at Microscopic Resolution in the Human Hippocampus". In: *Cerebral Cortex* (Feb. 13, 2016), bhw010. ISSN: 1047-3211, 1460-2199. DOI: 10.1093/cercor/bhw010.

[116] T.E.J. Behrens et al. "Characterization and Propagation of Uncertainty in Diffusion-weighted MR Imaging". In: *Magnetic Resonance in Medicine* 50.5 (Nov. 2003), pp. 1077–1088. ISSN: 0740-3194, 1522-2594. DOI: 10.1002/mrm.10609.

[117] Will Schroeder, Ken Martin, and Bill Lorensen. *The Visualization Toolkit (4th Ed.)* Kitware, 2006. ISBN: 978-1-930934-19-1.

[118] Sharib Ali et al. "Rigid and Non-Rigid Registration of Polarized Light Imaging Data for 3D Reconstruction of the Temporal Lobe of the Human Brain at Micrometer Resolution". In: *NeuroImage* 181 (Nov. 2018), pp. 235–251. ISSN: 10538119. DOI: 10.1016/j.neuroimage.2018.06.084.

[119] Christoph Palm. "Towards Ultra-High Resolution Fibre Tract Mapping of the Human Brain - Registration of Polarised Light Images and Reorientation of Fibre Vectors". In: *Frontiers in Human Neuroscience* (2010). ISSN: 16625161. DOI: 10.3389/neuro.09.009.2010.

[120] Amy F. D. Howard et al. "An Open Resource Combining Multi-Contrast MRI and Microscopy in the Macaque Brain". In: *Nature Communications* 14.1 (July 19, 2023), p. 4320. ISSN: 2041-1723. DOI: 10.1038/s41467-023-39916-1.

[121] Anastasia Yendiki et al. "Post Mortem Mapping of Connectional Anatomy for the Validation of Diffusion MRI". In: *NeuroImage* 256 (Aug. 2022), p. 119146. ISSN: 10538119. DOI: 10.1016/j.neuroimage.2022.119146.

[122] J. Mollink et al. "White Matter Changes in the Perforant Path Area in Patients with Amyotrophic Lateral Sclerosis". In: *Neuropathology and Applied Neurobiology* 45.6 (Oct. 2019), pp. 570–585. ISSN: 0305-1846, 1365-2990. DOI: 10.1111/nan.12555.

[123] Alberto Lazari and Ilona Lipp. "Can MRI Measure Myelin? Systematic Review, Qualitative Assessment, and Meta-Analysis of Studies Validating Microstructural Imaging with Myelin Histology". In: *NeuroImage* 230 (Apr. 2021), p. 117744. ISSN: 10538119. DOI: 10.1016/j.neuroimage.2021.117744.

[124] Alex L. MacKay and Cornelia Laule. "Magnetic Resonance of Myelin Water: An in Vivo Marker for Myelin". In: *Brain Plasticity* 2.1 (Dec. 21, 2016). Ed. by Bernard Zalc, pp. 71–91. ISSN: 22136304, 22136312. DOI: 10.3233/BPL-160033.

[125] Alex Mackay et al. "In Vivo Visualization of Myelin Water in Brain by Magnetic Resonance". In: *Magnetic Resonance in Medicine* 31.6 (June 1994), pp. 673–677. ISSN: 07403194, 15222594. DOI: 10.1002/mrm.1910310614.

[126] Brian Avants, Nicholas J. Tustison, and Gang Song. "Advanced Normalization Tools: V1.0". In: *The Insight Journal* (July 29, 2009). ISSN: 2327-770X. DOI: 10.54294/uvnhin.

[127] Francisco P.M. Oliveira and João Manuel R.S. Tavares. "Medical Image Registration: A Review". In: *Computer Methods in Biomechanics and Biomedical Engineering* 17.2 (Jan. 25, 2014), pp. 73–93. ISSN: 1025-5842, 1476-8259. DOI: 10.1080/10255842.2012.670855.

[128] Jiri Borovec et al. "ANHIR: Automatic Non-Rigid Histological Image Registration Challenge". In: *IEEE Transactions on Medical Imaging* 39.10 (Oct. 2020), pp. 3042–3052. ISSN: 0278-0062, 1558-254X. DOI: 10.1109/TMI.2020.2986331.

[129] Shammamah Hossain. "Visualization of Bioinformatics Data with Dash Bio". In: Python in Science Conference. Austin, Texas, 2019, pp. 126–133. DOI: 10.25080/Majora-7ddc1dd1-012.

[130] Ziv Yaniv et al. "SimpleITK Image-Analysis Notebooks: A Collaborative Environment for Education and Reproducible Research". In: *Journal of Digital Imaging* 31.3 (June 2018), pp. 290–303. ISSN: 0897-1889, 1618-727X. DOI: 10.1007/s10278-017-0037-8.

[131] Bradley C. Lowekamp et al. "The Design of SimpleITK". In: *Frontiers in Neuroinformatics* 7 (2013). ISSN: 1662-5196. DOI: 10.3389/fninf.2013.00045.

[132] Andriy Fedorov et al. "3D Slicer as an Image Computing Platform for the Quantitative Imaging Network". In: *Magnetic Resonance Imaging* 30.9 (Nov. 2012), pp. 1323–1341. ISSN: 0730725X. DOI: 10.1016/j.mri.2012.05.001.

[133] Jeroen Mollink et al. "Evaluating Fibre Orientation Dispersion in White Matter: Comparison of Diffusion MRI, Histology and Polarized Light Imaging". In: *NeuroImage* 157 (Aug. 2017), pp. 561–574. ISSN: 10538119. DOI: 10.1016/j.neuroimage.2017.06.001.

[134] Todd Gamblin and Daniel S. Katz. "Overcoming Challenges to Continuous Integration in HPC". In: *Computing in Science & Engineering* 24.6 (Nov. 2022), pp. 54–59. ISSN: 1521-9615, 1558-366X. DOI: 10.1109/MCSE.2023.3263458.

[135] Yiming Zhang et al. "Probabilistic Invertible Neural Network for Inverse Design Space Exploration and Reasoning". In: *Electronic Research Archive* 31.2 (2023), pp. 860–881. ISSN: 2688-1594. DOI: 10.3934/era.2023043.

[136] Ashish Vaswani et al. "Attention Is All You Need". In: *Advances in Neural Information Processing Systems*. Ed. by I. Guyon et al. Vol. 30. Curran Associates, Inc., 2017.

[137] Kurt Schilling et al. "Confirmation of a Gyral Bias in Diffusion MRI Fiber Tractography". In: *Human Brain Mapping* 39.3 (Mar. 2018), pp. 1449–1466. ISSN: 1065-9471, 1097-0193. DOI: 10.1002/hbm.23936.

[138] Pierre Fillard, Cyril Poupon, and Jean-François Mangin. "A Novel Global Tractography Algorithm Based on an Adaptive Spin Glass Model". In: *Medical Image Computing and Computer-Assisted Intervention – MICCAI 2009*. Ed. by Guang-Zhong Yang et al. Vol. 5761. Berlin, Heidelberg: Springer Berlin Heidelberg, 2009, pp. 927–934. ISBN: 978-3-642-04267-6 978-3-642-04268-3. DOI: 10.1007/978-3-642-04268-3_114.

[139] Patrick C. Nahirney and Marie-Eve Tremblay. "Brain Ultrastructure: Putting the Pieces Together". In: *Frontiers in Cell and Developmental Biology* 9 (Feb. 18, 2021), p. 629503. ISSN: 2296-634X. DOI: 10.3389/fcell.2021.629503.

[140] Vincent Arsigny, Xavier Pennec, and Nicholas Ayache. "Polyrigid and Polyaffine Transformations: A New Class of Diffeomorphisms for Locally Rigid or Affine Registration". In: *Medical Image Computing and Computer-Assisted Intervention - MICCAI 2003*. Ed. by Randy E. Ellis and Terry M. Peters. Red. by Gerhard Goos, Juris Hartmanis, and Jan Van Leeuwen. Vol. 2879. Berlin, Heidelberg: Springer Berlin Heidelberg, 2003, pp. 829–837. ISBN: 978-3-540-20464-0 978-3-540-39903-2. DOI: 10.1007/978-3-540-39903-2_101.

[141] Mousumi Roy et al. "Deep Learning Based Registration of Serial Whole-Slide Histopathology Images in Different Stains". In: *Journal of Pathology Informatics* 14 (2023), p. 100311. ISSN: 21533539. DOI: 10.1016/j.jpi.2023.100311.

[142] Alexander Oberstrass et al. *Self-Supervised Representation Learning for Nerve Fiber Distribution Patterns in 3D-PLI*. Jan. 30, 2024. arXiv: 2401.17207 [cs]. URL: http://arxiv.org/abs/2401.17207 (visited on 03/14/2024). Pre-published.

[143] Alexandros Popov. "Global Inference of the Structural Connectivity of White Matter Fiber Bundles Using Deep Learning Approaches and Microstructural Prior Knowledge". Theses. Université Paris-Saclay, June 2022.